A conserved interdomain linker of CCT mediates allosteric communication between regulatory and catalytic domains

by

Daniel Knowles

B.Sc., Simon Fraser University, 2016

Thesis Submitted in Partial Fulfillment of the
Requirements for the Degree of
Master of Science

in the
Department of Molecular Biology and Biochemistry
Faculty of Science

SIMON FRASER UNIVERSITY
Fall 2018

Approval

Name:	**Daniel Knowles**
Degree:	**Master of Science**
Title:	**A conserved interdomain linker of CCT mediates allosteric communication between regulatory and catalytic domains**
Examining Committee:	**Chair:** Sharon Gorski Professor
	Rosemary Cornell Senior Supervisor Professor
	Jenifer Thewalt Supervisor Professor
	Edgar Young Supervisor Associate Professor
	Tom Claydon Internal Examiner Associate Professor Biomedical Physiology and Kinesiology
Date Defended/Approved:	December 3, 2018

Abstract

Folding landscapes of linkers between ligand-binding and functional domains evolved to facilitate transmission of inter-domain signals. I investigated the structure/function of a conserved linker between the catalytic and membrane-binding (M) domains of CCT, which regulates phosphatidylcholine synthesis and activates upon membrane binding. The activity of CCT is very sensitive to mutations in the linker. Recent molecular dynamics simulations revealed that upon removal of auto-inhibitory contacts between the M domain and the active site, the αE helix adjacent to the linker bends toward the active site, bringing the catalytic domain close to the membrane surface. Tryptophan fluorescence quenching revealed that the linker lies superficially on the membrane surface. FRET between engineered tryptophans and vesicles containing Dansyl-Phosphatidylethanolamine support a bent αE helix conformation that is dependent on the native linker sequence. The data suggests that the linker may communicate membrane binding signals to enhance CCT activity by directly stabilizing a bent αE.

Keywords: CTP:phosphocholine cytidylyltransferase (CCT); allostery; amphitropism; lipids; interdomain linker; fluorescence

Acknowledgements

I would like to thank all the members of the Cornell lab, past and present, along with countless other researchers for laying the foundation of this work. Specifically, I would like to thank Cameron Proceviat for introducing me to the initial fluorescence experiments and Ronnie Tse for generating the original constructs used in tryptophan quenching experiments. I thank Kady Tishyadhigama for her contribution to this thesis during her ISS and all her support thereafter. I thank Dr. Jaeyong Lee for all his help during my MSc, providing advice and feedback for experiments and presentations. I also thank Jae for his contributions to the data in this thesis through generation of initial constructs and FPLC experiments. I thank Dr. Svetla Taneva for all her support and friendship throughout these years and for providing expert advice whenever experiments were not working well. I would like to thank Dr. Jenifer Thewalt and Dr. Edgar Young for all their input/feedback and for contributing to useful committee meetings. I would like to thank Dr. Tom Claydon for his input on FRET experiments and for participating in my thesis defence. Finally, I would like to thank Dr. Rosemary Cornell for her countless hours of support and guidance and for driving my improvement as a scientist.

Table of Contents

List of Tables

List of Figures

List of Acronyms

CCT	CTP: phosphocholine cytidylyltransferase
NMR	Nuclear magnetic resonance
PDB	Protein Data Bank
ATP	Adenosine triphosphate
ADP	Adenosine diphosphate
PS	Phosphatidylserine
PI	Phosphatidylinositol
PG	Phosphatidylglycerol
PE	Phosphatidylethanolamine
DAG	Diacylglycerol
PC	Phosphatidylcholine
POPC	1-palmitoyl-2-oleoyl-glycero-3-phosphocholine
BrPC	Brominated phosphatidylcholine
CTP	Cytidine triphosphate
CDP-choline	Cytidine 5'-diphosphocholine
NLS	Nuclear localization signal
K_{SV}	Stern-Volmer constant
FRET	Fluorescence resonance energy transfer
T_m	Melting temperature
FPLC	Fast protein liquid chromatography
LPC	Lysophosphatidylcholine
EC_{50}	Half maximal effective concentration
dansyl-PE	Dansylated 1,2-dioleoyl-glycero-3-phosphoethanolamine
SUV	Small (sonicated) unilamellar vesicle

Chapter 1. Introduction

1.1. Protein Allostery

1.1.1. Protein dynamics contribute to allosteric regulation

High resolution structural studies have uncovered the static architecture of a wide range of proteins, revealing how function may be altered in different states. However, it is now known that the function of proteins is ultimately dictated by their dynamic nature (1). Rather than forming a single highly stable, motionless structure, proteins are fluid molecules that exist as an ensemble of conformations in equilibrium around a specific favoured state. Intermolecular signals can shift this equilibrium to favour a new state and alter function.

Protein allostery, the regulation of protein function by direct interaction with effector molecules, relies on the highly dynamic nature of proteins. Structural perturbations induced by effector molecule binding events propagate from regulatory sites to distal protein sites to dictate function. These propagated perturbations stabilize a new global protein state, around which the protein structure and dynamics equilibrates. The central problem of allostery remains: what are the molecular mechanisms for propagation of effector-induced signals to distal sites, and how do these changes regulate function of specific proteins and pathways?

1.1.2. Allosteric linkers can facilitate interdomain signaling

Studying mechanisms of protein allostery becomes even more complex in the context of multidomain proteins, which constitute the majority of the eukaryotic proteome (2). As protein domains are typically distinct folding units, an effector binding event in one domain does not necessarily have a direct structural impact in another. So how have proteins evolved to communicate these interdomain signals? Flexible interdomain linkers connect domains physically, but they often serve a more active role in protein function, beyond simply preventing steric domain clashes. A subset of interdomain linkers, termed allosteric linkers, propagate conformational changes through modulation of their own dynamics to signal between effector-binding regulatory domains, and

functional domains of proteins (3) (**Fig. 1.1**). Allosteric linkers generally possess conserved sequences that encode specific, favoured folding pathways which are triggered by effector binding events in the regulatory domain.

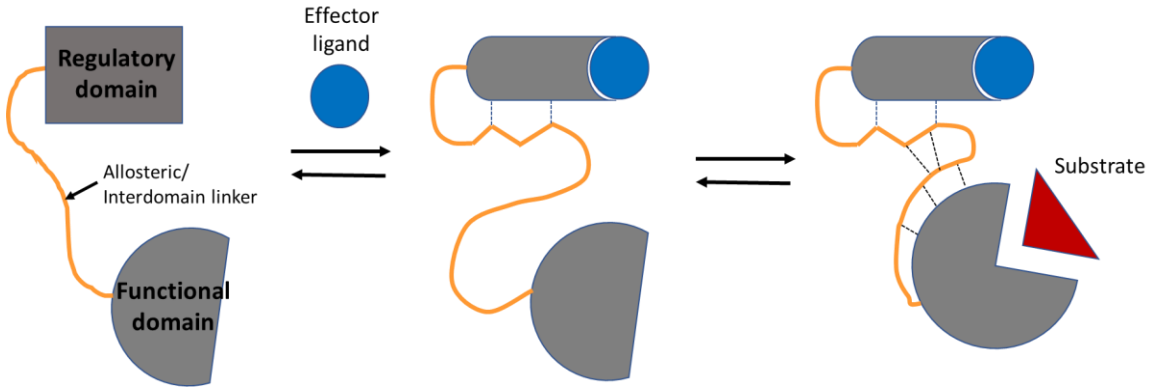

Figure 1.1. *Propagation of allosteric signals between domains can be facilitated by interdomain linker segments.* A hypothetical functionally "silent" protein (left) may have physically distinct regulatory and functional domains. When the regulatory domain binds an effector, conformational changes occur in this domain that propagate through the interdomain linker. The new linker conformation (which may involve contacts with either domain) induces a new, favoured conformation of the functional domain, which has altered functional activity (e.g. enhanced affinity for substrate).

Several recent studies have provided interesting examples of conserved linkers and the strategies they utilize to bridge this communication gap between regulatory and functional domains. An allosteric, interdomain linker in protein kinase A (PKA) breaks and forges weak, state-selective intramolecular contacts and alters its flexibility during the activation/inactivation cycle. In the inactive state, PKA's linker forms an extended structure along the active site cleft, which is resolved in crystal structures (4). During enzyme activation, the secondary messenger cAMP binds PKA's regulatory domain. NMR studies revealed that as a result of cAMP binding, the linker becomes more flexible, breaking interactions with the catalytic domain and forming new interactions with the regulatory domain which are essential for enzyme activation (5). In another example, the conserved allosteric linker between the nucleotide-binding regulatory domain (NBD) and the substrate-binding domain (SBD) of heat shock protein 70 (Hsp70) regulates protein function by a global re-orientation of the two domains with respect to each other (6). Hsp70 regulates general folding pathways by repeated binding and release of unfolded peptides to its SBD (7). The NBD controls the affinity of SBD for unfolded peptides by ATP binding (decreases SBD-peptide affinity) and ATP hydrolysis

(increases SBD-peptide affinity). In the ATP-bound form, the linker is well-structured and forms contacts near a stabilized SBD-NBD interface, closing off the SBD to substrate interaction (8). In the ADP-bound form the linker takes on an extended, more flexible structure that equilibrates between a few favoured states, separating the SBD and NBD, and enabling substrate binding (6). These two examples showcase that linkers can alter their flexibility and conformation in response to allosteric signals, and these changes can alter functional domains by generating new intramolecular interactions or re-orienting regulatory and functional domains. It is plausible that other, understudied interdomain linkers use similar strategies to facilitate allostery.

1.2. Amphitropic proteins

Many cellular processes are localized to membranes, and therefore, the functions of many proteins need to be concentrated there as well. Some of these proteins, called amphitropic proteins, regulate their function by reversibly binding to lipids (9), essentially using lipids as allosteric ligands. CCT, the enzyme that is the central focus of my thesis, is an amphitropic protein regulated by changes in membrane lipid composition. The next two sections will describe some general features of amphitropic proteins and the features of membranes that promote the binding of CCT and other amphitropic proteins.

1.2.1. Amphitropic proteins utilize different strategies to sense specific membrane characteristics

Membrane-binding, regulatory regions of amphitropic proteins utilize multiple strategies to interact with membranes. Some soluble proteins contain covalently linked fatty acids or isoprenyl groups to ensure membrane localization, such as the Ras GTPases and Src protein kinases, but a single acyl/alkyl chain provides insufficient binding strength to capture the protein on a bilayer (9). To regulate function, these proteins use a second, reversible lipid-binding domain for a strong membrane interaction (10). A second strategy utilized by some amphitropic proteins are lipid clamps. Lipid clamps are structurally conserved protein domains that have affinity for specific, low concentration lipids in membranes (9). For example, pleckstrin homology (PH) domains found on many signaling proteins generally have a high affinity for phosphatidylinositol phosphate (PIP) headgroups (11). Signals originating from cell surface receptors can

increase the membrane concentration of specific PIPs that promote membrane localization of a range of important PH domain-containing signaling proteins (12,13).

A third strategy for reversible membrane interaction utilized by amphitropic proteins is amphipathic helices. Amphipathic helices are unique membrane-binding domains as they typically undergo a drastic structural change during the conversion from a soluble peptide to a membrane-bound peptide. These domains are often highly basic and unfolded when the protein is in solution and fold into an α-helix during membrane docking (14). They produce a weak membrane interaction that can be regulated by membrane lipid composition. Electrostatic interactions facilitate the approach of the positively-charged residues in the soluble domain to the negative surface charge of the membrane. Then, hydrophobic residues in the domain penetrate the lipid bilayer and interact with the underlying fatty acyl chains of the phospholipids, a process driven by a random coil to α-helix transition (15). The resulting membrane-bound domain is an α-helix that lies parallel to the membrane surface with a non-polar face embedded in the bilayer, and a polar face oriented towards the solvent. Basic residues are often positioned at the membrane interface, forging electrostatic interactions with the anionic lipid headgroups. These characteristics of amphipathic helices allow their membrane interaction to be regulated by a balance of hydrophobic and electrostatic interactions, which are dictated by the chemical and physical characteristics of the membrane. These characteristics are ultimately determined by the relative composition of specific lipid types in the membrane.

1.2.2. Lipid composition dictates membrane characteristics and affinity for amphipathic helices

The strength of electrostatic interactions that increase the amphipathic helix-membrane affinity is determined by the relative amount of lipids with charged headgroups in the membrane. In biological membranes, the surface charge is net negative, largely contributed by the anionic lipids phosphatidylserine (PS) and phosphatidylinositol (PI) (16). Phosphatidylglycerol (PG) and cardiolipin are two other anionic lipids prominent in mitochondria that can enhance negative charge density on membranes. Phosphatidylcholine (PC) and phosphatidylethanolamine (PE) are major zwitterionic membrane phospholipids that counterbalance the negative surface charge (16). Relative metabolism of these phospholipids and their distribution in different

organelles provides a balance of surface charge that can regulate the membrane affinity and subsequent function of proteins containing amphipathic helices.

A second characteristic of lipids that controls the membrane affinity of amphipathic helices is lipid shape and resulting membrane architecture. Lipids can be classified into three shape categories based on the relative surface area along the plane of the bilayer occupied by the headgroup vs. acyl chains: inverted cone/type II (headgroup area smaller than acyl chains), cylindrical (similar size headgroup and acyl chains), and cone/type I (headgroup area larger than acyl chains) (17) (**Fig. 1.2**). Accumulation of type I or type II lipids on one bilayer leaflet causes energetically unfavourable packing gaps that prevent continuous hydrophobic contacts along acyl chains, creating bilayer strain. In the case of type II lipids, packing gaps between the headgroups can be relieved by negative curvature of each monolayer (14). But because adoption of negative curvature would disrupt bilayer integrity via disruption of intermonolayer acyl chain contacts, membranes with high content of these lipids retain acyl chain contact between monolayers and instead build up strain (18). Packing gaps and curvature strain can promote the binding of amphipathic helices (**Fig. 1.3**). Packing gaps provide the hydrophobic face of the α-helix with easy access to the acyl chains of the bilayer to forge hydrophobic interactions. Bilayer stress is relieved as the packing gaps are filled by the peptide (14). In summary, the membrane interaction of amphipathic helices is highly tuned based on the lipid composition of membranes, which can alter both electrostatic surface charge and membrane curvature/packing gaps.

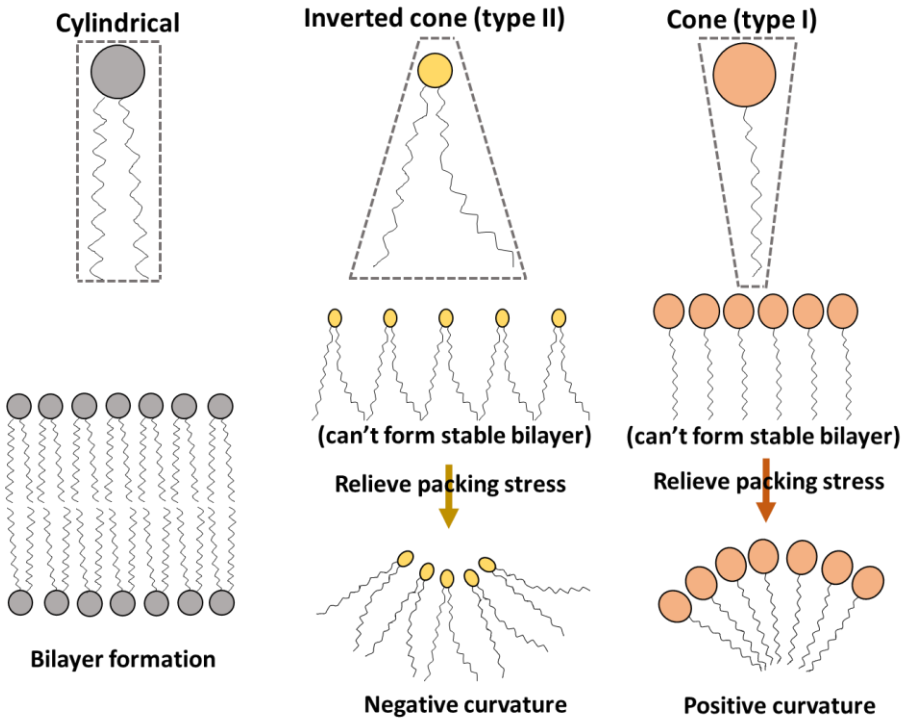

Figure 1.2. *Shapes of lipids dictate the level of packing stress on the bilayer.* In a bilayer, type II lipids (eg. DAG) produce packing gaps between headgroups. This high-energy state (packing stress) of type II lipids can be relieved by negative curvature to promote acyl chain contacts. With type I lipids, the packing stress can be relieved by positive curvature.

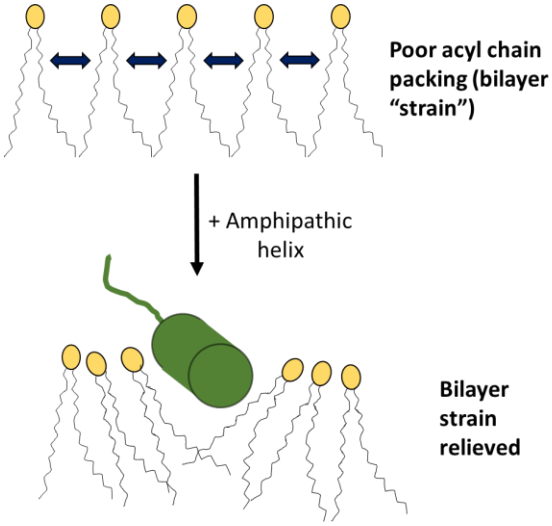

Figure 1.3. *Packing stress caused by accumulation of type II lipids can be relieved by binding of an amphipathic helix*. When maintained as a bilayer, type II lipids contribute to packing gaps, causing unfavourable bilayer strain. In this case, the hydrophobic acyl chains are exposed to solvent, promoting docking of the hydrophobic face of an amphipathic helix, which relieves the bilayer strain.

1.3. CTP: phosphocholine cytidylyltransferase (CCT)

1.3.1. CCT regulates PC synthesis by amphitropism

CCT, an enzyme involved in synthesis of membrane PC (19), is an amphitropic protein that utilizes amphipathic helices for regulation by reversible membrane binding (20-24). CCT catalyzes the rate-limiting step of the CDP-choline (Kennedy) pathway of PC synthesis in eukaryotes (**Fig. 1.4**). In this pathway, choline is first phosphorylated to phosphocholine by a choline kinase. CCT then uses phosphocholine and CTP as substrates to form CDP-choline and pyrophosphate products. Finally, a headgroup transfer occurs, catalyzed by the transmembrane enzyme cholinephosphotransferase, in which CDP-choline and diacylglycerol (DAG) substrates are utilized to produce PC and CMP products (25). It is CCT's amphitropism, i.e. its activity dependence on binding to a PC-deficient membrane, that allows this step in the pathway to regulate PC composition of eukaryotic cell membranes.

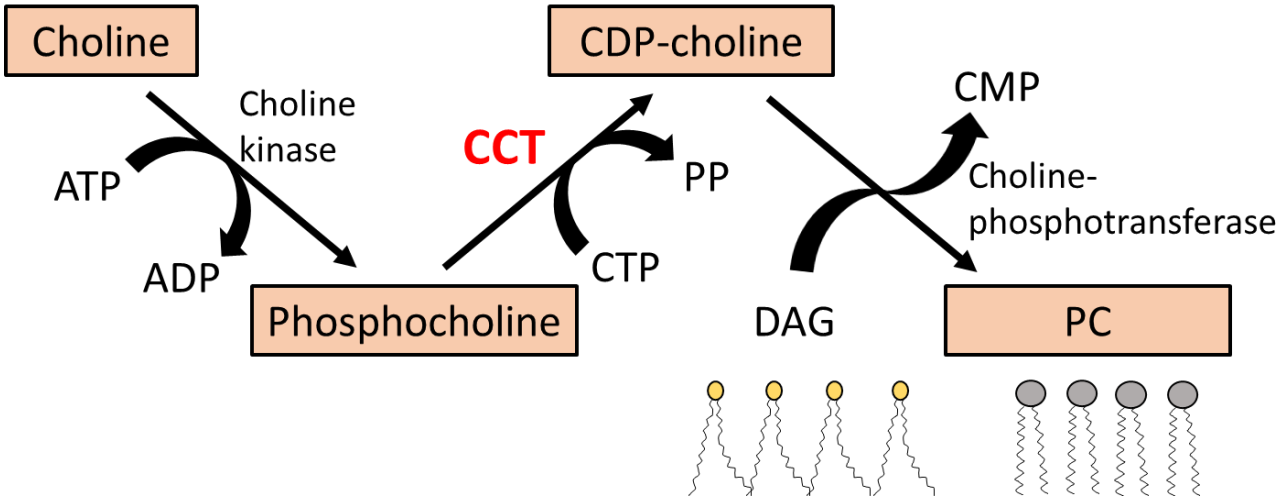

Figure 1.4. *The CDP-choline pathway is the major pathway of phosphatidylcholine (PC) synthesis in eukaryotes.* First, choline is phosphorylated by a choline kinase. CCT then catalyzes the conversion of choline-phosphate to CDP-choline, using CTP as a substrate. Finally, diacylglycerol (DAG) is converted to PC through the addition of a choline head group and release of CMP.

The nature of CCT's membrane binding domain (domain M) as an amphipathic helix provides CCT with a high-affinity for PC-deficient membranes (26). PC has a relatively large headgroup, making it a cylindrical lipid that promotes bilayer formation. In membranes with low PC levels, type II lipids (eg. unsaturated PE) are in relatively higher

abundance, which promotes domain M binding. PC is also zwitterionic and therefore PC-deficient membranes are relatively enriched in anionic lipids, and thus have a higher negative surface charge which attracts the basic residues of domain M. *In vitro* studies have demonstrated this, as rat CCT was weakly activated by pure PC vesicles and titration of anionic lipids into these vesicles sharply increased enzyme activity (27). When CCT binds membranes with the chemical and physical properties representing PC-deficiency, its upregulated activity initiates an increase of PC membrane levels. In this way, CCT is critical for maintaining the PC composition of eukaryotic membranes (**Fig. 1.5**).

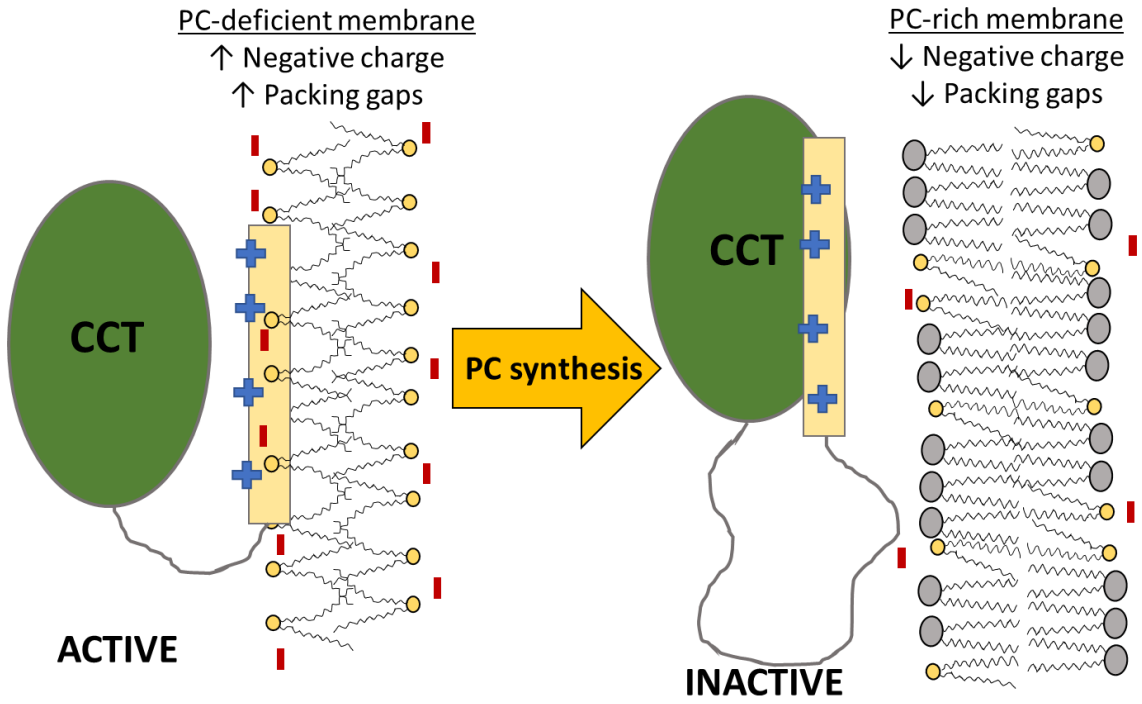

Figure 1.5. *CCT is amphitropic: It is activated by reversible membrane binding.* The properties of a PC-deficient membrane promote CCT binding through an amphipathic helical domain that embeds in the membrane. As the membrane loses these properties upon PC synthesis, CCT loses affinity for the membrane. This creates a feedback loop that allows CCT to regulate PC composition in the membrane.

1.3.2. CCT-catalyzed PC synthesis is important for numerous cellular functions in eukaryotes

PC is the major phospholipid in eukaryotic membranes (28). Two main pathways of PC-synthesis in eukaryotes have been established. The first is the CDP-choline

pathway described above. This pathway can be utilized with two distinct CCT isoforms: CCTα or CCTβ. CCTα is more ubiquitously expressed and localizes primarily to the nucleus (29-31). CCTβ lacks a nuclear localization signal (NLS) and therefore, localizes in the cytoplasm (32,33). These isoforms have distinct functions in cells but can provide compensatory roles in certain contexts (34). A second pathway of PC synthesis is the PE methylation pathway (35). Three successive methyl group transfers from S-adenosylmethionine to the ethanolamine headgroup of PE forms PC (ethanolamine → monomethylethanolamine → dimethylethanolamine → choline headgroup). All three methylations are catalyzed by phosphatidylethanolamine N-methyltransferase (PEMT) in mammals. This pathway only generates PC to a significant degree in the liver and adipose tissue in mammals (36,37). PEMT-knockout mice retained wild-type PC and PE-levels in the liver, and displayed no physiological defects (38). In these mice, CCT activity increased in the liver, suggesting the CDP-choline pathway may compensate for a loss of the PE methylation pathway. In the absence of dietary choline, PEMT prevented extensive liver malfunction in mice by providing PC and choline when the CDP-choline pathway lacks substrate to do so (39). However, PEMT-mediated compensation for loss of CCT-regulated PC synthesis is not complete, as loss of CCT function can have a number of detrimental effects in eukaryotes.

CCT-catalyzed PC is vital for global housekeeping of membrane structure and function through maintaining phospholipid homeostasis (40). In fact, CCTα knockout mice experience halted development before blastocyst formation (41). Deficiency in CCT-dependent PC also results in cell cycle arrest at various stages and subsequent apoptosis (42). General phospholipid homeostasis is also important for vesicle-trafficking/secretory pathways in cells (43). Work by Tian *et al.* showed that CCTα-deficient macrophages did not produce sufficient PC to allow lipopolysaccharide (LPS)-triggered cytokine secretion (44). The cytokines accumulated in the Golgi, suggesting that PC-deficiency prevents adequate membrane formation to promote vesicle budding from the Golgi. Finally, the synthesis of PC may indirectly regulate the amount of lipid secondary messengers in the membrane, such as DAG, phosphatidic acid, and lyso-PC, which are products of PC catabolism (45). An accumulation of data now supports the notion that CCTα-regulated PC synthesis specifically carries the weight of this responsibility to maintain global cellular health and processes (reviewed in (25,40)).

PC synthesized through the CDP-choline pathway also has several cell- and tissue-specific physiological functions. For example, epithelial cells in the lungs secrete a PC-rich surfactant in alveoli that reduces the surface tension of the air-water interface (46). Lung-targeted knock-out of CCTα in mice results in defects in surfactant production and lung function (47). The generation of triacylglycerol- and cholesterol-containing coated lipid droplets (lipoproteins) in hepatocytes relies heavily on CCT-synthesized PC. HDL and VLDL levels decrease upon disruption of PC synthesis through the CDP-choline pathway (48). Whereas CCTα is expressed ubiquitously, the CCTβ isoform is only expressed at high levels in the brain and gonads. PC production by CCTβ has been implicated in neuronal tissue development in cell culture and mouse models (49,50). Thus in addition to demand for CCT-dependent PC for organelle growth, PC is also specifically required for certain cell-specific functions.

1.3.3. CCTs have a conserved domain organization

CCTs form homodimers and each monomer is organized into 4 regions: N-terminal (N), catalytic (C), membrane-binding (M), and phosphorylation (P) (40) (**Fig. 1.6**). Region N is a disordered sequence with low conservation that, in the case of CCTα, contains a nuclear localization signal (NLS) (51). This sequence is vital for isoform-specific localization of CCTα to the nuclear membrane (29,30). Domain C is a highly conserved sequence and structure that houses the active site (discussed in depth in section 1.3.4) (52). Domain M is a flexible, highly charged sequence that folds into an amphipathic α-helix upon membrane binding (22,23,53,54). Its structure has been solved by NMR in complex with the membrane mimetic sodium dodecyl sulfate (SDS) (**Fig. 1.6**). This domain M-membrane interaction activates the catalytic domain (55). Finally, region P is a highly unstructured and variable sequence with 16 serine residues (in the case of CCTα), all of which can be phosphorylated (56). Phosphorylation of this domain is thought to have a role in regulation of membrane affinity (51,57,58). As phosphate groups are added to region P, electrostatic repulsion with anionic lipids lowers the charge-based membrane affinity of CCT's domain M, and raises the dependence of domain M membrane binding on the hydrophobic interactions promoted by membrane curvature and packing gaps (57,59).

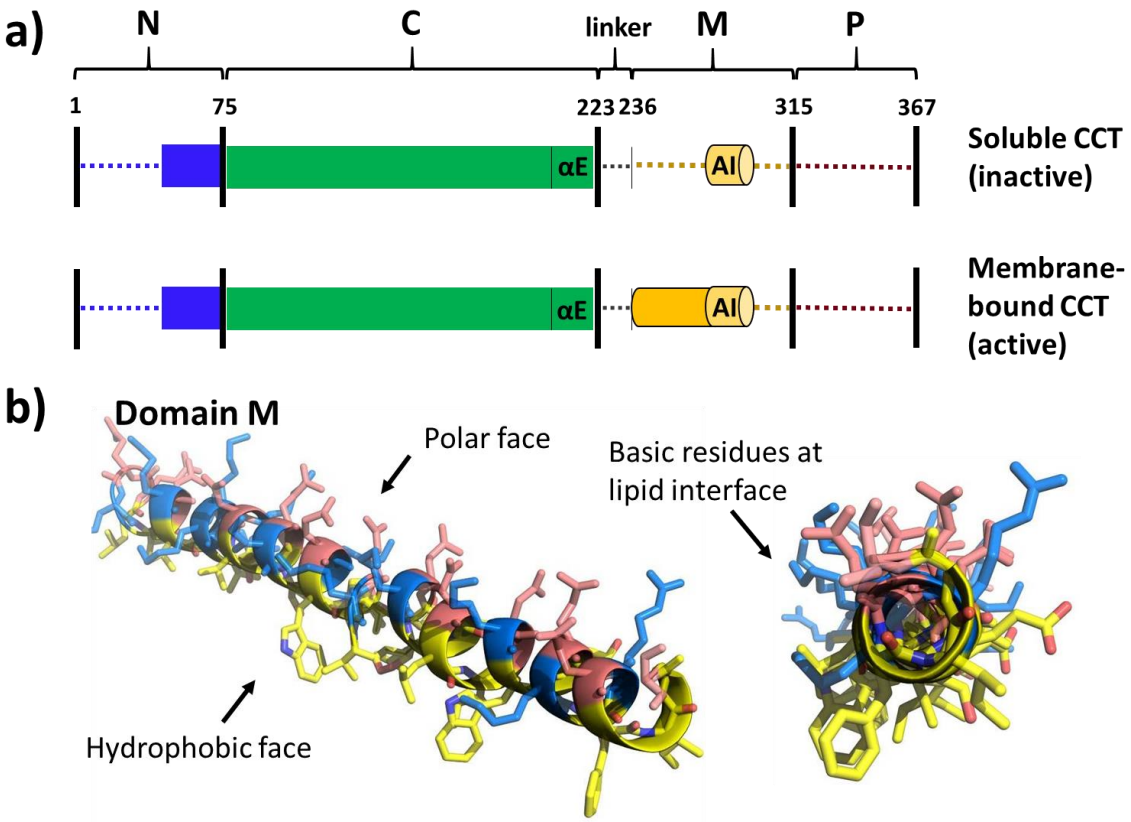

Figure 1.6. *Domains of a full-length CCT monomer: N-terminal (N) region, catalytic (C) domain, membrane-binding (M) domain, and phosphorylation (P) region.* **a)** Dotted lines represent disordered portions of CCT. The solid blue portion of region N represents the N-terminal cap of the catalytic domain. The conserved linker and αE helix are indicated. AI is the auto-inhibitory helix, which is preceded by a long, disordered leash in soluble CCT. The long, disordered leash of domain M forms a long amphipathic helix upon membrane binding. **b)** The solved NMR structure of domain M in complex with a membrane mimetic, SDS, (1PEI/1PEH) is shown from residues 243 -288. Residues on the hydrophobic face are indicated in yellow, residues in the polar face are red, and basic residues are blue.

1.3.4. Structural data reveals a mechanism for CCT auto-inhibition

Crystal structures of CCT reveal domain C adopts a Rossmann fold, common for nucleotide-binding proteins (52,60,61). Each monomer contains a 5-stranded twisted parallel β-sheet surrounded by five α-helices (**Fig. 1.7**). At the base of the β-sheet the active sites appear as large, two-armed pockets, with one arm for CTP and another for phosphocholine. Crystal structures with bound CDP-choline reveal ligand contacts with many amine groups donated from several loops (L1, L2, L5, and L6), that forge charge-stabilizing interactions with the α- and β-phosphates. CTP bound in the active site of

CTs adopts a strained U-shape stabilized by N-terminal αE residues that positions the α-phosphate for and in-line nucleophilic attack by phosphocholine and severance of the α – β phosphodiester (62) (**Fig. 1.8**). Mutagenesis has implicated several residues involved in active site contacts as catalytic requirements (52,63-65). One noteworthy residue, K122 in loop L2, is highly sensitive to mutation. Even a conserved arginine mutation at this position reduces k_{cat} / K_m by ~5 orders of magnitude (63). K122 is targeted for regulation by membrane binding, as I discuss below. The αE helices at the C-terminal of domain C extend away from each active site. The two αE helices crossover and make monomer-monomer contacts that, along with several other contact sites in domain C and region N, help stabilize the dimer interface. The αE helix is another site targeted for regulation.

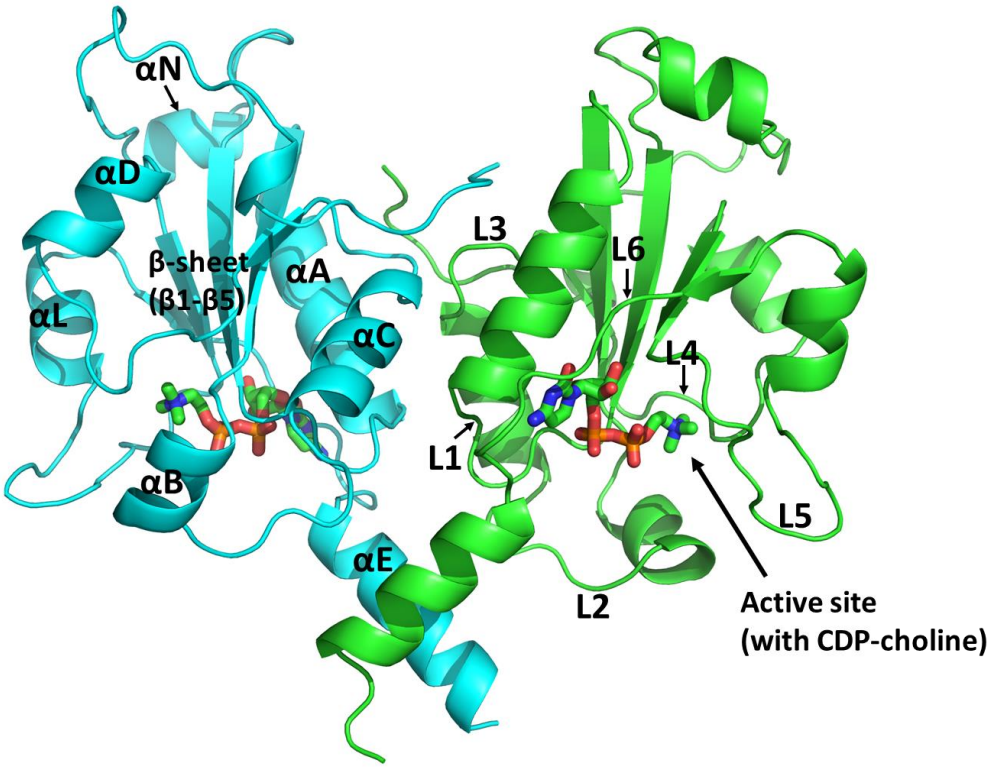

Figure 1.7. *Crystal structure of the catalytic domain of CCT*. Rat CCT dimer with a domain M/P truncation (CCT-236) and CDP-choline product in the active site is depicted (PDB: 3HL4). Monomers are displayed in different colours. The central, parallel β-sheet and its surrounding α-helices are labeled on one monomer (cyan) and the loops are labeled on the other monomer (green).

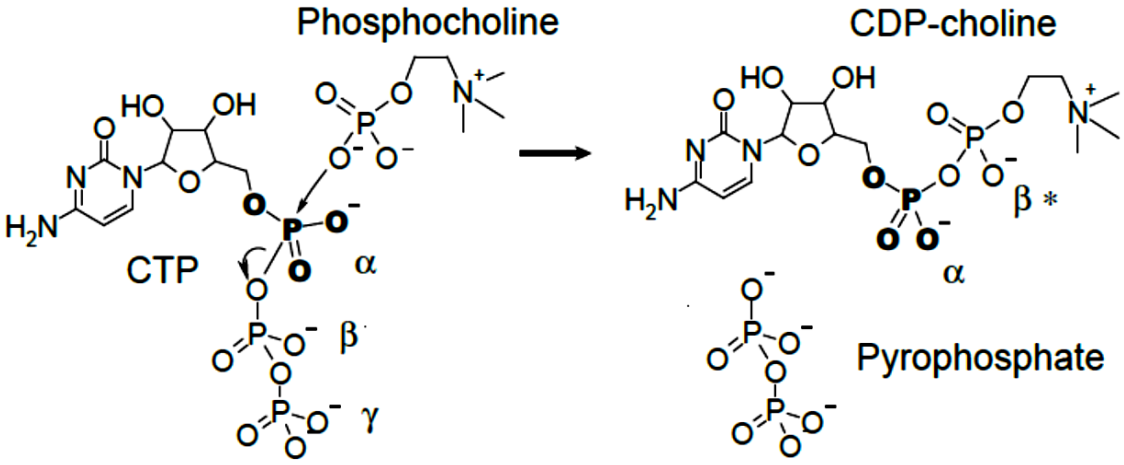

Figure 1.8. *The reaction mechanism of CCT-catalyzed CDP-choline production.* This reaction diagram is from Lee, *et al.* (2009) (52). The active site stabilizes a U-shaped, contorted CTP, allowing a nucleophilic attack by the phosphate of phosphocholine, on the α-phosphate of CTP, displacing pyrophosphate and forming CDP-choline.

The inactive, soluble form of CCT is characterized by auto-inhibitory contacts made between the αE helix and a region of domain M termed the auto-inhibitory (AI) helix (55,60,66,67) (**Fig. 1.9**). Each monomer donates one of each of these helices to form a catalytically-silencing 4-helix complex. Monitoring enzyme activity of CCT mutants with truncations in domain M revealed the AI helix as a hydrophobic segment of domain M that is important for silencing soluble CCT (60,68). In soluble CCT, the AI helix is linked to the C-terminal of αE by a long, flexible leash segment (66). The mostly hydrophobic contacts between the αE and AI helices position the C-terminal of each AI helix near the active site entrance. Molecular dynamics simulations suggest that the AI motif introduces a “backbone trap”, in which backbone carbonyls of F293, G294, and P295 (in the AI motif) and F124 (in loop L2) form electrostatic interactions with K122, directing it away from the active site and resulting in silenced CCT (60,69). As a result, backbone dynamics of loop L2 are also restricted.

1.3.5. The mechanism of CCT activation by membranes is not known

During CCT membrane docking, the AI helix dissociates from the αE helices and the flexible leash of domain M along with the AI segment folds to form a long amphipathic helix, coincident with membrane insertion. Membrane binding of domain M thus relieves auto-inhibitory contacts to allow K122 to engage substrate, and promote αE helix dynamics (60). Interestingly, regulation of CCT activity by membrane-binding is more complex than merely relief of auto-inhibition. This is most evident with activity analysis of truncated CCTs lacking domain M- or the AI helix. These mutations increase catalytic efficiency of soluble CCT approximately 10-fold compared to full-length soluble CCT (55,68). However, membrane binding of full-length CCT increases catalytic efficiency by about 200-fold (40,68). Thus, membrane binding is an allosteric event that triggers shifts in the conformational equilibrium that propagates from domain M to the domain C.

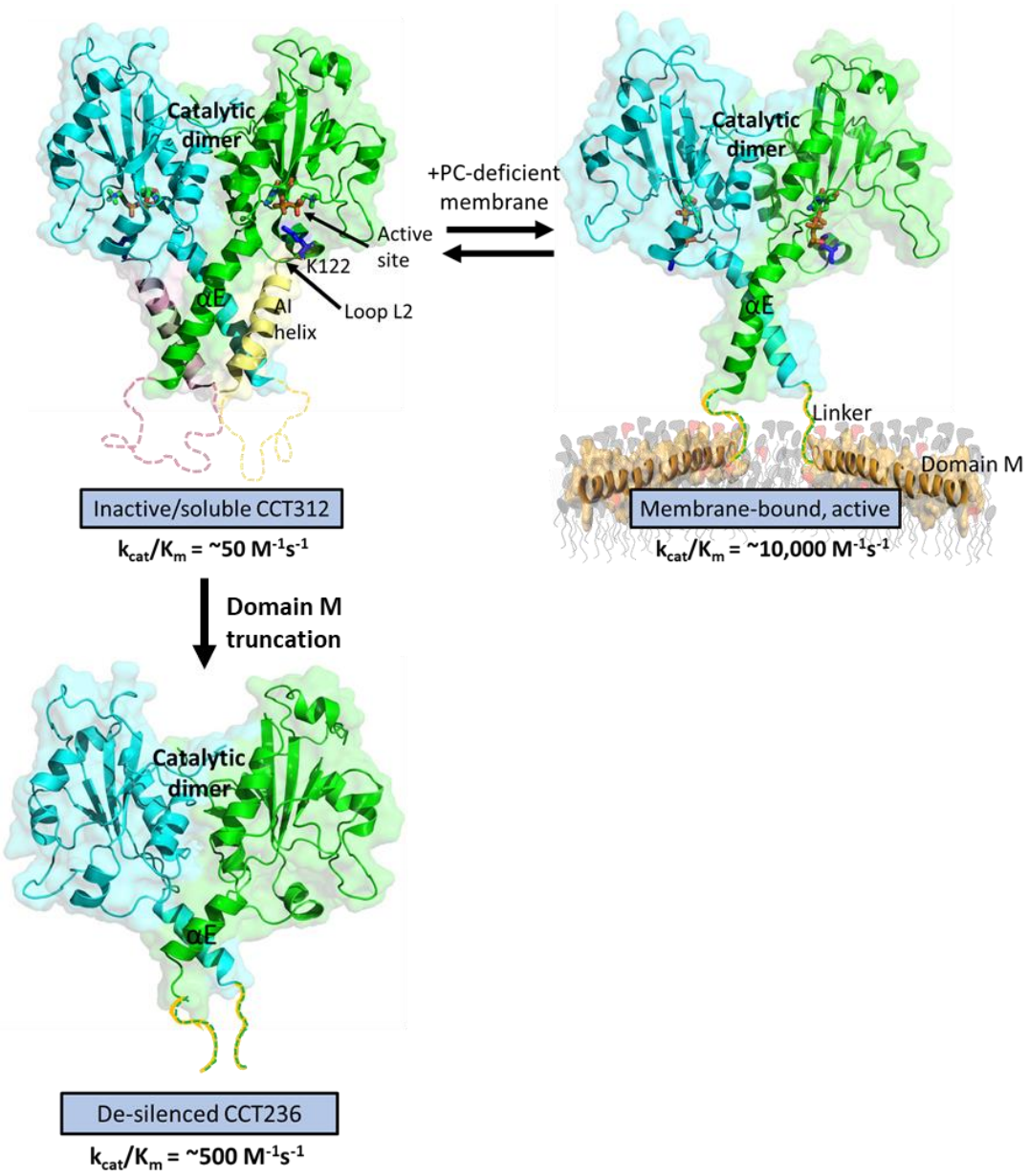

Figure 1.9. *The structure of CCT is solved for the soluble/inactive form but not for the membrane-bound/active form.* The solved structure of soluble/inactive CCT312 Δ18, containing a truncated region P and flexible leash of domain M (top left, PDB: 4MVC, (60)) is shown with CDP-choline in the active site. Loop L2, housing the key catalytic residue K122, is also labeled. The top right depicts a hypothetical membrane-bound CCT with "extended" αE helices (derived from a pre-equilibrated structure of CCT's catalytic domain in the absence of AI helices from simulations by Ramezanpour and Lee, *et al*. (69)) with the NMR structure of domain M embedded in lipid (PDB: 1PEI/1PEH, (22)). Also displayed is the crystal structure of CCT-236 (domain M-truncated, PDB: 3HL4, (70)). The dashed lines at the C-terminus represent 20 unresolved amino acids.

1.3.6. Enhanced αE dynamics likely plays a role in activation of membrane-bound CCT

What conformational shifts occur in CCT specifically during membrane docking of domain M that promote catalysis? While there is no solved structure of a membrane-bound CCT, there are a few pieces of structural information we can deduce about the membrane-bound, fully-active conformation. First, there are solved NMR structures of domain M peptides bound to SDS, a membrane mimetic (22). These structures confirm an α-helical conformation for residues 242 - 288. Second, chymotrypsin digestion patterns do not change drastically when CCT is bound to lipids (71), suggesting there is no drastic, global reorganization of domain C. However, crosslinking experiments do show that there are some changes in the dimer interface upon membrane binding (72). Third, crystal structures of CCT-312 (with domain M) (60) and CCT-236 (domain M truncated) (52) reveals that the C-terminal portion of αE (αE_C) is less structured with the removal of AI helix contacts. This suggests that the αE_C requires stable molecular interactions to maintain its helical structure and may forge new interactions in membrane-bound CCT. Fourth, the high level of sequence conservation of the αE_C compared to the AI helix suggests that the αE_C is involved in other protein-protein interactions beyond the less-specific hydrophobic interactions of the 4 helix complex.

Secondary structure and disorder predictions suggest that the αE has a flexible pivot point (hinge), dividing the helix into αE_N and αE_C. Residues 212-215 in the middle of αE is the only region of the sequence without a strong helical prediction (40). In fact, a helical break was observed at this site in one monomer of the solved CCT236 structure (52), suggesting that the absence of the AI helix allows this αE helix “bending”. During the progress of my thesis, new information emerged about the dynamics of the αE. Molecular dynamics simulations revealed a possible conformation of αE in active CCT (69) (**Fig. 1.10**). This conformation involves a bend around the putative hinge region that allows contacts between the αE_C and domain C of the other monomer. The interactions observed in the simulations include close association between Y213/Y216 in the αE and F124 in loop L2, forming a hydrophobic (aromatic) cluster. Interestingly, in 5 out of 10 simulation replicates the conserved R223 at the very C-terminal of αE_C re-oriented far enough to form contacts with the γ-phosphate of CTP substrate in the active site. The bent αE helices were stabilized for up to 700 ns during the 1000 ns simulations. *In vitro* evidence supporting this αE conformation as the active form of CCT comes from

“straight-jacketing” the αE helices with chemical crosslinks (69). When the helices are constrained from bending, activation by lipids was impaired. These simulations and cross-linking data provided a basis for interpretation of the results in this thesis. One caveat of the simulations is that the C-terminal 8 residues of the αE were constrained to remain helical. Thus, there is a lack of information about the conformational preferences of this segment that appears to be so critical for stimulation of catalysis.

If the αE helices are signal transducers, then one would expect their function to be sensitive to mutation at multiple sites. Recent mutational analysis revealed high mutational sensitivity to conserved residues in αE (Taneva, *et al.*, unpublished). Of particular interest were two mutations in the hinge region between αE_N and αE_C: Y213F and D214A. These mutations had reduced lipid activation in the context of CCT-312 but they had no effect on CCT-236 activity. This suggests that this hinge region plays a critical role in domain M-mediated CCT activation. Furthermore, mutation of Y213 to smaller amino acids (G, T, or A) increased CCT’s catalytic efficiency in the absence of lipids (likely by destabilization of the 4-helix complex) but decreased the efficiency in the presence of lipids. It therefore appears that both the bulky aromatic group and the hydroxyl of tyrosine are important for lipid activation. This supports simulation data in which bending of the αE helices at the hinge promotes contacts between the hydroxyl of Y213 and the backbone of F124 in loop L2, as well as forming an aromatic cluster with F124 and Y216 side chains. Other mutations in the hinge and αE_C regions (or immediately after this sequence) had moderate/strong negative effects on activity in the absence and presence of lipids (eg. D212A, Y216A, G224A), further implicating the region as an important regulator of CCT function.

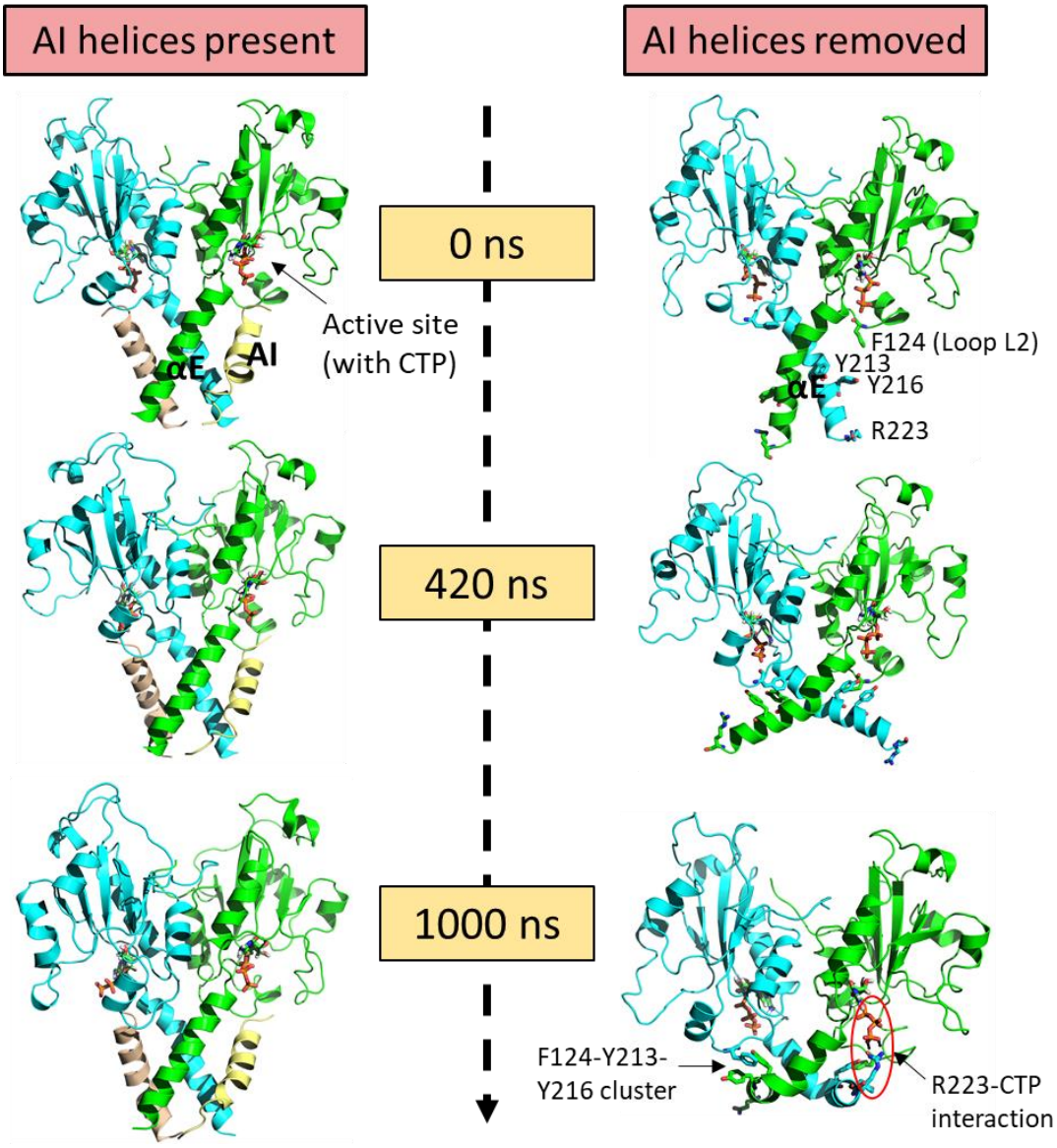

Figure 1.10. *Molecular dynamics simulations by Ramezanpour et al. reveal increased αE malleability with the removal of autoinhibitory (AI) helices.* Simulations were performed using the silenced CCT crystal structure (4MVC) as starting coordinates both in the presence and absence of the AI helices (69). Constraints were applied to the C-terminal 8 residues of the αE helices (αE_C) to maintain secondary structure and simulations were run for 1000 ns, with CTP in the active site in the simulation with AI helices removed (right side). Labeled simulation timepoints include a 40 ns pre-equilibration step of the structure/solvent.

1.3.7. CCT's interdomain linker may play a pivotal role in transducing membrane-binding signals

One final region of CCT that likely plays a pivotal role in the activation mechanism of CCT is the flexible linker region between domain C and domain M. After the αE_C sequence there is a predicted, conserved turn (^{223}RGY^{225}). This turn is resolved in a low-resolution structure of soluble CCT-312 (60). Also, Y225 is highly solvent exposed and susceptible to proteolysis in soluble and membrane-bound CCT (71), suggesting this short sequence is deficient in peptide backbone H-bonding. Following this turn is a sequence of approximately 10 residues that have never been resolved in any CCT structure, CCT's interdomain linker. Little is known about the structure and function of this interdomain linker (^{226}TAKELNVSF^{234}). It is a highly conserved sequence (**Fig. 1.11**), essentially to the same extent as domain C. There are both charged and hydrophobic residues, suggesting possible membrane affinity. Both the αE_C and linker sequences are only present/conserved in lipid-regulated CTs (**Fig. 1.11**). My hypothesis is that this interdomain linker is an allosteric transducer of activating signals from domain M to domain C and key, conserved residues are important for stabilizing a certain conformation of this linker and the αE helices (possibly a bent conformation).

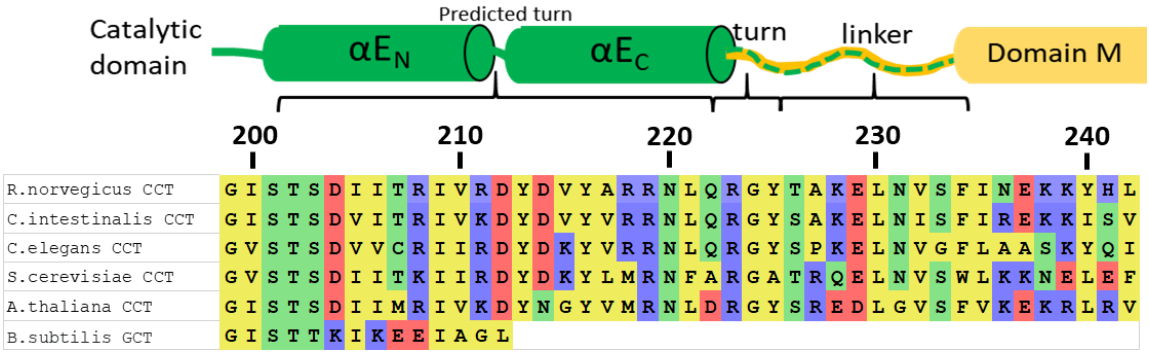

Figure 1.11. *The interdomain linker of CCT is highly conserved.* Sequence alignment of αE-linker sequence of lipid-regulated eukaryotic CCTs along with a non-lipid-regulated bacterial CT (Glycerol-3-phosphate cytidylyltransferase) generated using ClustalX2. Eukaryotic sequences are ordered with a decreasing degree of relatedness to rat CCT (the sequence used in this study). UniProt accession: *R. norvegicus* (rat; P19836), *C. intestinalis* (sea squirt; A0A1W2WNC7), *C. elegans* (nematode; Q3HKC4), *S. cerevisiae* (yeast; P13259), *A. thaliana* (flowering plant; Q9ZV56), and *B. subtilis* (bacteria; P27623).

1.4. Fluorescence-based approaches are valuable for studying protein structure

To probe the linker-membrane interaction and test the physiological validity of the bent αE helices models, I relied heavily on fluorescence-based approaches. When light of a specific wavelength is absorbed by molecules called fluorophores, an electron can transition to a higher-energy state (excited orbital) (73). If the excited electron is paired (possesses an opposite spin) with an electron in the lower-energy state (ground-state orbital), the rapid return of the electron to the ground-state orbital is accompanied by the release of a photon of a specific wavelength (fluorescence) longer than the incident light. The amount of fluorescence emitted by an excited fluorophore can be detected by a photomultiplier tube, which detects photons and amplifies and transduces the light signal as a measurable electronic signal.

Fluorophores are typically aromatic molecules. The fluorophore used in my experiments is the native amino acid, tryptophan (Trp), which has the highest extinction coefficient of the three aromatic amino acids (i.e. it absorbs light the strongest), making it generally the dominant fluorophore in Trp-containing proteins (73). 280 nm light, commonly used to excite proteins, is absorbed by Tyr and Trp but not Phe. Tyr emits light near 303 nm. Trp emission wavelength is slightly more complex. The Trp emission

maximum is largely dependent upon polarity/solvent-exposure of its local environment, varying in a ~40 nm range (74). In water the emission maximum is near 350 nm, however the emission maximum for a Trp that is protected from polar solvent will be blue-shifted (shorter wavelength) compared to a solvent-exposed Trp. Solvent-protection also increases the intensity of Trp fluorescence. Polar solvents only have substantial effects on the emission spectra of polarizable fluorophores because the decrease in emission energy (or increase in wavelength) is caused by dipole-dipole interactions between the excited fluorophore and the solvent molecules. During excitation, solvent molecules organize around the enhanced dipole of the excited-state fluorophore, lowering the excited-state energy. Trp fluorescence can also be quenched by a number of polar amino acid side chains (74). Thus, tryptophan is an extremely useful fluorophore for monitoring local structural changes that occur in proteins with multiple states.

1.4.1. Fluorescent quenchers reveal information about fluorophore solvent- and lipid-exposure

Certain molecules called collisional quenchers can collide with excited fluorophores to deactivate them, returning the electron to ground-state without the emission of a photon (73). Another type of quenching, called static quenching, results from the fluorophore and quencher forming a complex which is non-fluorescent. A quencher can act as both collisional and static. Exciting fluorophores in the presence of these quenchers results in lower overall fluorescence intensity. To monitor the quenching of Trp fluorescence by quenchers in the solvent and lipid phases, I used the soluble quencher acrylamide and the halogen quencher bromine conjugated to PC acyl chains (brominated PC or BrPC). I assumed that these quenchers were acting on Trp using primarily a collisional mechanism. The mechanism of Trp quenching by acrylamide likely involves an electron transfer from the indole that is only able to occur in the excited state (73). The mechanism of Trp quenching by bromine is likely a transfer of the excited electron from a singlet state (opposite spin as ground-state electron) to a triplet state (same spin as ground-state electron) (73). This transfer causes a slow emission rate that is not detected as fluorescence. Collisional quenching can be quantified using the equation:

$$\frac{F_0}{F} = 1 + K_{SV}[Q]$$

Where F_0 is the fluorescence in the absence of quencher, F is the fluorescence in the presence of quencher, Q is the concentration of quencher, and K_{SV} is the quenching constant (a measure of the degree of quenching). Therefore, a plot of F_0/F vs. [Q] with a y-intercept of 1 is typically linear with a slope of K_{SV}.

Quenching requires contact of the quencher and fluorophore (73). Because of this, quenching becomes insignificant beyond several angstroms (~3-5 Å) between the quencher and fluorophore. I used increasing concentrations of acrylamide and the formula above to monitor the exposure of Trps in several single-Trp CCT mutants to molecules in the solvent. The lower the K_{SV} value, the less collisions with acrylamide in the solvent are occurring, thus the more protected a Trp is from the solvent. I used lipid vesicles containing BrPC to monitor the extent of interaction between different Trps and the lipid acyl chains. I used BrPC with bromines conjugated to carbons 6,7 (shallowest), 9,10, or 11,12 (deepest) to probe three different bilayer depths. Previously, X-ray diffraction experiments with BrPCs in stacked multilayers have estimated these bromine positions as ~3.5, 6.5, and 8 Å from the acyl chain-headgroup boundary (75,76). The diffraction experiments also revealed that different BrPCs alter bilayer thickness by less than 1 Å compared to POPC (75), suggesting the conjugated bromines have similar effects on acyl chain dynamics as an acyl chain double bond. Therefore, POPC is a good (non-quenching) physical mimic of dibrominated PC and was used as the reference lipid. Collisional quenching by any of these bromine positions in a bilayer system would require association with the lipid (75-77). In my experiments, I utilized small, high curvature vesicles with a potential level of disorder in the bilayer that allows quenching of Trps by BrPCs that may not form a stable membrane interaction but merely come within proximity of the membrane surface.

1.4.2. FRET can monitor membrane approach of specific protein sites

Fluorescence resonance energy transfer (FRET) is used widely to monitor the molecular distances between two different fluorophores. The FRET fluorophore pair consists of a donor (which is excited by incident light) and an acceptor (which is in the ground-state) (73). Donor and acceptor pairs are chosen based on the absorbance and emission wavelength spectra. The donor absorbs light at a lower wavelength than the acceptor, and the donor's emission spectra and the acceptors absorbance spectra must overlap, as this condition reflects the fluorophores electronic oscillations being "in

resonance". When this condition is met, there can be a non-radiative energy transfer (no donor photon released) from donor to acceptor fluorophore (FRET). This energy transfer is the result of through-space dipole-dipole interactions between the fluorophores. The result is a decrease in donor fluorescence and an increase in acceptor fluorescence, both of which can be monitored to quantify FRET. Typically, the percent decrease in donor fluorescence (from a maximum fluorescence in the absence of acceptor) when acceptor is present is defined as the FRET efficiency. The level of FRET (efficiency) is determined by a few factors: the degree of spectral overlap of donor emission and acceptor absorbance, the quantum yield of the donor (number of photons that are emitted per number of photons absorbed), orientation of donor and acceptor dipoles, and the distance between donor and acceptor fluorophores (73). The first three factors determine the Förster distance (R_0) constant for each donor-acceptor pair, which is defined as the donor-acceptor distance at which FRET is 50% of maximum. The fourth factor, donor-acceptor distance, is the most dominant determinant of FRET efficiency. Therefore, monitoring donor fluorescence decrease when acceptor is added, or monitoring acceptor fluorescence increase as donor is added are both effective methods for monitoring donor-acceptor distances. In a single donor to single acceptor system, the relationship between donor-acceptor distance (r) and FRET efficiency (E) is defined as:

$$E = \frac{1}{1 + \left(\frac{r}{R_0}\right)^6}$$

I used FRET to monitor the relative distances between different Trp sites (donor) and dansyl fluorophore (acceptor) conjugated to PE headgroups (dansyl-PE) in lipid vesicles. Since the Trp donor can transfer energy to multiple potential dansyl acceptors (surface density of acceptors representing the membrane surface), the above equation cannot easily be used to calculate distances between Trp and dansyl. Therefore, the data from my FRET experiments are largely used to monitor relative distances to the membrane surface for different Trp sites.

1.5. Research aims

The general aim of this research was to determine the role of the interdomain linker of CCT in the lipid-induced activation mechanism. More specifically, the goals were to:

1. To determine if the αE_C and/or linker interact with the membrane.
2. To determine if disruption of linker-membrane interactions blocks activation.
3. To determine the relative distance between the membrane surface and sites in the linker, αE, and catalytic domain.
4. To determine if the linker is instrumental in stabilizing a bent αE helix that draws the catalytic domain close to the membrane surface.
5. To determine if the linker directly interacts with αE to promote an activating conformation in the αE helices.

Chapter 2. Experimental Procedures

2.1. Materials

Pfu DNA polymerase, 10X polymerase buffer/$MgSO_4$, and DpnI restriction enzyme were from Thermo Fisher. dNTPs and SYPRO Orange dye (5000X) were from Invitrogen. Primers were from Integrated DNA Technologies. TOP10 and Rosetta competent *E. coli* cells were originally from Novagen. Ampicillin, chloramphenicol, CTP, CDP-choline, and imidazole were from Sigma. [^{14}C-Me]-phosphocholine was from Perkin Elmer. Kanamycin, DTT, and IPTG were from Bioshop. All protease inhibitors were from Sigma. Dialysis tubing was from Spectrum LifeSciences (12-14 kDa MWCO). Ni-NTA agarose beads were from Qiagen. All phospholipids (POPC, eggPG, diBrPC 6,7/9,10/11,12, and dansyl-PE) were from Avanti Polar Lipids.

2.2. Generation of His-tagged CCT mutants

CCT sequences were derived from Rattus norvegicus CCT α isoform (UniProt accession P19836). All CCT constructs were generated by Quikchange site directed mutagenesis (Qiagen) using complementary primers and the templates described next.

2.2.1. Templates for Mutagenesis of pET24a-CCT312-His

Mutations in CCT312 were performed using pET24a-CCT312-His template, encoding a C-terminal His6-tag (^{313}LEHHHHHH^{320}). This template was constructed before my thesis work as described by Ramezanpour and Lee, *et al*. (69). Previously, CCT constructs with N-terminal His-tags were co-purified on Ni-agarose columns with proteolyzed CCT fragments cleaved near the C-terminus. Switching the His-tag to the C-terminus prevented the retention of these fragments on columns as their His-tags would also be cleaved. This switch produced cleaner preparations without truncated CCT present that may skew results. Previously, vesicle cross-bridging experiments revealed the nuclear localization signal (NLS) as a second vesicle-binding motif of CCT, independent of domain M (51,78). The NLS (^{12}RKRRK^{16}) was deleted in all constructs to prevent lipid vesicle cross-bridging and sample turbidity in fluorescence experiments. **Appendix A** provides data showing how deleting the NLS alleviates turbidity generation.

For generation of single tryptophan mutants used in fluorescence assays, two native tryptophans were first mutated to phenylalanine (W151F and W278F). For mutants used in activity assays, W151 was retained.

2.2.2. Templates for Mutagenesis of pET14b-His-CCT236

Mutations in CCT236 were performed using pET14b-His-CCT236 template, encoding an N-terminal His6 tag ($^{-19}$MGSSHHHHHHSSGLVPRGSH^{0}). This template was constructed before my thesis work as described by Taneva, et al. [3]. The nuclear localization signal was deleted (^{12}RKRRK^{16}) in all constructs. The native tryptophan at 151 was retained in mutants used for activity assays and mutated to phenylalanine (W151F) in mutants used for fluorescence assays.

2.2.3. Mutagenesis, Cloning and purification of pET24a-CCT312-His and pET14b-His-CCT236 mutagenesis products

I designed the primers for QuikChange mutagenesis using the following guidelines: $T_m \geq 81.5$ (based on: $T_m = 0.41$(%GC content) − (675/(# of nucleotides)) − % mismatch), 25-45 base length, and at least 10 correct bases flanking the mutation site in the primers). Polymerase Chain Reaction set-up and thermocycler settings for site-directed mutagenesis can be found in **Appendix B**. PCR product plasmids were incubated with 1 µL of FastDigest DpnI restriction enzyme for 1 h at 37°C to digest methylated template plasmid. 1-5 µL of mutagenesis products were transformed into competent TOP10 *E. coli* by incubation on ice for 30 min followed by a 42°C heat shock for 30 sec and a second incubation on ice for 5 min. Transformed cells were spread on agar plates. For pET24a-CCT312-His constructs, plates contained 50 µg/mL of kanamycin to select for the kanamycin resistant pET24a. For pET14b-His-CCT236 constructs, plates contained 100 µg/mL of ampicillin to select for the ampicillin resistant pET14b. Plated cells were grown overnight (12-16 h) at 37°C. Typically there were ~30-50 colonies vs. 0 in the control plate transformed with dd$H_2$0. 5 mL of Lysogeny broth (LB) was inoculated with a single bacterial colony and agitated overnight (225 rpm for 12-16 h) at 37°C. LB was supplemented with the same antibiotics as above. Plasmid purification was performed using a QiaPrep Spin Miniprep Kit from Qiagen, as per manufacturer protocol (79). The concentration of purified plasmids were measured using a Nanodrop ND-1000 Spectrophotometer and DNA sequences of CCT constructs

(primed from the T7 terminator site) were analyzed by external sequencing (Eurofins Scientific) to confirm the presence of the engineered mutation as well as an absence of any non-solicited mutations.

2.3. Expression and purification of CCT312-His and His-CCT236

2.3.1. Expression of CCT312-His and His-CCT236 in *E. coli*

Purified pET24a-CCT312-His and pET14b-His-CCT236 constructs were transformed into competent Rosetta *E. coli* cells as described above except the 42°C heat shock was for 45 sec. The expression of the transgene within pET vectors is controlled by an IPTG-inducible bacteriophage-derived T7 RNA polymerase promoter. Transformed cells were spread on agar plates. For pET24a-CCT312-His constructs, plates contained 50 µg/mL of kanamycin and 34 µg/mL of chloramphenicol. For pET14b-His-CCT236 constructs, plates contained 100 µg/mL of ampicillin and 34 µg/mL of chloramphenicol. Plated cells were grown overnight (12-16 h) at 37°C. 5 mL of Lysogeny broth (LB) was inoculated with a single bacterial colony and agitated overnight (225 rpm for 12-16 h) at 37°C. LB was supplemented with the same concentrations of antibiotics as described above. For large-scale expression, 1 mL of overnight liquid culture was added per 100 mL LB media (typically 400 mL total) containing antibiotics. Large-scale cultures were agitated (225 rpm) at 37°C until the optical density (absorbance at 600 nm) reached 0.45-0.55. At this point, Isopropyl β-D-1-thiogalactopyranoside (IPTG) was added to a final concentration of 1 mM. Cultures were agitated for an additional 3 h at 37°C (for CCT312-His) or room temperature (for His-CCT236) to allow adequate expression of the exogenous CCT. After expression, cells were harvested by centrifugation at 4500 RCF (g) for 15 min and frozen at -80°C.

2.3.2. Small-scale cell partitioning

High-level expression of exogenous soluble proteins in bacteria can result in the formation of insoluble protein aggregates called inclusion bodies. I utilized modified CCT purification protocols depending on whether the mutant was expressed in soluble form, in inclusion bodies, or in both. To determine this cellular localization of CCT, 1 mL aliquots of uninduced and IPTG-induced *E. coli* were separately saved during the large-

scale CCT expression step. The aliquot was centrifuged at 13000 RCF (g) for 5 min. The liquid media was removed and each cell aliquot was resuspended in 200 µL of lysis buffer (150 mM NaCl, 20 mM NaPi, 1% Triton, 2 mM DTT, protease inhibitors, 0.01 mg/mL DNase I, pH = 8.0) and incubated on ice for 5 min. See **Appendix C** for a list of protease inhibitors used and working concentrations. The cells were then sonicated on ice for 10 sec (x3) to form a cell homogenate. 20 µL of this homogenate was removed and the remaining 180 µL was centrifuged at 13000 RCF (g) at 4°C for 15 min. The cell supernatant (soluble cell fraction) was collected and the pellet (insoluble cell fraction) was resuspended in 180 µL of lysis buffer by sonication for 10 sec (x3). 10 µL of uninduced and IPTG-induced cell homogenate, supernatant, and pellet were analyzed by SDS-PAGE.

2.3.3. Cell partitioning and purification of *E. coli*-expressed CCT312-His and His-CCT236

Based on small-scale cell partitioning analysis, CCT312-His mutants were purified from either the insoluble cell pellet fraction or the whole cell lysate. His-CCT236 mutants were purified from the soluble cell supernatant fraction. **Appendix D** lists all CCT mutants purified and the cell fraction from which they were purified.

2.3.3.1. Purification of CCT312-His from insoluble cell pellet

E. coli cells harvested from 200mL of LB media after large-scale expression were thawed on ice for 15 min and re-suspended in 5 mL of lysis buffer and incubated on ice for 5 min. The cells were sonicated 3 x 30 sec followed by addition of 5mL of lysis buffer, sonicated 2 x 30 sec followed by addition of 10mL of lysis buffer, sonicated for a final 30 sec (all on ice). This cell homogenate was centrifuged at 13000 RCF (g) for 30 min at 4°C. The cell supernatant (soluble fraction) was poured off and the cell pellet (insoluble fractions) was washed twice by re-suspending in lysis buffer (20 mL for first wash and 10mL for second wash), sonicating for 30 sec, and centrifuging at 15000 RCF (g) for 15 min at 4°C. The washed cell pellet was denatured (resolubilized) in 10 mL of denaturation buffer (6 M GnHCl, 500 mM NaCl, 50mM NaPi, 25 mM imidazole, 1 mM DTT, pH = 8.0) by intermittent vortexing at room temperature for 1 h. The resolubilized pellet was centrifuged for 20 min at 13000 RCF (g) at room temperature. The supernatant of the centrifuged resolubilized cell pellet was loaded onto a Ni-NTA-agarose column (3-5 mL packed beads that had been pre-washed with denaturation

buffer) at room temperature, and the flow-through was collected and reloaded on the column for a second flow-through. The bead-bound CCT was washed with 20 mL aliquots of denaturation buffer with decreasing concentrations of urea (6M, 5M, 4M, 3M, 2M, 1M, 0M urea in 500mM NaCl, 50mM NaPi, 25mM imidazole, 1mM DTT, pH = 8.0;) to renature the protein on the column. CCT was eluted from the column with elution buffer 1 (10 mM Tris, 150 mM NaCl, 100 mM imidazole, 2 mM DTT, pH = 8.0) followed by elution buffer 2 (10 mM Tris, 150 mM NaCl, 350 mM imidazole, 2 mM DTT, pH = 8.0).1 – 3 mL elution fractions were collected (depending on expression levels). Elution fractions were pipetted into dialysis bags with 12-14 kDa cutoff and dialyzed for 3 h, changing the dialysis buffer (10 mM Tris, 200 mM NaCl, 2 mM DTT, pH = 7.4) every 45 min. 10 µL of each elution fraction was analyzed by SDS-PAGE to determine relative CCT concentrations. Dialyzed elution fractions were spun for 10 min at 13000 RCF (g), the most concentrated fractions were pooled, and this pool was stored at -80°C.

2.3.3.2. Purification of CCT312-His from denatured whole cell pellet

E. coli cells harvested from 200mL of LB media after large-scale expression were thawed on ice for 15 min and re-suspended in 5 mL of lysis buffer and incubated on ice for 5 min. The cells were sonicated 3 x 30 sec on ice. The 5 mL lysed cell homogenate was added to 50 mL of Triton-containing denaturation buffer (6 M GnHCl, 500 mM NaCl, 50mM NaPi, 25 mM imidazole, 1% Triton, 1 mM DTT, pH = 8.0). This denatured whole cell pellet was gently mixed for 1 h at room temperature and centrifuged at 13000 RCF (g) for 30 min. The supernatant was added to a Ni-NTA agarose column at room temperature and the CCT was isolated as described above.

2.3.3.3. Purification of His-CCT236 from soluble cell supernatant

In this protocol, the lysate (20 mL) was separated into soluble and insoluble fractions by centrifugation at 13000 RCF (g) for 15 min at 4°C. Prior to this spin I added 1.6 mL of 10X binding buffer (5 M NaCl, 50 mM NaPi, pH = 8.0) to 20 mL lysate. This step raises the ionic strength and leads to higher retention of CCT in the soluble fraction (80). The resulting cell supernatant was added to a Ni-NTA-agarose column at room temperature. 10 mL aliquots (x 3) of wash 1 (500 mM NaCl, 50 mM NaPi, 25 mM imidazole, 1 mM DTT, pH = 8.0) were applied to the column followed by 10 mL aliquots (x 3) of wash 2 (100 mM NaCl, 50 mM NaPi, 25 mM imidazole, 1 mM DTT, pH = 8.0). CCT was then eluted and dialyzed as described above.

2.4 Determining protein concentration

The concentration of purified CCT pools was determined by the Bradford assay (81). Protein samples were diluted up to 20 µL with ddH20 and 200 µL of Bradford reagent (81) was added, followed by immediate vortexing. Samples were incubated at 37°C for 15 min and absorbance was read at 595 nm. Bovine serum albumin (BSA) of known concentration was used to create a standard curve (0 – 10 µg of BSA) from which CCT concentrations were interpolated. The background absorbance was subtracted from absorbance of CCT using the spent dialysis buffer aliquots instead of CCT.

2.5 Preparation of small unilamellar lipid vesicles

Phospholipid stocks (dissolved in organic solvent) were added to a 5 mL round-bottom flask in calculated volumes depending on target vesicle concentration (1 – 2 mM) and lipid composition. The concentrations of the phospholipid stocks were determined by phosphorus analysis (82). The organic solvent was evaporated with a rotary evaporator by rotating the flask in a warm water bath under vacuum for 20 min. The dried lipids were resuspended in 1 mL of 10 mM Tris (pH = 7.4) by vortexing and sonicated on ice for 15 min using a probe sonicator set at 50% output and a setting of 1.0. The sonicated vesicles were centrifuged at 13000 RCF (g) at 4°C for 5 min to remove residual titanium introduced by the sonicator probe. The vesicles were stored under argon at 4°C and used within 2 days.

2.6 Fluorescence quenching of tryptophan by dibrominated PC and acrylamide

2.6.1. Quenching of single-tryptophan CCT mutants by dibrominated PC

Vesicles were prepared containing 50% eggPG and 50% PC. Non-quenching vesicles contained POPC while quenching vesicles contained dibrominated PC with bromines conjugated to carbons 6 and 7 (BrPC 6,7), 9 and 10 (BrPC 9,10), or 11 and 12 (BrPC 11,12). Pilot experiments were carried out using lower concentrations of BrPC but I obtained poorer quenching than with 50% BrPC. Fluorescence samples (300 µL) were prepared by mixing 3 µM of CCT and 450 µM of vesicles in buffer (10 mM Tris, 150 mM

NaCl, 2 mM DTT, pH = 7.4) and incubating for 5 min at room temperature. Fluorescence scans were measured at 20°C on the Cary Eclipse Fluorescence Spectrophotometer. The excitation wavelength was set to 295 nm (to minimize tyrosine excitation) with a 5 nm excitation slit and the emission was scanned from 305 nm to 420 nm with a 10 nm emission slit and a scan rate of 120 nm/min. The intensity vs. wavelength data was imported into Excel. Two scans were averaged and lipid blanks (containing spent dialysis buffer instead of CCT) were subtracted to generate corrected fluorescence emission spectra. To determine peak fluorescence, the emission wavelength that produced the highest signal was averaged for each set of emission spectra obtained for a given Trp mutant and the fluorescence values at this averaged wavelength for each individual emission curve was recorded. The ratio of fluorescence intensity maxima of the single Trp-containing CCTs in the presence of non-quenching vs quenching vesicles was calculated using the corrected spectra to determine the degree of quenching.

2.6.2. Quenching of single-tryptophan CCT mutants by acrylamide

Vesicles were prepared containing 50% eggPG and 50% POPC. Fluorescence samples were prepared by mixing 3 μM of CCT and either 0 μM or 450 μM of vesicles in buffer (10 mM Tris,150 mM NaCl, 2 mM DTT, pH = 7.4) and incubating for 5 min at room temperature. After scanning each sample using the same fluorimeter parameters as for BrPC quenching, the 300 μL from the cuvette was pipette-mixed in a microfuge tube containing 6 μmol of dried-down acrylamide to bring the acrylamide concentration in the sample to 20 mM. A Trp fluorescence scan was obtained and the acrylamide addition was increased again. This cycle was continued in 20 mM increments until a final acrylamide concentration of 120 mM was reached. This was done for both the vesicle-free and vesicle-containing samples. Lipid and buffer blank spectra were subtracted to generate corrected emission spectra. The fluorescence intensity maximums were used to generate linear plots of unquenched/quenched fluorescence vs. concentration of acrylamide for each single-Trp CCT construct. The slopes of these plots were reported as the Stern-Volmer quenching constants (K_{SV}) in the absence and presence of vesicles. R^2 values of all acrylamide quenching plots were >0.9.

2.7. Tryptophan-DansylPE FRET

2.7.1. Monitoring increases in Dansyl fluorescence

Vesicles were prepared containing 1% dansylated PE (49% eggPG, 50% POPC). Fluorescence sample tubes were prepared by mixing 100 μM of vesicles with 0-4 μM of CCT in buffer (10 mM Tris,150 mM NaCl, 2 mM DTT, pH = 7.4) and incubating for 5 min at room temperature. The excitation wavelength was set to 280 nm to maximize donor tryptophan excitation and the emission scan was read from 290 nm to 590 nm. The remainder of the fluorimeter settings were identical to the Trp quenching experiments. For each sample, the fluorescence intensity at 520 nm (Dansyl emission) was monitored and a FRET efficiency value was calculated based on intensity increases at this wavelength ((F_{DA}/F_A) - 1), with F_{DA} as acceptor fluorescence in the presence of donor and F_A as acceptor fluorescence in the absence of donor. FRET signals produced with each single tryptophan mutant were plotted as (F_{DA}/F_A) – 1 vs. donor:acceptor molar ratio and the data was fit to a one-site binding hyperbola fit using GraphPad Prism 4.

FRET experiments monitoring dansyl fluorescence used samples with donor:acceptor molar ratios ranging from 0:1 to 4:1 and lipid:protein molar ratios ranging from 100:1 – 25:1 (individual phospholipids per domain M). Preliminary FRET experiments with varied CCT concentration ranges, vesicle concentrations, and % dansyl-PE vesicle compositions were important to determine the parameters that produced optimal FRET signals. A challenge in experimental design is to improve the signal to noise ratio, while capturing the small differences between Trp sites. These experiments were initially carried out on select Trp mutants with 50 μM, 100 μM, or 200 μM vesicles. With 200 μM vesicles, FRET signals were very low for 1%, 2.5%, and 5% dansyl-PE compositions, and there was concern with light scattering interference from the high vesicle concentration. 50 μM vesicles produced high FRET signals but only at high CCT concentration. 100 μM vesicles also produced discernable FRET signals and so this concentration was chosen. A range of 0 – 2 μM of CCT did not produce FRET signals that could be differentiated between different Trps, therefore, a range of 0 – 4 μM of CCT was chosen. Dansyl-PE compositions above 1% (with 100 μM vesicles) also produced very low FRET values and therefore, 1% dansyl-PE composition was chosen.

Since dansyl fluorescence increases with increasing [CCT] were measured directly from the raw spectra, the titrated CCT may have contributed to some of the signal observed at 520 nm. To assess this possibility, I monitored fluorescence signal of 0 – 4 μM CCT at 520 nm for all the single-Trp mutants analyzed in the FRET experiments. Signal increases were negligible up to 4 μM of CCT and so this background signal was not taken into account.

2.7.2. Monitoring decreases in tryptophan fluorescence

Vesicles were prepared containing 0%, 2.5%, 5%, or 10% dansylated PE (50%, 47.5%, 45%, or 40% eggPG, 50% POPC). Fluorescence sample tubes were prepared by mixing 100 μM of vesicles with 1 μM of CCT in buffer (10 mM Tris,150 mM NaCl, 2 mM DTT, pH = 7.4) and incubating for 5 min at room temperature. The excitation wavelength was set to 290 nm to maximize donor tryptophan excitation and the emission fluorescence was monitored from 300 nm to 420 nm. The remainder of the fluorimeter settings were identical to the Trp quenching experiments. The 2 scans were averaged and lipid blank scans (containing last dialysis buffer instead of CCT) were subtracted to generate fluorescence emission curves. For each tryptophan mutant and % Dansyl PE, the fluorescence intensity maximum was noted and a FRET efficiency value was calculated based on intensity decreases at this wavelength ($1 - (F_{DA}/F_D)$), with F_{DA} as donor fluorescence in the presence of acceptor and F_D as donor fluorescence in the absence of acceptor. FRET signals produced with each single tryptophan mutant were plotted as $1 - (F_{DA}/F_D)$ vs. acceptor:donor molar ratio and the data was fit linearly using GraphPad Prism 4.

FRET experiments monitoring Trp fluorescence used samples with acceptor:donor molar ratios ranging from 0:1 to 10:1 and a lipid:protein molar ratio of 100:1. A high degree of variation between FRET signals of single-Trp mutants was only observed for relatively high dansyl-PE % compositions (above 1%) and 50 μM vesicle concentrations produced low FRET signals. Therefore, 100 μM of vesicles was used with increasing dansyl-PE composition well above 1%.

2.8. CCT activity assay

Activity of CCT mutants was measured using a similar protocol as described previously [6]. A mixture of 20 mM Tris (pH = 7.4), 12 mM $MgCl_2$, 89 mM NaCl, 8 mM CTP, and 10 mM DTT was formed either in the absence or presence of 0 - 200 μM 50% eggPG / 50% POPC vesicles 0.1 μg of CCT (or identical volume of dialysis buffer) was added to this mixture and the tubes were placed in a 37°C water bath. The reaction was started with 1.5 mM [^{14}C]-phosphocholine (1 mCi/mmol) to bring the final reaction volume to 40 μL and gentle vortex. The tubes were agitated in the 37°C bath for 10 min and the reaction was stopped by addition of 30 μL of a 9:1 methonal:ammonia mix followed by vigorous vortex. The CCT-generated [14C]-CDP-choline product was separated from substrates using thin layer chromatography. 12.5 μL of carrier (60 mg/mL phosphocholine, 10 mg/mL CDP-choline) was spotted to enable visualization of CDP-choline as a band under UV light. 25 μL of each reaction was spotted on aluminum- or plastic-backed silica plates and the plate was placed in sealed tanks containing 90 mL of methanol:0.6 M NaCl: ammonia (5:5:1). Plastic-backed plates were sprayed with 0.02% dichlorofluorescein to visualize the CDP-choline band. The silica containing the band was scraped from the plate and re-suspended in scintillation cocktail solution before liquid scintillation counting to quantify the amount of product produced from each reaction. Disintegrations per min (dpm) values were obtained and the specific activity of CCT constructs (in the absence and presence of vesicles) was calculated as nmol of CDP-choline produced per min per μg of CCT, using the formula 1 nCi = 2220 dpm and a specific radioactivity of the ^{14}C-CDPcholine as 1.0 nCi/nmol.

2.9. Thermal denaturation of CCT using Sypro Orange dye

5 μM of CCT was mixed in buffer (10 mM Tris, 150 mM NaCl, 2 mM DTT, pH = 7.4) supplemented with 3x Sypro Orange (83) (diluted from 5000x stock). Thermal denaturation was monitored on the Cary Eclipse Fluorescence Spectrophotometer by excitation of the 300 μL sample at 492 nm (5 nm excitation slit) and monitoring Sypro emission at 595 nm (5 nm emission slit) every 0.5°C increment. The start temperature was 25°C and the temperature was increased to 65°C at a rate of 0.5°C/min. A first derivative plot of the intensity vs. temperature scan was computed by the fluorimeter software to generate the melting temperature of the CCT construct.

2.10. Chymotrypsin digestion of single-Trp mutants

1.5 µg of single-Trp CCT312-His constructs were added to buffer (10 mM Tris, 150 mM NaCl, 2 mM DTT, pH = 7.4) at 37°C. 1 µL of 0.02 µg/µL chymotrypsin (0.02 µg) was added to each sample to a final volume of 27 µL. The CCT:chymotrypsin molar ratio was ~25:1 (75:1 weight ratio). After 3 min of digestion at 37°C., PMSF (chymotrypsin inhibitor) was added to a final concentration of 2 mM to quench the reaction. After quenching, samples were incubated at 37°C for 30 sec, followed by addition of Laemmli buffer and boiling for 2 min. Digested samples were run on a 13% SDS-PAGE gel and bands were visualized by silver staining. “Pre-quenched’ reactions were also performed in which PMSF was added to the CCT mix before chymotrypsin.

Silver staining on SDS-PAGE gels from chymotrypsin experiments was performed using a modification of (84) by first fixing and removing SDS from the gel by agitation for 20 min in 50% methanol/10% acetic acid. The gel was incubated for 5 min (x3) in 15% methanol to wash and further remove SDS. The gel was then oxidized by incubation in 10% glutaraldehyde for 20 min. This was followed by a wash with 15% methanol for 5 min (x5) and rinse for 5 min in ddH20. The staining was performed by incubation for ~8 min in 0.047 M $AgNO_3$ (1 M NaOH, 7.5% NH_4OH). The gel was then rinsed for 6 min (x3) with ddH_20. The stained gel was developed by incubation with citric acid-formaldehyde developer (~0.26 mM citric acid, 3.7% formaldehyde). When the desired staining endpoint was seen, the developer was removed and stain development was halted by incubation with 1% acetic acid. Gels were stored in ddH_20.

2.11. FPLC gel filtration

Fast protein liquid chromatography (FPLC) gel-filtration experiments of CCTs and CCT-lysoPC micelle complexes were performed by Dr. Jaeyong Lee. The indicated CCTs were mixed with a 175~180 molar excess of LPC (16:0) in buffer (10 mM Tris (pH = 8), 300 mM NaCl, 2 mM DTT) and concentrated using an Amicon Ultra-spin filter (30kDa cut-off) at 4000 rpm to a protein concentration of 150 – 300 µM. Samples (0.4 mL volume) were applied to a Superdex 200 10/300 FPLC gel-filtration column (24 mL bead volume) pre-equilibrated with 10 mM Tris, pH 8, 0.1 M NaCl, and 2 mM DTT. The column had been pre-calibrated with the mass standards: Dextran, >2000 kDa; Vo; ferritin, 440 kDa; catalase, 220 kDa; BSA, 67 kDa; and ribonuclease, 13.7 kDa. The

FPLC-controlled flow rate was 0.4 mL/min and 1 mL volume fractions were collected. Lipid phosphorus was measured in duplicate (82) and the absorbance at 280 nm was measured for each elution fraction.

Chapter 3. Results

3.1. The αE_C and linker associate with the membrane during CCT activation

3.1.1. Preparation and characterization of single-Trp mutations

As there is no solved structure of lipid-bound CCT, the orientation of the CCT catalytic domain, αE, and linker relative to the membrane surface is not known. To assess whether sites in the αE and linker come into contact with the membrane surface, I used fluorescence quenching of CCT tryptophans (Trps) by vesicles containing brominated PC (BrPC). I engineered single Trps at two sites in the αE_C and four sites in the linker of CCT-312 (**Fig. 3.1**), a construct that includes all of the catalytic and M domains but lacks the phosphorylated P region. This CCT construct mimics full length, dephosphorylated CCT with respect to catalysis and regulation by lipids (51,60), and is used in all experiments in this thesis unless otherwise specified. The template for mutagenesis, CCT-312His Δ12-16, is explained in Section 2.2.1. The sites for mutagenesis substituted Trp for tyrosine or phenylalanine, except for three positions in the αE and linker where no aromatic amino acids were available (L221, L230, and V232). Single-Trp mutant preparations were highly pure after elution from Ni-agarose affinity columns as observed by SDS-PAGE (purity of mutants used in fluorescence experiments are shown in **Appendix E**). Select single-Trp variants subjected to limited chymotrypsin digestion produced unaltered patterns of proteolytic fragments, indicating no disruption of tertiary interactions (**Fig. 3.2**). The engineered Trps did not impair the interaction of the M domain with membrane vesicles. Lipid-dependence curves showed that all active αE/linker single-Trp mutants respond with approximately the same high affinity (EC_{50} =~1-4 μM) for the highly curved vesicles used in the fluorescence experiments (**Fig. 3.3**). Many of the single-Trp variants did not affect CCT activity. Of the few that did drastically impair activity (W230 and W232), the single Trp substitutions did not alter the transition temperatures for unfolding (**Table 3.1**), confirming that they do not destabilize the catalytic domain fold.

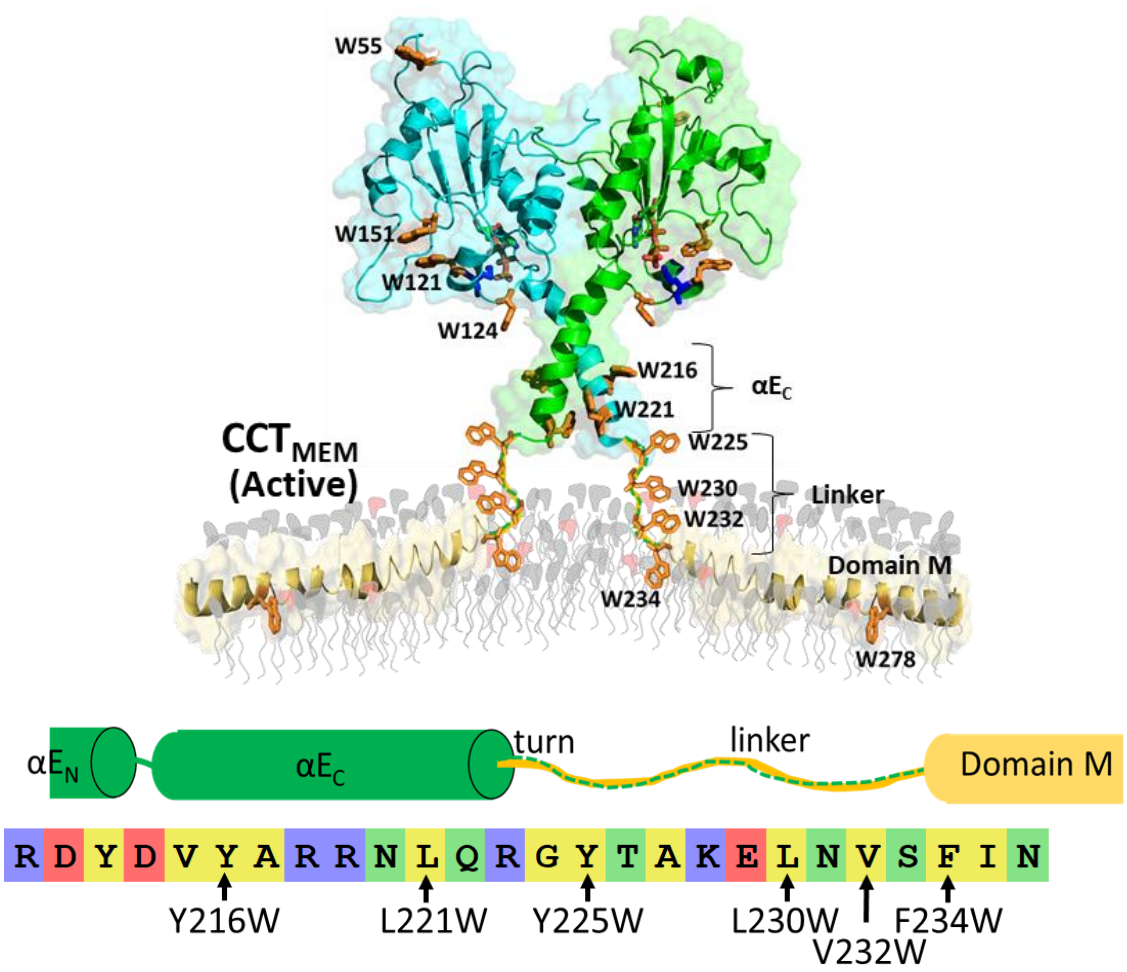

Figure 3.1. *Sites of the single-Trp mutations in a hypothetical membrane-bound CCT with 'extended' αE and unfolded linker.* A hypothetical membrane-bound CCT (CCT_{MEM}) with extended αE helices (derived from simulation files from Ramezanpour and Lee, *et al*. (69)) with the NMR-derived structure of domain M embedded in lipid (PDB: 1PEI/1PEH). Sites of single Trp mutants generated in this study are displayed in orange (W151 and W278 are the only native Trps). Also depicted is the rat CCT $αE_C$-linker sequence with sites of single-Trp mutations indicated.

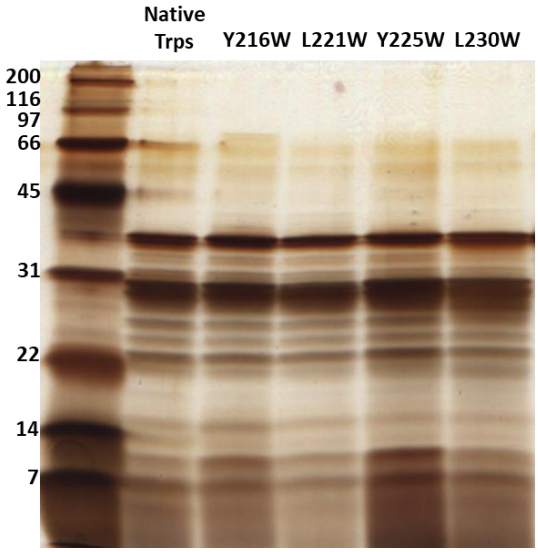

Figure 3.2. *Chymotrypsin digestion patterns are not affected by Trp mutations.* CCT312His Δ12-16 containing single-Trp mutants (Y216W, L221W, Y225W, L230W – all with W151F and W278F mutations) and containing only the native Trps (W151, W278) were digested with chymotrypsin for 3 minutes at 37°C. Digestion products were run on a 13% SDS-Page gel followed by silver staining.

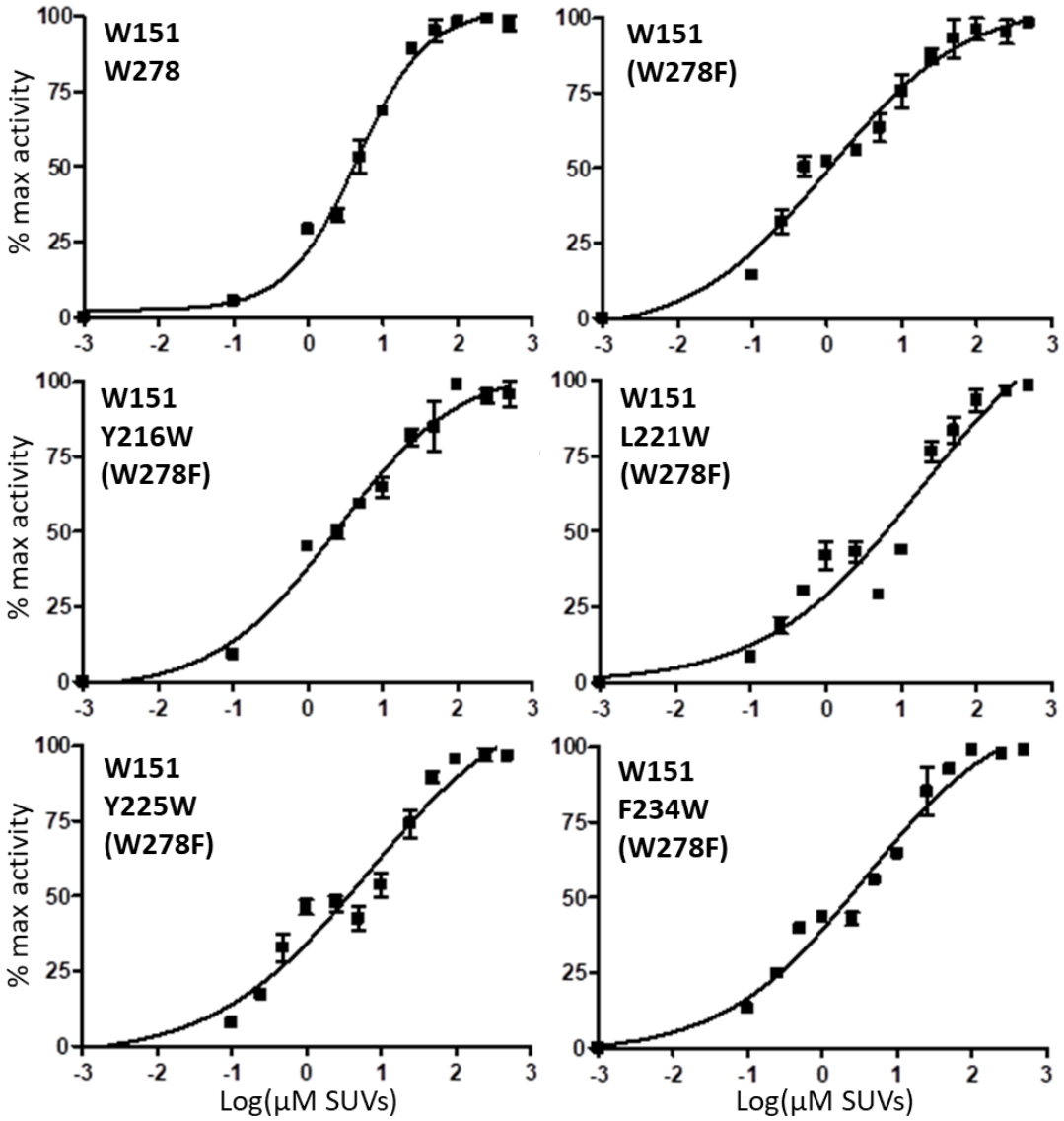

Figure 3.3. *EC_{50} is similar and low for all single Trp mutants activated by the SUVs.* Activity of single tryptophan αE/linker CCT mutants was monitored with increasing [SUVs] (50% POPC/50% eggPG) from 0 µM to 500 µM and 0.1 µg of CCT at 37°C. All constructs contained the native Trp W151. To reflect constructs used in fluorescence assays, αE/linker Trp mutants contained W278F mutation. Data was fit to a sigmoidal dose-response curve. Data points are means +/- average deviation of 2-4 independent determinations.

Table 3.1. *Melting temperatures of inactive αE and linker mutants are well above activity assay temperature.* Thermal denaturation curves of 5 μM CCT312 αE/linker mutants were generated as described in Section 2.9, and the midpoint of the SYPRO Orange transition and/or first derivative of the transition was used to obtain T_m values.

Full name of mutant	Code name	T_m
CCT312His Δ12-16	Native CCT312	55°C
CCT312His Δ12-16 (W151F)	W151F	~54C
CCT312His Δ12-16 (W278F)	W278F	50°C
CCT312His Δ12-16 L230W (W151F, W278F)	L230W	49.5°C
CCT312His Δ12-16 V232W (W151F, W278F)	V232W	50°C
CCT312His Δ12-16 L230A V232A F234A (Y225W, W151F, W278F)	Triple-A	51°C
CCT312His Δ12-16 R219Q R223Q K228Q (Y225W, W151F, W278F)	Triple-Q	51°C
CCT312His Δ12-16 Y216A Y225A F234A (L221W, W151F, W278F)	Triple-Aro	49°C
CCT312His Δ12-16 Δ227-232 (W151F)	D227-232	56°C
CCT312His Δ12-16 227GGGSGG232 (W151F)	GS linker	57°C

3.1.2. Br-PC quenching of single-Trp mutants

Quenching by BrPC requires molecular contact (overlapping van der Waals radii) of the excited Trp and bromine on the acyl chain (73). I tested quenching by BrPCs brominated at the 6,7-, 9,10-, or 11,12- positions of the acyl chain. A Trp in domain M, W278, was used as a positive control. Previous work with domain M peptides had shown strong quenching of this Trp by all three BrPCs, with the strongest quenching by 9,10-BrPC (23). In keeping with these published data, W278 was strongly quenched by all three depths of bromine quenchers in the context of CCT-312, with the strongest impact using 9,10-BrPC (**Fig. 3.4**). These data supports a stable interaction between the vesicles and domain M. In contrast, W55 at the N-terminal of the catalytic domain was not significantly quenched by any BrPC vesicles. W151 near the active site was also not quenched. These results provide evidence that BrPC quenching monitors the persistence of residue-membrane interactions and that random collision by vesicles do not contribute significantly to quenching.

The sequence conservation of the αE_C and linker sequences along with their location as the physical conduit between domain M and the active site suggest the two act cooperatively to transduce membrane-binding signals, and may be positioned close to the membrane itself. Trps at the N-terminal (W225), middle (W230), and C-terminal (W234) of CCT's linker were moderately quenched by BrPC, most prominently at the shallower 6,7 and 9,10 positions (**Fig. 3.4**). Interestingly, W216 and W221 were weakly

quenched, despite their location in the αE_C. Even more surprisingly, W124 in loop L2 was quenched beyond background levels. These data support a model of active CCT that includes the linker lying superficially at the membrane with hydrophobic residues in the αE_C and loop L2 approaching the membrane with transient interactions.

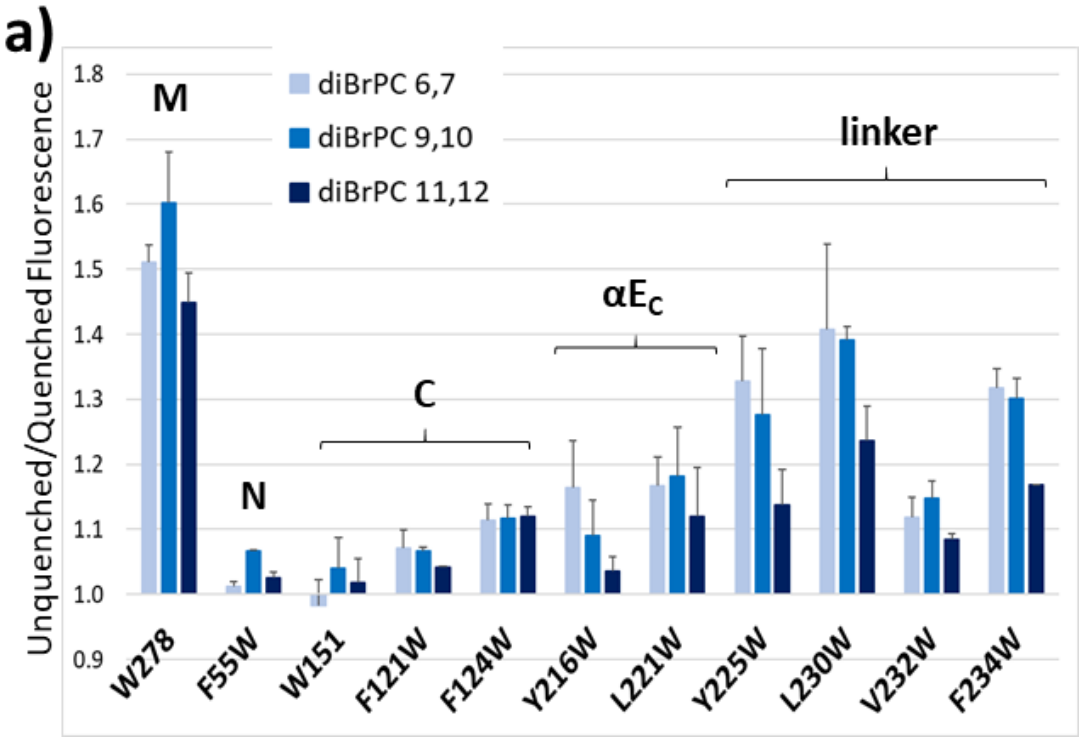
a)
Unquenched/Quenched Fluorescence
1.8
1.7
1.6
1.5
1.4
1.3
1.2
1.1
1.0
0.9
diBrPC 6,7
diBrPC 9,10
diBrPC 11,12
M
N
C
αE_C
linker
W278
F55W
W151
F121W
F124W
Y216W
L221W
Y225W
L230W
V232W
F234W

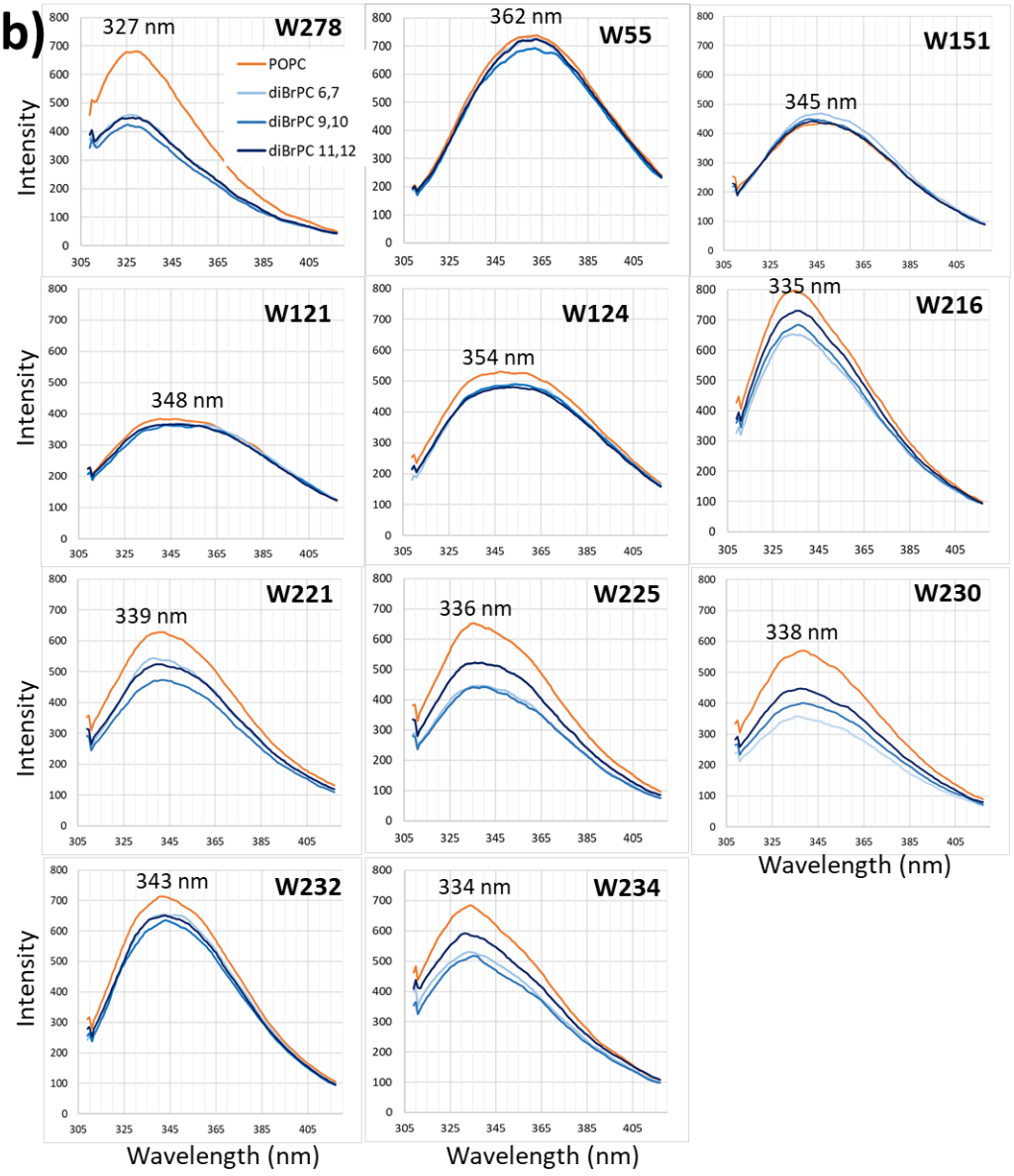

Figure 3.4. *αE$_C$ and linker residues interact with membranes superficially.* The fluorescence of samples of CCT-312 with single Trps at the indicated positions was monitored in the presence of vesicles composed of POPC/egg PG (1/1) (unquenched) or dibrominated PC/egg PG (1/1) (quenched). The [CCT] was 3 μM and the [lipid] was 450 μM. **a)** Mean degree of quenching +/- average deviation of 2-5 independent determinations. Domain location of each Trp mutation is labeled as C (catalytic), N (N-terminal), M (domain M), αE$_C$, and linker. **b)** Representative emission spectra for each single-Trp mutant. Each spectrum has lipid blanks subtracted. The average peak emission wavelength for each set of spectra is also displayed. P-values between different Trp sites are listed in **Appendix F**.

3.1.3. Acrylamide quenching of single-Trp mutants

I monitored quenching of single-Trp mutants by the aqueous-phase quencher acrylamide to probe changes in the solvent exposure of specific sites upon CCT membrane binding (**Fig. 3.5**). For comparison, the quenching constant (K_{SV}) for free tryptophan amino acid at the same concentration used for CCT Trps was 25 (**Fig. 3.5**), and the K_{SV} for the membrane-embedded W278 was 5 (in rough agreement with published work of membrane-embedded peptides (85-87)). In the absence of vesicles, the Trp sites showed a range of acrylamide quenching that likely reflects the degree to which they bury in the protein (**Fig. 3.5**). For example, the moderate acrylamide quenching of W278 in soluble CCT reflects its burial in the 4-helix complex, and the stronger quenching of W124 reflects its contact with residues of the AI helix in CCT's soluble form (60,69). All sites showed reduced acrylamide quenching in membrane-bound CCT, with the exception of W230. The reduction for K_{SV} at residues 55,121,221, and 225 is ~ 30%, which may reflect reduced "activity" of the acrylamide in the zone immediately adjacent to a membrane surface crowded with bound CCT, where both the protein-bound Trps and the acrylamide may experience reduced tumbling rate (88). Membrane protection was strong for W234 (K_{SV} = 5), suggesting that W234 marks the N-terminus of domain M. Protection was minimal for residues in the linker, in agreement with a superficial membrane localization. In soluble CCT, the AI helices should partially protect the αEc residues from solvent, thus one might anticipate an increase in acrylamide quenching upon membrane binding. However, acrylamide quenching was decreased.

W216 in αE_C showed an unexpectedly high degree of solvent-protection (3-fold) upon vesicle addition, even greater than W278. Given the low quenching by BrPC at this position, membrane binding cannot account for this result. Additional support for Y216 burial upon domain M membrane binding is the large increase in fluorescence intensity of W216 when vesicles are added to the CCT (**Fig. 3.6**), reflecting an increased quantum yield characteristic of Trp burial in hydrophobic environments. This increase is not observed in any other single-Trp mutant (**Appendix G**). Interestingly, W151 and F124 in the active site also experienced >30% solvent protection with vesicles, despite little or no quenching of this residue by the brominated PC. This may reflect reduced solvent access to the active site upon membrane binding. Taken together, the BrPC and acrylamide quenching results suggest the linker in active CCT lies near the membrane

interface, still exposed to solvent. The αE_C occupies a space slightly further from the membrane and assumes a conformation that buries Y216 into the protein interior.

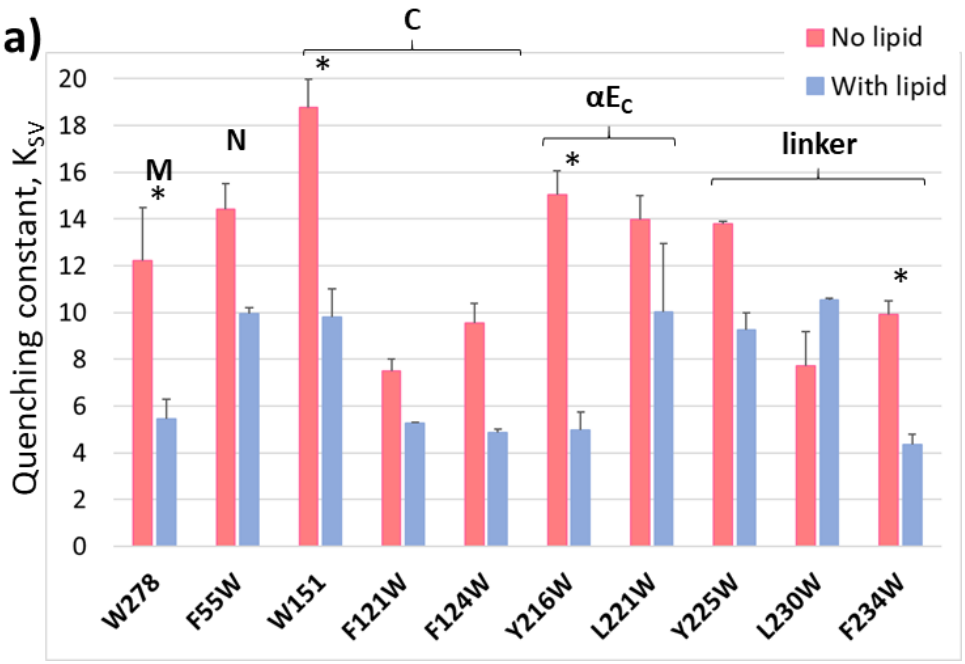
a)
C
No lipid
With lipid
αE_C
linker
M
N
*
Quenching constant, K_SV
20
18
16
14
12
10
8
6
4
2
0
W278
F55W
W151
F121W
F124W
Y216W
L221W
Y225W
L230W
F234W

b)

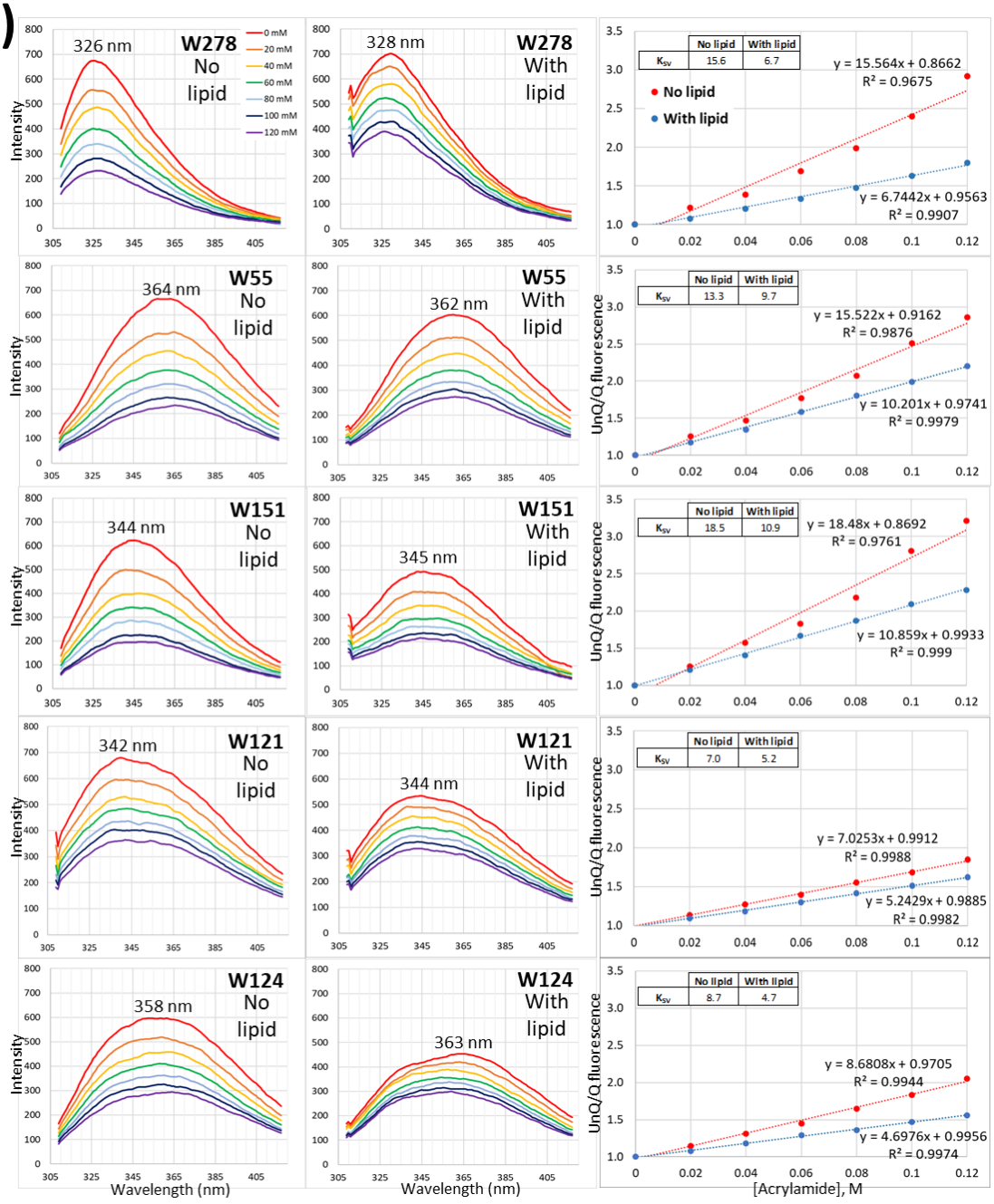
326 nm
W278 No lipid
328 nm
W278 With lipid
0 mM
20 mM
40 mM
60 mM
80 mM
100 mM
120 mM
No lipid
With lipid
Ksv
15.6
6.7
y = 15.564x + 0.8662
R² = 0.9675
y = 6.7442x + 0.9563
R² = 0.9907
364 nm
W55 No lipid
362 nm
W55 With lipid
13.3
9.7
y = 15.522x + 0.9162
R² = 0.9876
y = 10.201x + 0.9741
R² = 0.9979
344 nm
W151 No lipid
345 nm
W151 With lipid
18.5
10.9
y = 18.48x + 0.8692
R² = 0.9761
y = 10.859x + 0.9933
R² = 0.999
342 nm
W121 No lipid
344 nm
W121 With lipid
7.0
5.2
y = 7.0253x + 0.9912
R² = 0.9988
y = 5.2429x + 0.9885
R² = 0.9982
358 nm
W124 No lipid
363 nm
W124 With lipid
8.7
4.7
y = 8.6808x + 0.9705
R² = 0.9944
y = 4.6976x + 0.9956
R² = 0.9974
Intensity
UnQ/Q fluorescence
Wavelength (nm)
[Acrylamide], M

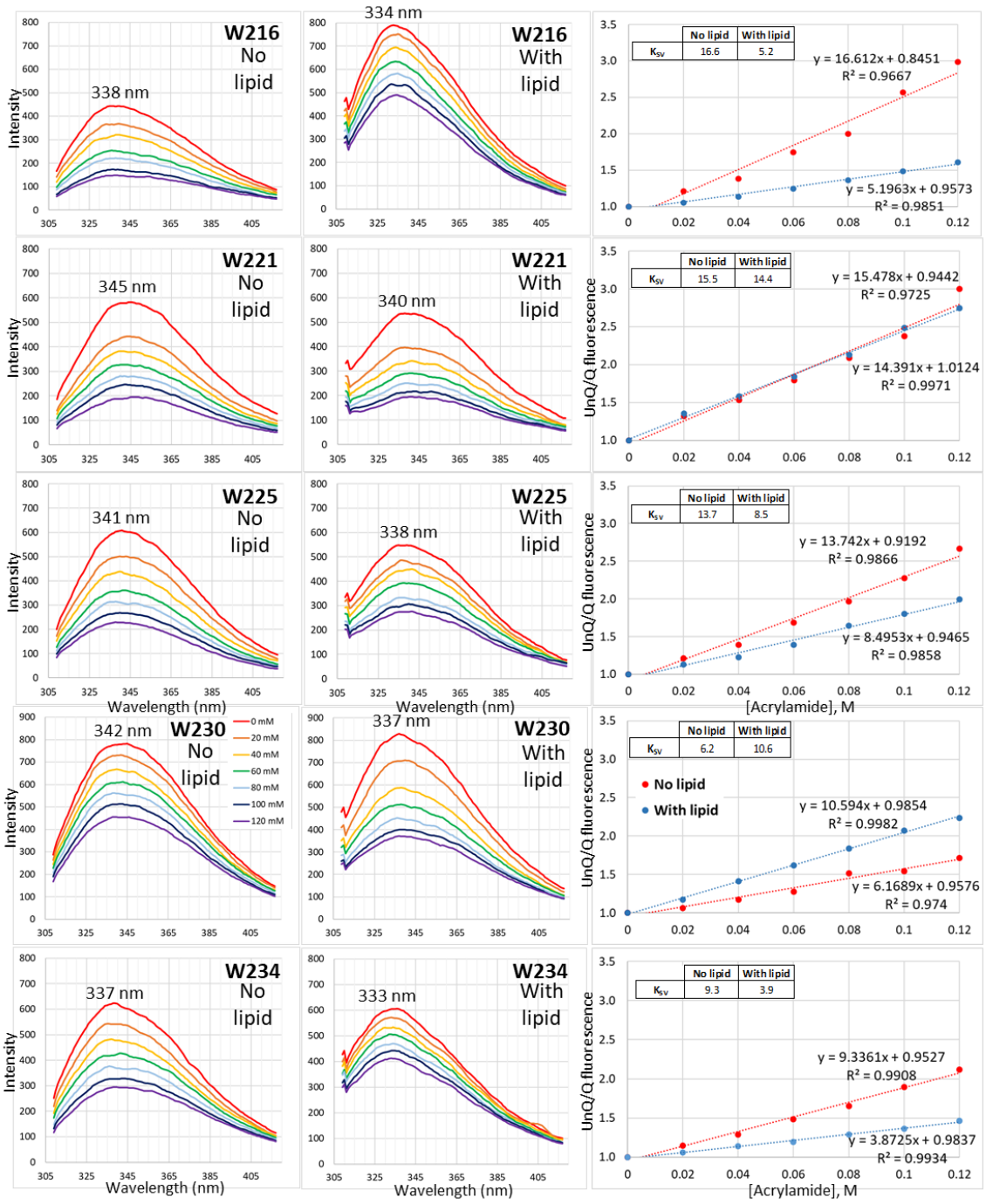
W216 No lipid
338 nm
W216 With lipid
334 nm
No lipid | With lipid
Ksv 16.6 | 5.2
y = 16.612x + 0.8451
R² = 0.9667
y = 5.1963x + 0.9573
R² = 0.9851
W221 No lipid
345 nm
W221 With lipid
340 nm
Ksv 15.5 | 14.4
y = 15.478x + 0.9442
R² = 0.9725
y = 14.391x + 1.0124
R² = 0.9971
W225 No lipid
341 nm
W225 With lipid
338 nm
Ksv 13.7 | 8.5
y = 13.742x + 0.9192
R² = 0.9866
y = 8.4953x + 0.9465
R² = 0.9858
W230 No lipid
342 nm
0 mM
20 mM
40 mM
60 mM
80 mM
100 mM
120 mM
W230 With lipid
337 nm
Ksv 6.2 | 10.6
No lipid
With lipid
y = 10.594x + 0.9854
R² = 0.9982
y = 6.1689x + 0.9576
R² = 0.974
W234 No lipid
337 nm
W234 With lipid
333 nm
Ksv 9.3 | 3.9
y = 9.3361x + 0.9527
R² = 0.9908
y = 3.8725x + 0.9837
R² = 0.9934
Intensity
Wavelength (nm)
UnQ/Q fluorescence
[Acrylamide], M

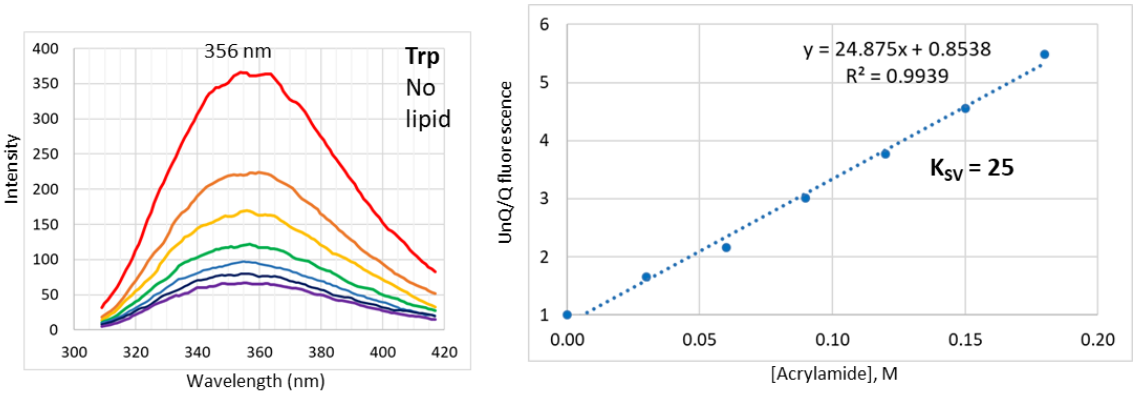

Figure 3.5. *αE$_C$ and linker residues show varied degrees of solvent protection upon membrane-binding of domain M.* The fluorescence of samples of CCT-312 with single Trps at the indicated positions were monitored in the presence and absence of POPC/egg PG (1/1) vesicles with increasing concentrations of soluble quencher (acrylamide) to generate quenching constants (K_{SV}). The [CCT] was 3 μM and the [lipid] was 450 μM. **a)** Mean quenching constants (K_{SV}) +/- average deviation of 2-3 independent determinations. Domain location of each Trp mutation is labeled as C (catalytic), N (N-terminal), M (domain M), αE$_C$, and linker. * indicates $p < 0.05$ based on a two-sample unequal variance Student's t-Test with a two-tailed distribution. **b)** Representative emission spectra for each single-Trp mutant with increasing concentrations of acrylamide is reflected in the color spectrum. Each curve has lipid/buffer blank subtracted. The average peak emission wavelength for each set of spectra is also displayed. Stern-Volmer plots are displayed to the right of the spectra. The quenching constant (K_{SV}) is the slope of the plot. Spectra and a Stern-Volmer plot for Trp amino acid in the absence of lipids is also displayed.

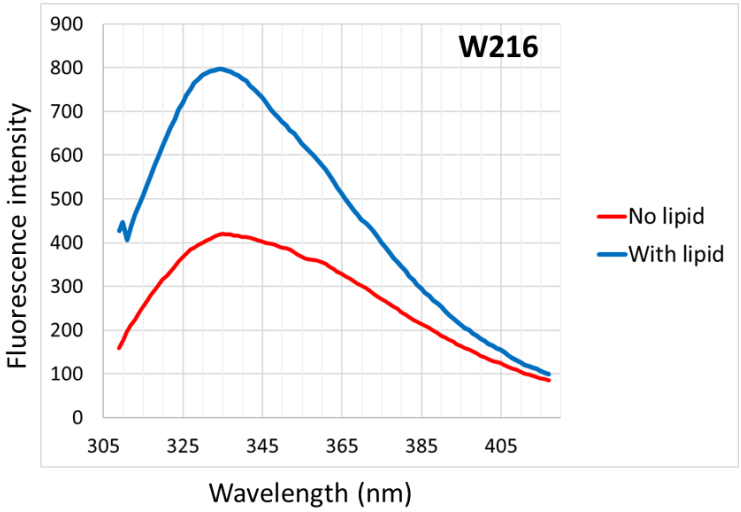

Figure 3.6. *W216 is highly protected from solvent upon membrane binding of domain M.* Fluorescence emission scans of W216 in αE (3 μM of CCT312His Δ12-16 Y216W (W151F, W278F)) in the absence and presence of 450 μM of 50% POPC/50% eggPG SUVs by excitation with 295 nm light.

3.2. The linker segment is required for CCT activity

To determine if the linker sequence is vital for CCT activation, Chanajai Tishyadhigama first generated two drastic mutants. One mutant deleted a significant region of the linker (Δ227-232) and the other replaced this region with a non-specific flexible sequence ^{227}GGGSGG^{232}. Neither of these mutants were activated by lipids (**Fig. 3.7**), suggesting the native CCT linker sequence is important for transducing the lipid-induced activating signal. Global stability was not impaired by these mutations (**Table 3.1**) and domain M-membrane interactions were the same as wild-type linker constructs (monitored by BrPC quenching of W278 - data not shown).

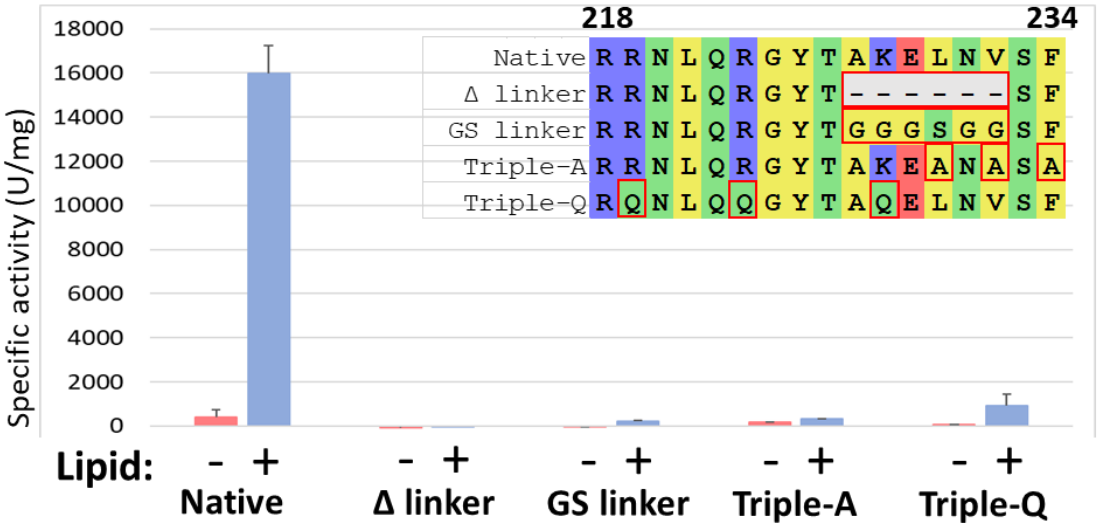

Figure 3.7. *The αE$_C$-linker sequence is sensitive to mutation.* The enzyme activity of CCT linker mutants: Δlinker (Δ227-232), GS linker (^{227}GGGSGG^{232}), Triple-A (L230A, V232A, F234A), Triple-Q (R219Q, R223Q, K228Q) was measured as nmol CDP-choline produced per min per mg CCT. Sites of mutation are highlighted in red boxes. Each mutant was assayed in the absence and presence of 200μM vesicles (50% eggPG, 50% POPC). Data are means +/- deviation of 2 independent determinations.

The enzyme activity of each single-Trp CCT mutant was monitored in the absence and presence of activating lipid vesicles (after restoring the native W151 in the active sites) (**Fig. 3.8**). The less-conservative mutations had severe effects on lipid-dependent activity. The activity of L221W in the αE was decreased ~75%, while the activities of L230W and V232W were nearly abolished. In these cases, the activities were affected both in the absence and presence of vesicles. The T_m values for these

constructs were unaffected, suggesting they remain folded at the activity assay temperature of 37°C (**Table 3.1**). These mutations illustrate the finely-tuned nature of the linker sequence and its high sensitivity to mutation. The more conservative Trp mutations (from tyrosine and phenylalanine) did not have a substantial effect on the activity of CCT.

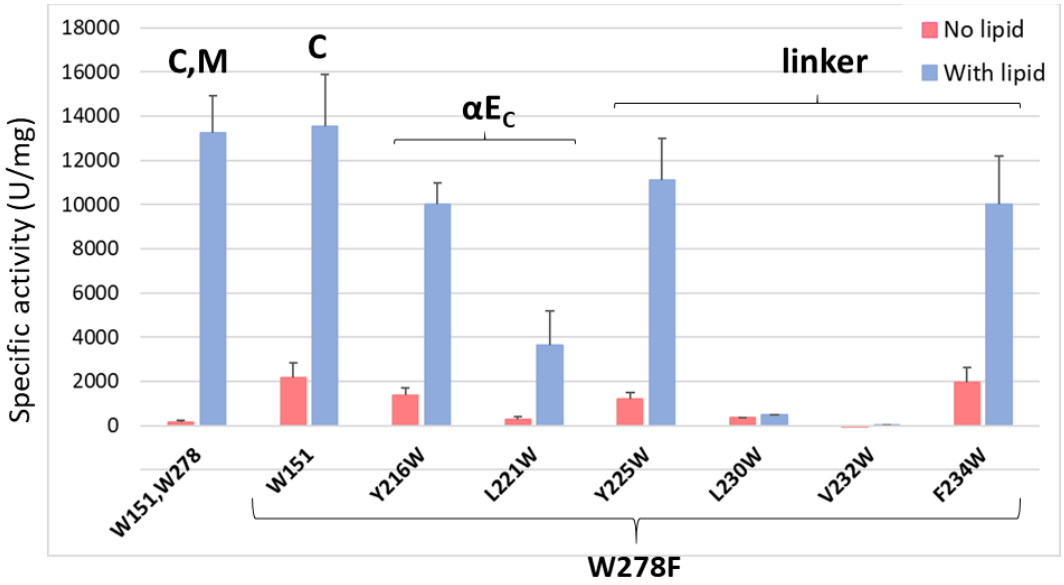

Figure 3.8. *Enzyme activity analysis of single tryptophan mutations in αE_C and linker show that non-conservative substitution are not tolerated.* W151,W278 is a construct with no engineered Trp mutations and contains both intrinsic Trps at positions 151 and 278. W151 represents intrinsic Trp at W151 but with W278F mutation. All linker/αE mutants in this analysis contain W151 and have W278F mutation. Activity was measured as nmol CDP-choline produced per min per mg CCT. Activity was measured in the absence or presence of 50% POPC/50% eggPG vesicles at 200μM. Data are means +/-deviation of 2 independent determinations. Domain location corresponding to the indicated Trps is labeled as C (catalytic), M (domain M), αE_C, and linker.

3.3. Multiple conserved αE_C-linker residues have roles beyond membrane interaction

I next created three separate αE_C-linker mutants to perturb the membrane-linker interaction. In Triple-A, three conserved hydrophobic residues were mutated to alanine (L230A/V232A/F234A). In Triple-Q, three conserved basic residues were mutated to glutamine (R219Q/R223Q/K228Q). In Triple-Aro, three conserved aromatic residues were mutated to alanine (Y216A/Y225A/F234A). The Triple-A and Triple-Q mutants

were not activated by vesicles (**Fig. 3.7**) and previous enzyme activity analysis has shown that the Y216A mutation in the Triple-Aro mutant also prevents activation by vesicles (Taneva, *et al*., unpublished). These constructs remain folded above the activity assay temperature of 37°C (**Table 3.1**). The large effect of these mutations on both soluble and membrane-bound CCT activity clearly shows how valuable these specific amino acids are for generating a catalytically-active CCT in both the presence and absence of membranes.

I hypothesized that the strong inactivation by these linker mutations was due to perturbation of the linker-membrane interaction. To test this hypothesis, I monitored quenching of W225 fluorescence by BrPC in the context of the Triple-A and Triple-Q mutations. Neither mutating conserved hydrophobic residues (Triple-A) nor conserved basic residues (Triple-Q) prevented quenching of W225 (**Fig. 3.9**). I suspected that the Y225W mutation, along with two other conserved aromatic residues in the αE_C (Y216) and linker (F234), may be the driving force of the linker-membrane interaction due to the strong affinity of aromatic residues for membrane interfaces (89,90). I mutated these three residues to alanine (Triple-Aro) and monitored BrPC quenching of engineered W221. W225 was more highly quenched by BrPC than W221 (**Fig. 3.4**), thus I anticipated a reduced contribution of the introduced Trp to the linker-membrane interaction. However, Triple-Aro maintained a linker-membrane interaction as measured by W221 quenching (**Fig. 3.9**). One explanation for these seemingly perplexing data is that multiple residues within the αE_C-linker sequence act together to position the linker near the membrane interface. At the same time, key conserved residues in the linker sequence clearly have an alternate function: I propose that the function is to forge interactions with other regions of CCT, and a strong candidate is the αE_C, based on its linker proximity and similar importance for catalysis (Taneva, Lee, *et al*. unpublished data).

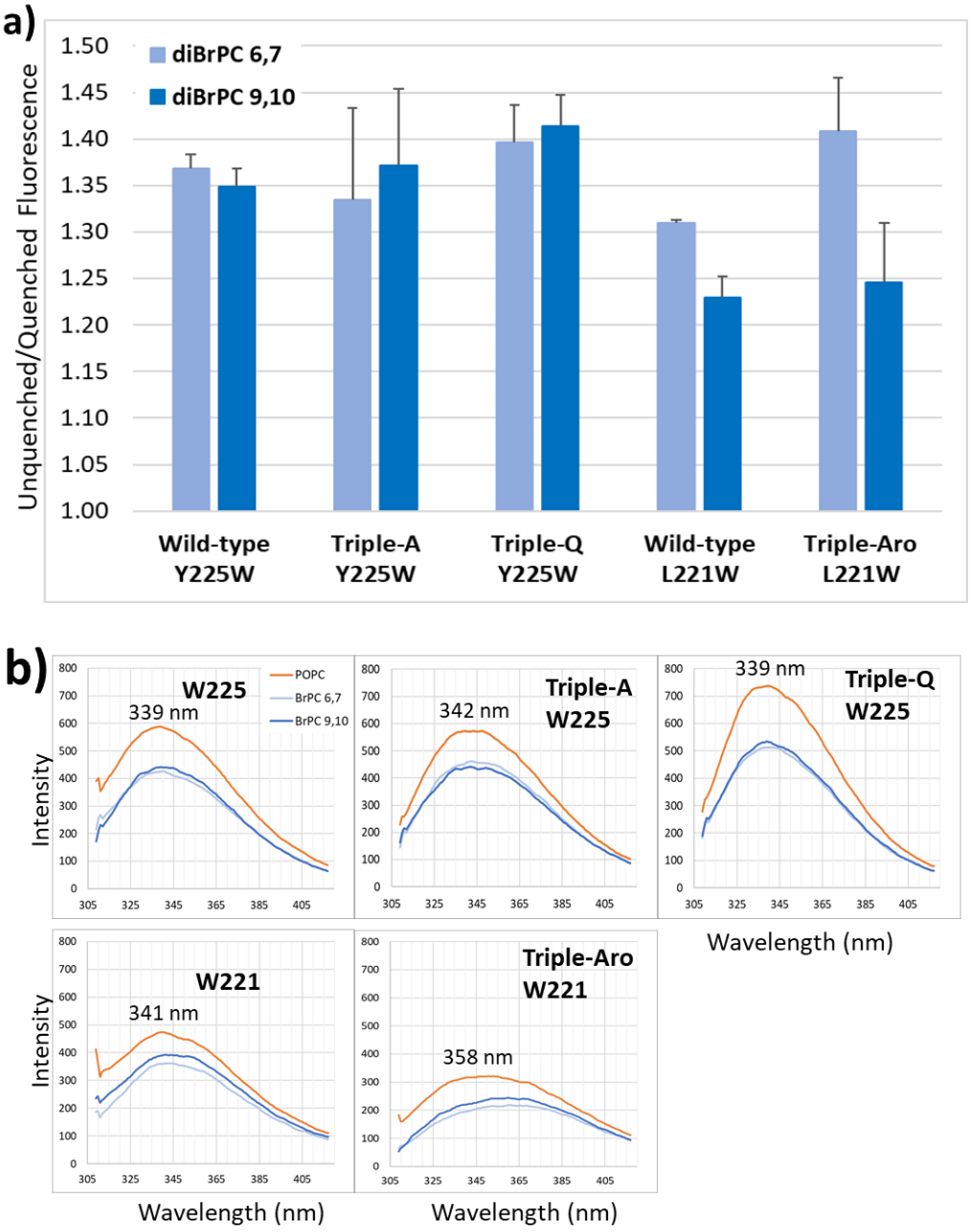

Figure 3.9. *Mutation of conserved hydrophobic, basic, or aromatic residues in the αE$_C$-linker sequence does not perturb the linker-membrane interaction.* CCT constructs with wild-type, Triple-A (L230A, V232A, F234A), or Triple-Q (R219Q, R223Q, K228Q) linkers in the context of a Y225W mutation and CCT constructs with wild-type or Triple-Aro (Y216A, Y225A, F234A) linkers were subjected to Trp quenching by 450 μM of 50% diBrPC (6,7 or 9,10)/50% eggPG vesicles. **a)** Mean degree of quenching +/- deviation of 2 independent determinations. **b)** Representative emission spectra for each linker mutant. Each spectrum has lipid blanks subtracted. The average peak emission wavelength for each set of spectra is also displayed.

3.4. The αE-linker sequence contributes to an independent membrane-binding and CCT-activating domain

3.4.1. BrPC quenching of CCT-236 implicates the αE_C – linker sequence as a membrane-binding region

The observation of a linker-membrane interaction in CCT-312 could be interpreted as simply a consequence of its proximity to membrane-bound domain M. To test whether the linker segment has intrinsic membrane partitioning properties I examined the ability of the linker to interact with vesicles using CCT-236. CCT-236, truncated before domain M, is constitutively active in the soluble form with a 10-fold increase in activity due to the absence of auto-inhibitory contacts (55,68) (**Fig. 3.10**). CCT-236 is activated by lipids ~ 2-fold, compared to a > 30-fold activation of the domain M containing construct, CCT-312 (**Fig. 3.10**). To determine if the linker acts as an independent activating domain, I removed a region of the linker (Δ227-232) in the context of CCT-236 and monitored enzyme activity. This mutation decreased the activity of CCT-236 both in the absence and presence of lipids, but the mutant was still activated > 2-fold by lipids (**Fig. 3.10**). Furthermore, when I engineered W225 into CCT-236 and monitored quenching by BrPC vesicles, I found that quenching was very strong, more intense than quenching of W225 in the context of CCT312. (**Fig. 3.11**). This implies that the linker region is an independent membrane-binding domain. Surprisingly, however, quenching of W225 in CCT-236 was not reduced by deletion of linker residues 227-232, but was enhanced. Possible reasons are suggested in Chapter 4. This suggests that the linker region is not required for association of CCT-236 with membranes, but that membrane association requires additional residues to stabilize the interaction, likely αE_C residues.

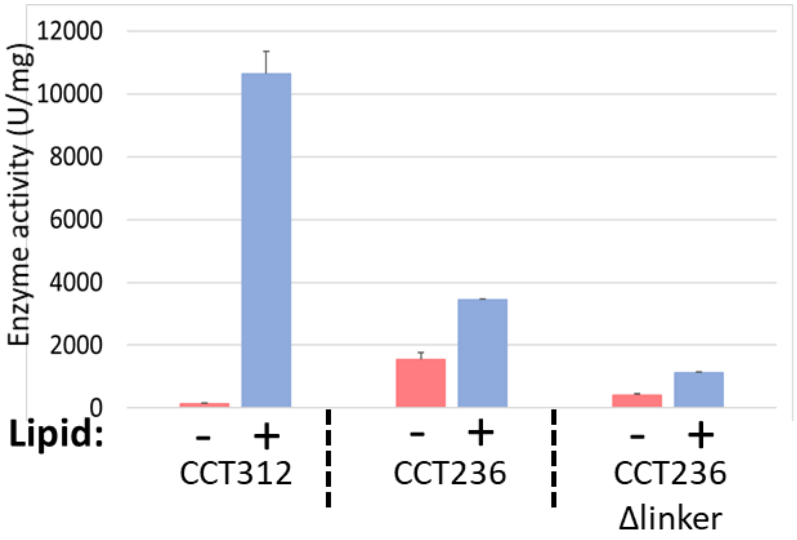

Figure 3.10. *Activation of CCT-236 by lipids is not solely mediated by the linker.* Enzyme activity was compared for CCT312 (with catalytic and M domains), CCT236 (domain M removed), and CCT236 Δlinker (Δ227-232). Each mutant was assayed in the absence and presence of 200 μM vesicles (50% eggPG, 50% POPC). Data are means +/- deviation of 2 independent determinations.

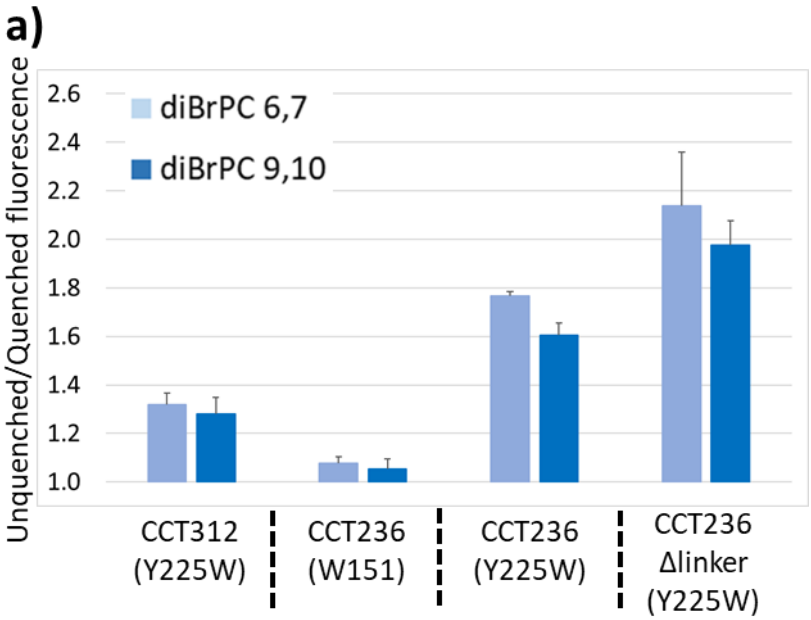

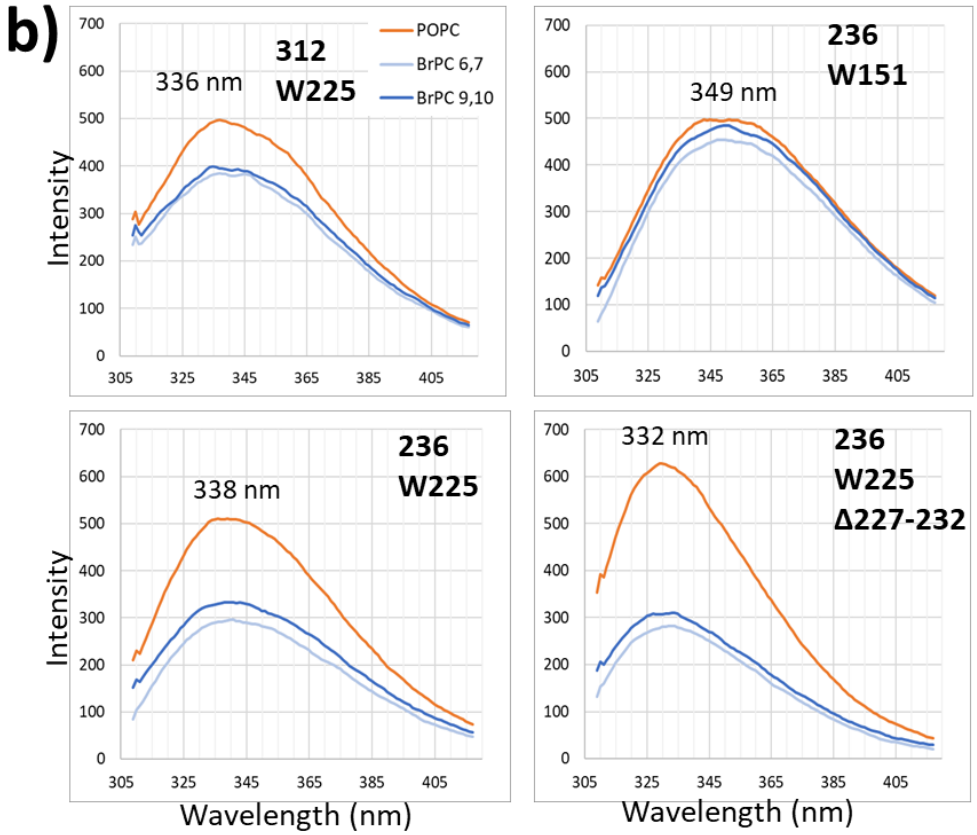

Figure 3.11. *CCT-236 maintains an interaction with the membrane in the absence of the native linker sequence.* CCT312 (Y225W), CCT236 (W151), CCT236 (Y225W), and CCT236 Δlinker (Δ227-232, Y225W) were subjected to Trp quenching by 450 μM of 50% diBrPC (6,7 or 9,10)/50% eggPG vesicles to monitor the linker-membrane interaction. **a)** Mean degree of quenching +/- deviation of 2 independent determinations. **b)** Representative emission spectra for each linker mutant (with 50% eggPG/50% PC SUVs). Each spectrum has lipid blanks subtracted. The average peak emission wavelength for each set of spectra is also displayed.

3.4.2. FPLC gel filtration of CCT-236 confirms an αE_C – linker association with lipid

If a linker deletion does not prevent membrane-association of CCT-236, is the αE_C a membrane-binding determinant? Deletion of the entire CCT sequence beyond the αE_N (CCT-212) obliterates CCT activity with or without lipids (Taneva, *et al.*, unpublished), whereas CCT-236 Δ227-232 with the αE_C intact maintained some activity and response to lipids. This emphasizes the importance of αE_C residues in lipid-dependent activation and membrane binding. To compare the lipid interaction of CCT-236 and these two mutants, fast protein liquid chromatography (FPLC) gel filtration was

performed in the presence and absence of activating lyso-PC (LPC) lipid micelles (**Figure 3.12**). All FPLC experiments were performed by Dr. Jaeyong Lee. This method utilizes constructs with only native Trps (W151), thus the lipid interaction is not biased by engineered Trps. In the absence of lipid, CCT-236 eluted as a peak around 110 kDa (tetramer size) but upon addition of micelles, the eluted complex size increased to ~220 kDa, and co-eluted with phospholipid (**Fig. 3.12**, panel b). This reinforces the BrPC quenching data suggesting an interaction is formed between CCT-236 and lipids. Interestingly, CCT-236 Δ227-232 eluted as a ~70 kDa complex (dimer size) in the absence of lipids. With the introduction of micelles, the elution peak became broad, with a much larger size, similar to CCT-236. This suggests that the linker deletion does not abolish the CCT-236-lipid interaction. However, CCT-212, lacking all of the αE_C and linker, elutes as a 70 kDa dimer both in the absence and presence of micelles, suggesting the αE_C contributes to the CCT-236 - lipid interaction. These experiments with domain M-truncated CCTs provide evidence that a combination of the linker and αE_C sequences can form an independent, catalytically-relevant membrane interaction.

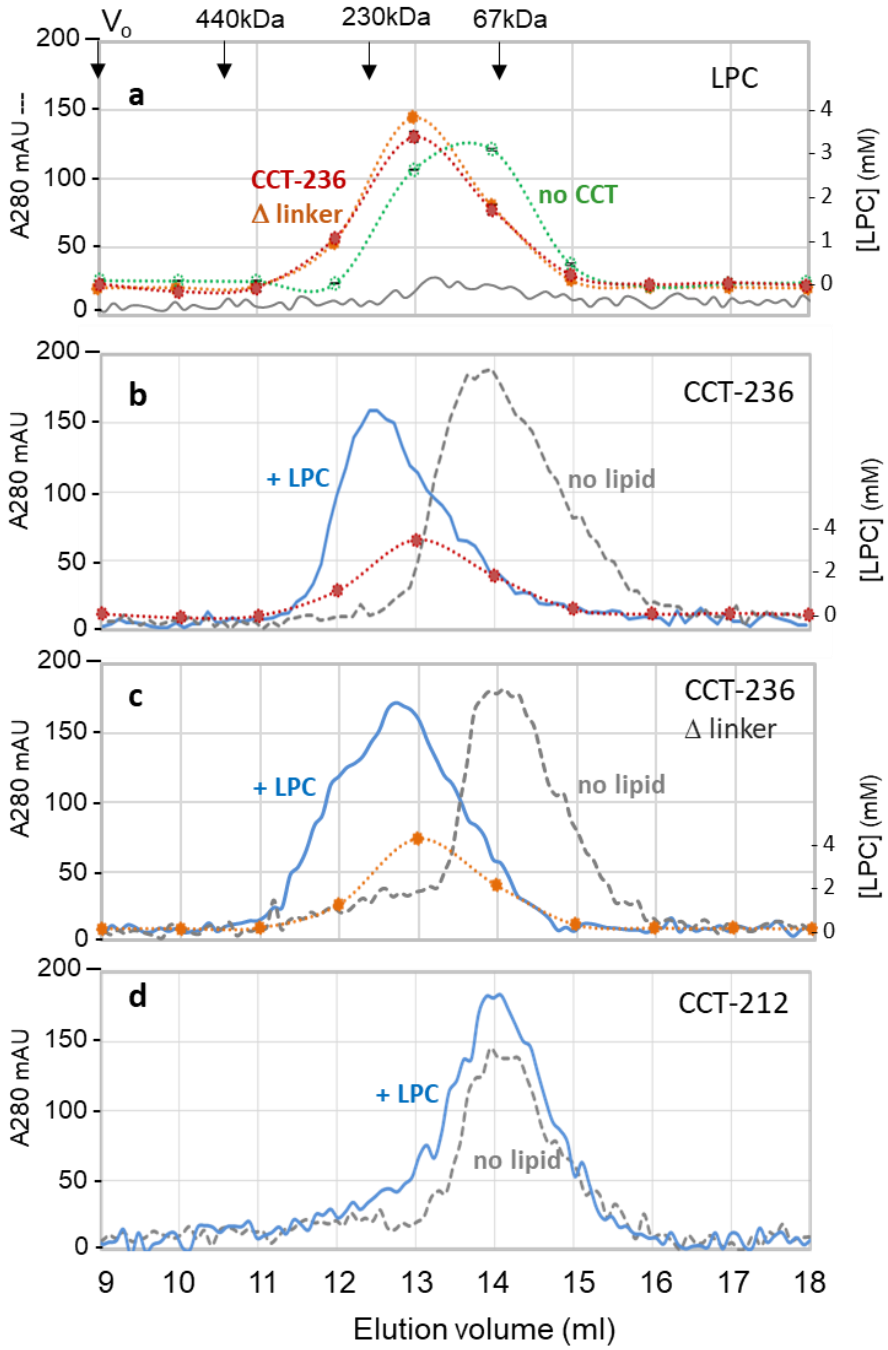

Figure 3.12. *Independent elution of CCT and LPC in FPLC gel filtration requires truncation of the linker and αE$_C$.* Figure courtesy of Dr. Jaeyong Lee. **a)** Concentration of LPC in each elution fraction (in the absence and presence of CCT-236 and CCT-236 Δ227-232) measured by the Bartlett assay (82). The absorbance at 280 nm was monitored for the pure LPC sample in panel **a** (grey line) and the indicated CCT mutant in the absence and presence of LPC in panels **a - d.** The phospholipid profile associated with the CCT236-LPC sample and the CCT-236 Δ227-232 - LPC sample is also shown in panels **b** and **c**, respectively**.** The elution fractions of the mass standards are indicated by arrows.

3.5. Trp-dansyl-PE FRET supports a linker-dependent bending of the αE helices

If the αE helices bend during the conversion from inactive to active CCT, the distance between the membrane and the catalytic domain would be reduced.

3.5.1. Analysis of Trp-dansyl-PE FRET acceptor fluorescence

To monitor the relative distances between the membrane and sites in the catalytic domain, the αE, and the linker, FRET efficiency curves were generated by monitoring fluorescence increases of vesicle-associated FRET acceptor, dansyl-PE, with increasing concentrations of CCT single-Trp mutants, constituting the FRET donor (**Fig. 3.13**). I monitored FRET at the same Trp positions used for the BrPC quenching analysis. The FRET curves are hyperbolic and saturate because as CCT was titrated into a fixed concentration of vesicles (100 μM), binding to the vesicles likely became restricted due to molecular crowding on the membrane surface. The lipid/protein ratio was only 25 at the highest donor/acceptor ratio, barely sufficient to solvate domain M (91). Despite this potential limitation, it is clear that W278 in domain M, along with W234, produced the highest FRET signals with this approach (**Fig. 3.13**). The negative control, W55, at the N-terminal of the catalytic domain, produces a very low background FRET signal (0.05). FRET efficiency values above this background will indicate a membrane surface approach of Trp closer than ~30 Å, as larger Trp-dansyl distances produce FRET efficiency values below ~0.1-0.15, given the R_0 for the Trp-dansyl pair of ~20-24 Å [9, 10] (**Appendix H**). Based on the structural data from soluble CCT, extended αE helices and an extended/solvent-exposed linker sequence (**Fig. 1.9**) would position loop L2 and the active site more than 30 Å from the active site, out of effective FRET range.

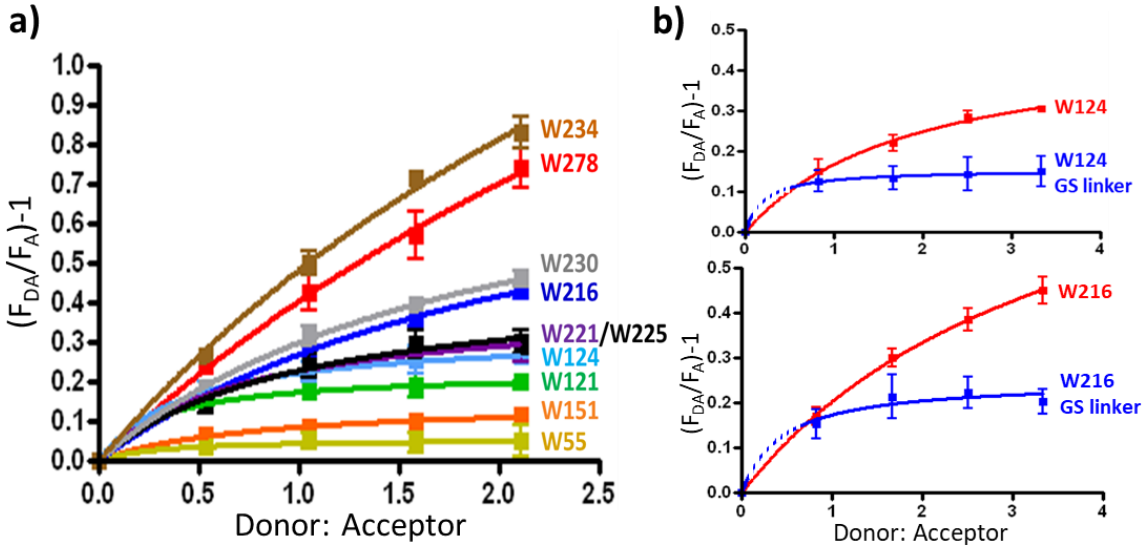
a)
b)
W234
W278
W230
W216
W221/W225
W124
W121
W151
W55
W124
W124
GS linker
W216
W216
GS linker
Donor: Acceptor
Donor: Acceptor

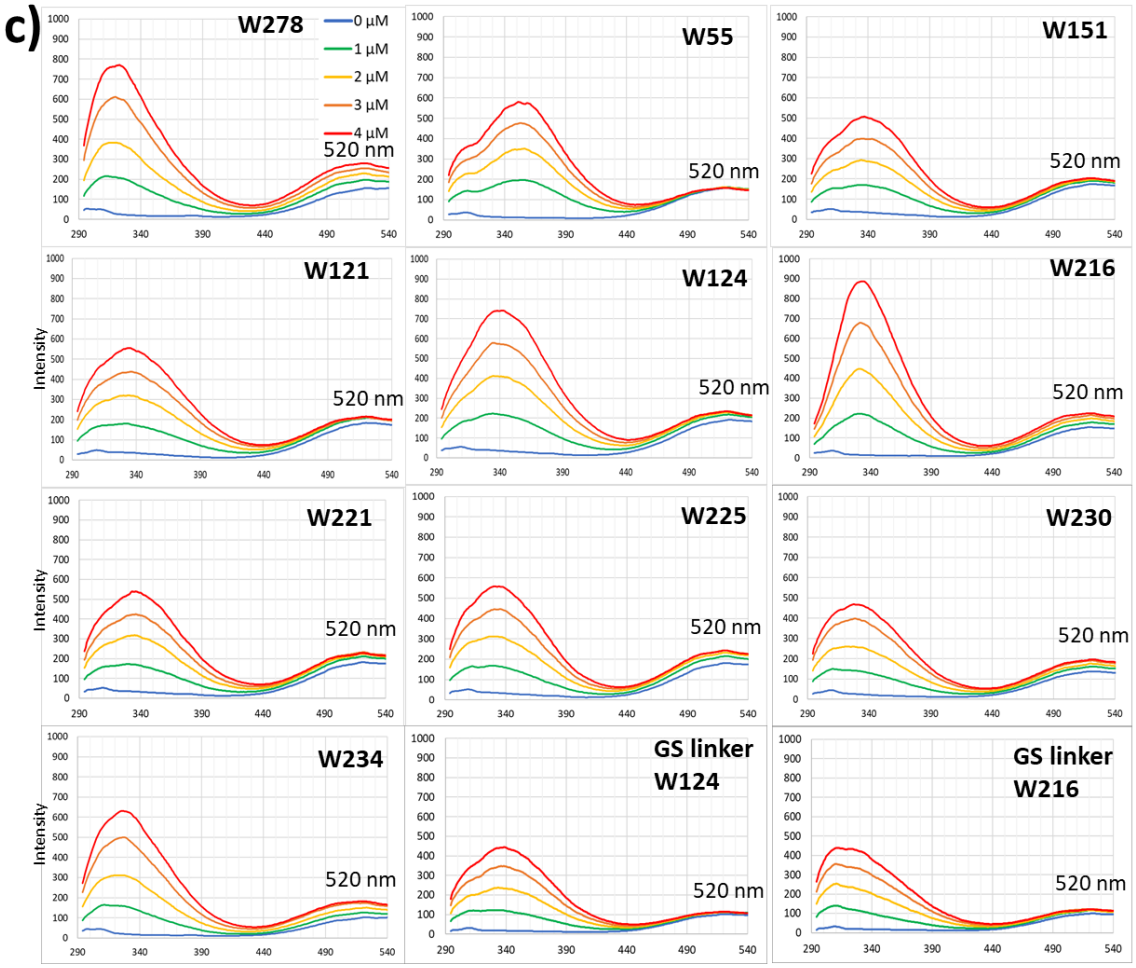

Figure 3.13. *Dansyl-PE fluorescence suggests a close membrane approach of Trps in αEc and domain C.* 0-4 µM of single-Trp CCT constructs were added to 100 µM of ~1.8% dansylPE vesicles (50% POPC, 48% eggPG) and Trp was excited. FRET efficiency was calculated using F_A (intensity at 520 nm when [CCT] = 0 µM) and F_{DA} (intensity at 520 nm with increasing [CCT]). Data are means +/- deviation of 2 independent determinations. **b)** Strong FRET between dansyl-PE and αE_C or L2 depends on the native linker. For W124 and W216, FRET was compared between constructs containing a wild-type linker and GS linker (^{227}GGGSGG^{232}). **c)** Sample emission spectra for each single-Trp mutant.

W151 near the active site and W121/W124 in loop L2 produced measurable FRET signals, suggesting an approach of these residues to the membrane interface that would not be possible with an 'extended' α-helical conformation (**Fig. 3.13**). The FRET signal produced by W124 is especially intriguing, as it is similar in strength to the signals produced by W221 in αE_C and W225 in the linker. FRET from W216 was also surprisingly high given its position in the middle of the αE_C, higher than W221 at the C-terminal of αE_C and similar to W230 of the linker. Therefore, the αE and linker

sequences appear to lie along a similar plane with respect to the membrane surface, perhaps folding into a condensed structure near the membrane during CCT activation.

To probe the bent αE-helix model and its dependence on a wild-type linker sequence, I monitored Trp-dansyl-PE FRET of W124 (loop L2) and W216 (αE) in the context of a non-specific flexible linker (^{227}GGGSGG^{232}) by monitoring dansyl fluorescence increases (**Fig. 3.13**). Compared to the wild-type linker Trp mutants, both linker mutants produced decreased FRET signals. Without native intramolecular interactions forged by the wild-type linker in active CCT, the αE may not be stabilized in a bent conformation, preventing the catalytic domain from a stable approach to the membrane surface.

An important caveat to consider when assessing Trp-dansyl FRET data is that dansyl fluorescence increases could be affected by differences in intensity and peak wavelengths which vary based on the environment of different Trp sites, differences I observed in the spectra. A benefit of the chosen sites is that most Trps emit near the dansyl absorbance maximum of 336 nm (**Table 3.2**). Also R_0 is not highly dependent on spectral overlap or donor quantum yield (73), and thus FRET efficiency values would not vary significantly among Trps based solely on small blue shifts and intensity differences. The main determinant of FRET in these experiments is the donor-acceptor distance, r.

Table 3.2. *Max emission wavelengths do not vary greatly for most Trp positions.* Wavelength maximums of Trp emission spectra in the presence of SUVs, averaged from n determinations with average deviation listed. Single Trp CCT312His Δ12-16 mutants were excited at 295 nm in the presence and absence of 450 μM of 50% eggPG/50% POPC SUVs. Domain location of single Trp is also noted.

Domain	Trp site	lipid	Λ_{max} (nm)	N
M	W278	-	326 ± 2	4
		+	328 ± 1	4
N-terminal	W55	-	362 ± 2	2
		+	362 ± 1	4
Catalytic	W151	-	345 ± 1	4
		+	346 ± 1	4
	W121	-	344 ± 2	3
		+	347 ± 4	4
	W124	-	351 ± 4	3
		+	354 ± 7	4
αE_C	W216	-	337 ±1	7
		+	334 ± 1	7
	W221	-	344 ± 2	7
		+	341 ± 1	7
linker	W225	-	342 ± 1	6
		+	337 ± 1	6
	W230	-	341 ± 1	5
		+	337 ± 1	5
	W234	-	338 ± 1	4
		+	333 ± 1	4

3.5.2. Analysis of Trp-dansyl-PE FRET donor fluorescence

To strengthen my conclusions based on dansyl-PE FRET data and maintain a constant and lower protein:lipid ratio (to prevent FRET signal saturation due to vesicle surface crowding by CCT), I monitored FRET efficiency values at select Trp sites by monitoring Trp fluorescence decreases while increasing the concentration of dansyl-PE acceptor in my lipid vesicles (**Fig. 3.14**). The lipid/protein ratio was 100 in all samples, which is 2-fold in excess of the requirement for complete solvation of domain M (91). These data illustrate a similar trend to that obtained when monitoring dansyl-PE, except W216 produced the largest FRET signal. W234 and W278 again produced a similar signal (and roughly similar to W216), confirming W234 as the start of domain M. W124 in loop L2 and W221 in the αE produced similar FRET signals when monitoring Trp fluorescence, suggesting loop L2 approaches the membrane to approximately the same extent as some residues in the αE. The glycine-rich linker substitution (^{227}GGGSGG^{232})

also reduced the FRET signal when monitoring Trp fluorescence (**Fig. 3.14**), although not to the same degree as when monitoring dansyl fluorescence. Overall, the FRET data supports substantial conformational shifts in the αE_C-linker sequence that occurs during membrane-binding, stabilizing an active catalytic domain close to the membrane surface (**Fig. 3.15**).

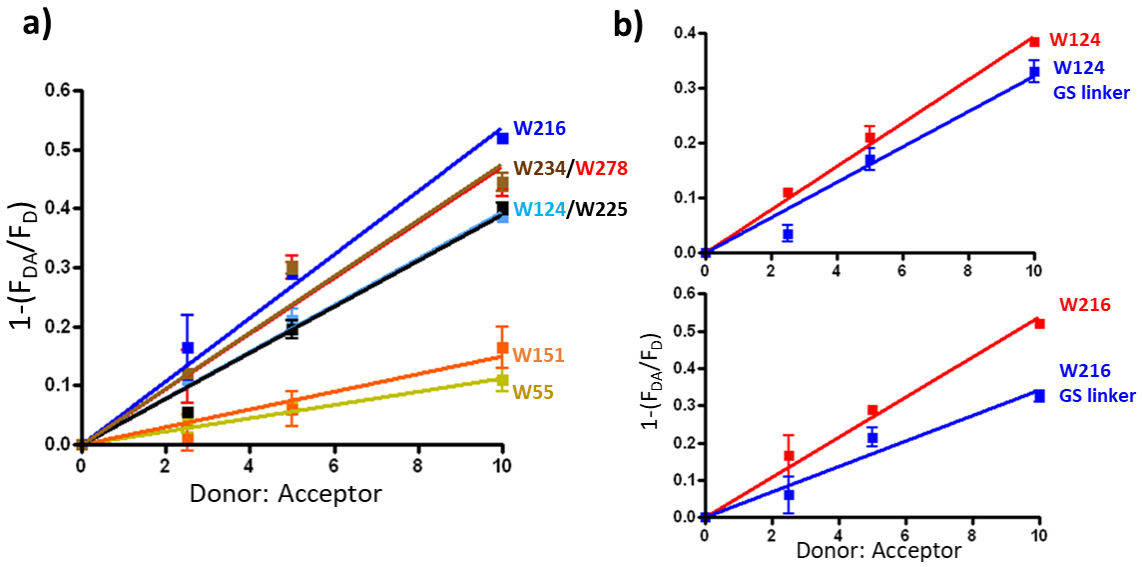

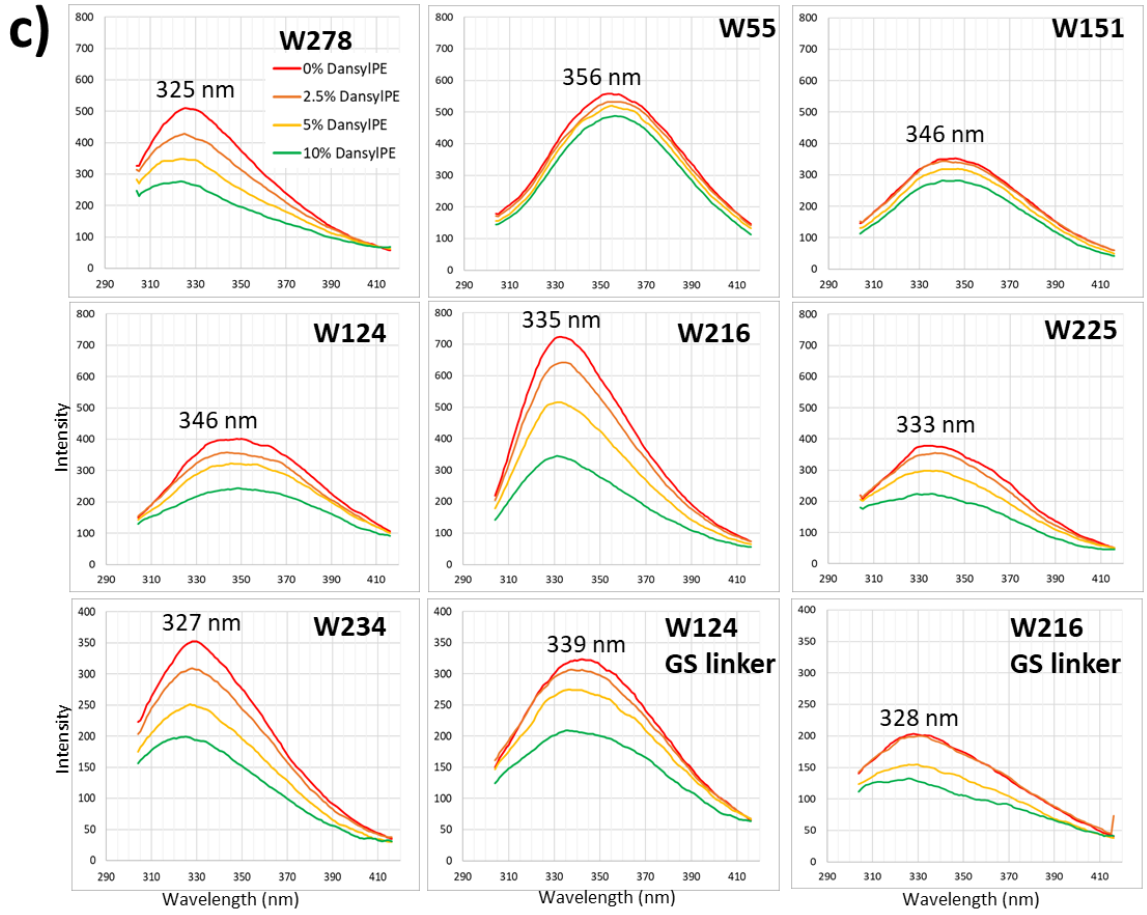

Figure 3.14. *Trp-dansyl-PE FRET supports a bent αE helices model.* 1 uM of single-Trp CCT constructs were added to 100 μM vesicles containing the indicated mole percent dansylPE balanced by eggPG in 50% POPC. **a)** FRET efficiency was calculated using F_D (intensity of Trp without dansyl) and F_{DA} (intensity of Trp with dansyl). Data are means +/- deviation of 2 independent determinations. For W124 and W216, FRET was compared between constructs containing a wild-type linker and GS linker (^{227}GGGSGG^{232}). **b)** Strong FRET between dansyl-PE and αE_C or L2 depends on the native linker. For W124 and W216, FRET was compared between constructs containing a wild-type linker and GS linker (^{227}GGGSGG^{232}). **c)** Sample emission spectra for each single-Trp mutant used in FRET. Each spectrum has lipid blanks subtracted.

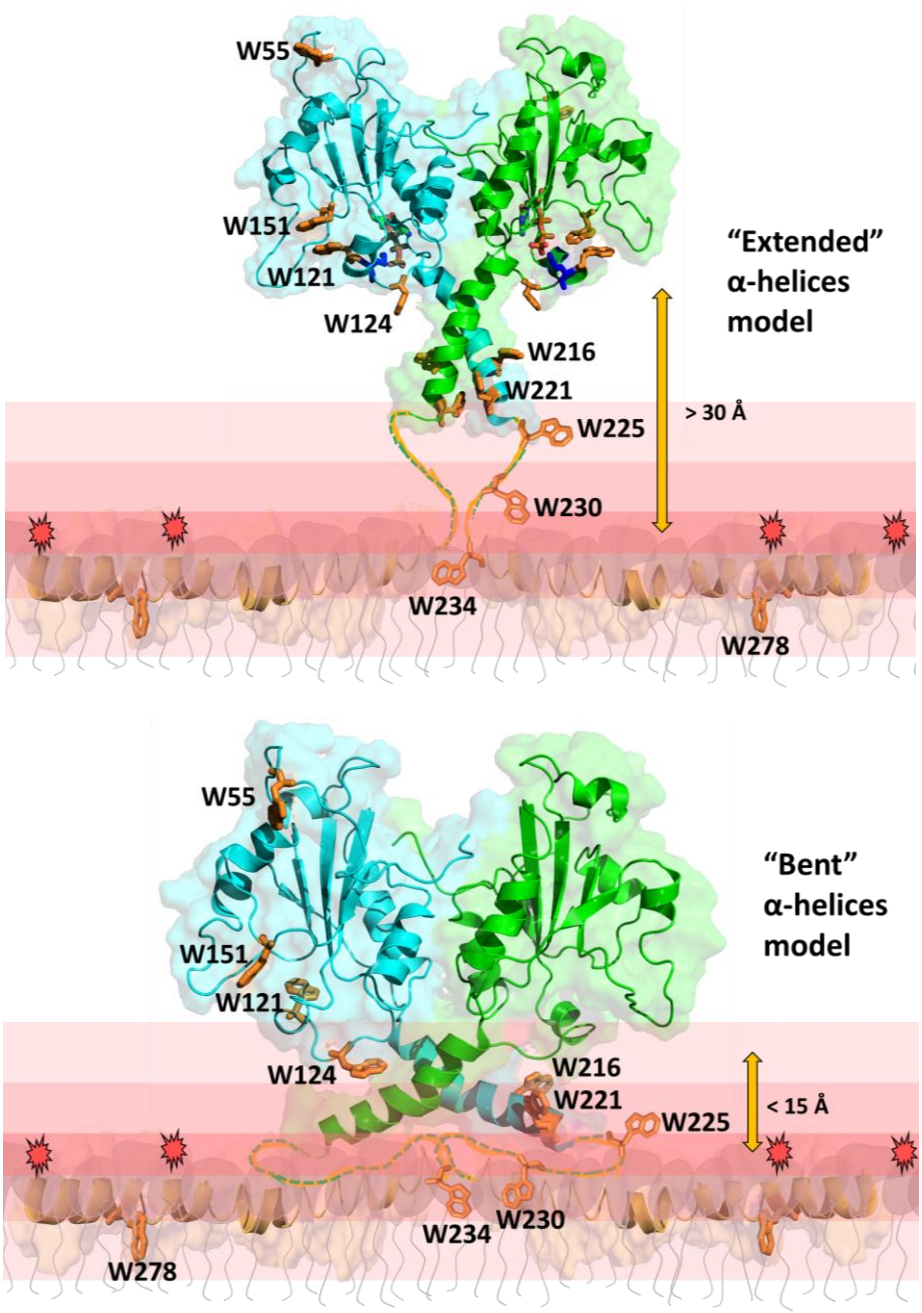

Figure 3.15. *The linker may stabilize an active, bent conformation of the αE helices.* Top panel illustrates the estimated distances between engineered Trps and membrane surface- localized dansyl-PE when the αE_C and linker are fully extended. The shades of red reflect the diminishing FRET range for the Trp-dansyl pair. The lower panel illustrates the transition of W124, W216, and W221 into FRET range when the αE is bent at the hinge and the linker lies parallel to the membrane. The CCT structures depicted are derived from simulation files from Ramezanpour and Lee, *et al*. (69). The NMR structure of domain M embedded in lipid is from PDB: 1PEI/1PEH. W225, W230, and W234 were manually placed onto the linker sequence (yellow/dotted green).

Chapter 4. Discussion

4.1 Generation of an 'allosteric linker' model of CCT regulation by membranes

In this investigation, I established the conserved, flexible linker between the catalytic and membrane-binding regulatory domains of CCT as a transducer of activating allosteric signals. I showed that upon binding of domain M, the linker situates itself near the membrane interface, interacts with lipid acyl chains of a disordered vesicle surface, and appears to form a less stable membrane interaction than domain M. At the same time, hydrophobic residues in αE_C approach the membrane interface and experience quenching by BrPC, suggesting the formation of a compact αE-linker structure that organizes near the surface of the membrane upon domain M membrane binding. Mutagenesis of specific conserved hydrophobic, basic, and aromatic residues in the αE_C and linker destroyed CCT activity, suggesting that this segment is vital for CCT activity. FRET experiments revealed a linker-dependent membrane approach of the catalytic domain, which could occur by a linker conformation positioned at the membrane surface combined with splayed αE helices, stabilized by interactions with the linker. Taken together, this model characterizes CCT's αE_C-linker sequence as an 'allosteric linker' that communicates ligand (membrane) binding signals from a regulatory M domain to promote activation of a physically distinct catalytic domain.

4.2. The linker region is not merely an extension of the M domain or an unstructured tether between αE and M

No structural studies of lipid-regulated CCTs have provided the favoured conformation of the αE_C-linker in active CCT. An initial possibility, supported by the BrPC quenching, could be that that the linker is simply an amphipathic helical extension of domain M. This is not likely for a few reasons. First, Heliquest analysis indicates a very low score for the helical hydrophobic moment of the linker sequence compared to domain M (**Fig. 4.1**). Secondary structure predictions of the linker suggest a coil structure that starts after αE (~ residue 223) and ends at the beginning of domain M (~ residue 234) (**Fig. 4.2**). Secondly, Trps in the linker are quenched by brominated PC to a lesser extent than Trps within the M domain, and the surface proximal bromine

positions (6,7 BrPC) were more effective quenchers. This suggests that the domain M-membrane interaction is more stable than the linker-membrane interaction. The third and most convincing piece of evidence against this hypothesis is the strikingly high sensitivity of CCT activity to mutation. This could not be accounted for if the linker is solely a membrane binding domain. For example, an L230W mutation in the middle of the linker should be beneficial to CCT activation if the linker's primary role is establishing a membrane interaction, but it was devastating to CCT activity.

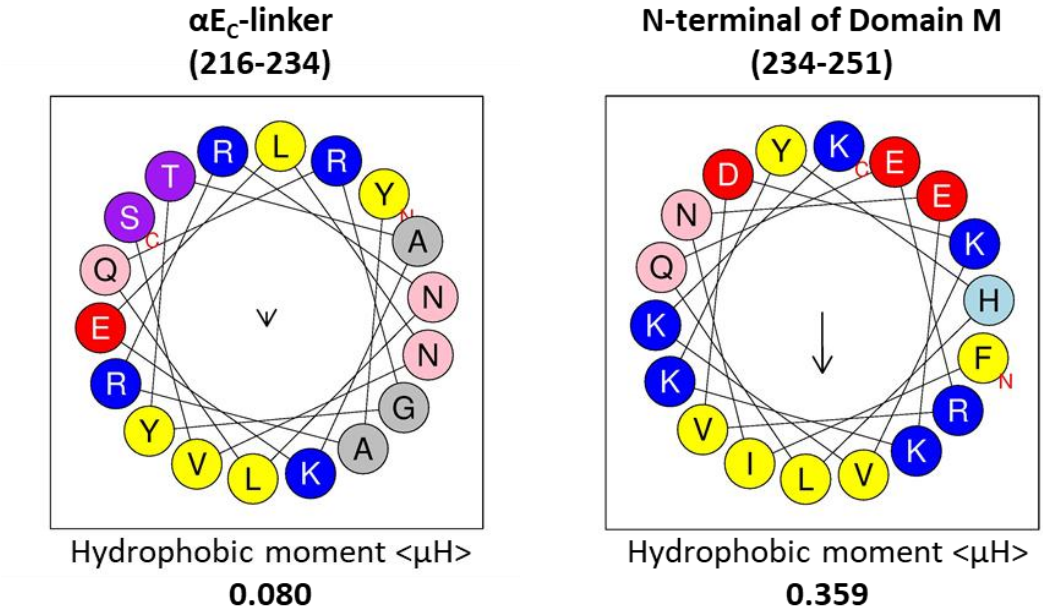

Figure 4.1. *The linker has a much lower hydrophobic moment than domain M.* Helical wheel projections of αE$_C$-linker sequence and 18 N-terminal residues of domain M. Projections and hydrophobic moment values were generated by HeliQuest (92).

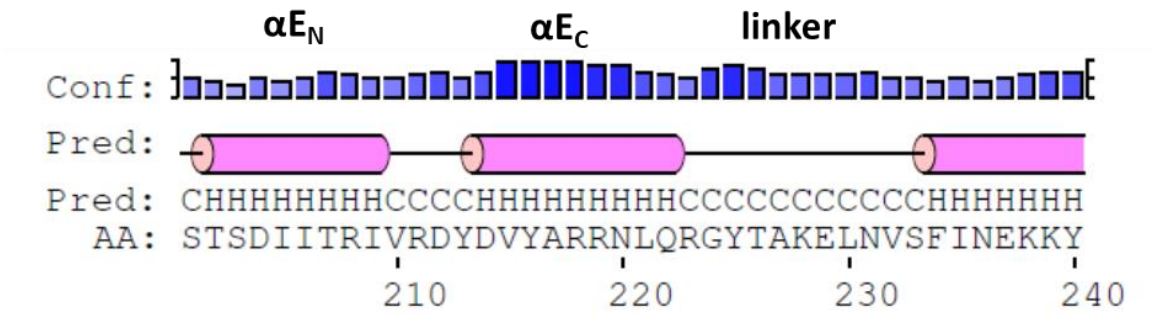

Figure 4.2. *The linker is predicted to be unstructured.* Secondary structure prediction of αE-linker sequence generated by Psipred (93). 'H' represents an α-helix prediction and 'C' represents random coil prediction. Also illustrated is the confidence level of predictions and the sites for Trp substitution.

The data in this thesis also argue against the αE_C-linker sequence as an unstructured tether between the αE_N and domain M or as an unbroken α-helix. If this were the case, the relative distances between Trp residues and the membrane surface would decrease with closer proximity to domain M. However, Trp-dansyl-PE FRET experiments did not show this. The similar, high FRET signals of W216 in the αE_C and W230 in the linker suggest that these residues lie within a similar plane that is parallel to the membrane surface, rather than perpendicular as would be consistent with a continuous α-helix or an unstructured αE_C-linker sequence. The FRET data also positions W124 at a similar distance from the membrane surface as W221 (αE_C) and W225 (linker) despite its position in loop L2, near the active site. The extended, unstructured αE_C-linker sequence would not facilitate this level of membrane approach of the catalytic domain.

The high sequence conservation of the αE_C-linker also does not agree with an extended αE_C and unstructured linker. Conserved residues in this sequence would likely serve no catalytic purpose in active CCT if they were completely solvent-exposed and forged no stable intramolecular or membrane interactions, as would be in an 'extended' αE model. Yet this sequence is as highly conserved as the rest of the catalytic domain, and activity is highly sensitive to mutations in this region. Taken together, the data supports a new allosteric model of CCT activation, in which the αE_C-linker segment acts as a cooperative folding unit upon membrane binding of domain M. This new conformation includes a bending of the αE helices and resultant membrane approach of the catalytic domain, all stabilized perhaps by direct αE_C-linker interactions. This model is supported by some of the insights gained from this study, which are discussed below.

4.3. Multiple conserved residues throughout the αE_C and linker likely contribute to membrane and protein-protein interactions

To assess whether the linker-membrane interaction is required for transducing the membrane binding signals of domain M to the catalytic domain, I tried to disrupt the linker-membrane interaction by mutagenesis. Surprisingly, mutations of sets of three hydrophobic (Triple-A), three basic (Triple-Q), or three aromatic (Triple-Aro) amino acids did not disrupt the positioning of the linker at the membrane but did abolish activation. These results led us to hypothesize that direct interactions between the αE_C and linker sequences were disrupted by the mutations. These interactions would function to create an αE_C-linker conformation essential for transducing signals from the membrane, and the membrane-embedded domain M would contribute to stabilization of this conformation.

One limitation of my experiments monitoring the linker-membrane interaction in the Triple-A, Triple-Q, and Triple-Aro mutants is that the engineered tryptophan probe has a high affinity for membrane interfaces (89,90) and could therefore be artificially forging linker-membrane interactions not available to the wild-type CCT. I engineered Trp probes at Y225 or L221 in these experiments. Y225W is a more conservative change than L221W in terms of the effect on partitioning into the membrane interface, but the interfacial driving force of Trp exceeds that of both Tyr and Leu (89,90). However, given the low observed BrPC quenching at this position, it is not likely that a Trp here would drive a membrane interaction of the entire αE_C-linker sequence. Therefore, it is reasonable to argue that none of the sets of three residues mutated in Triple-A, Triple-Q, or Triple-Aro are solely responsible for the membrane binding propensity of the sequence.

Monitoring BrPC quenching of an engineered W225 in CCT-236 revealed a linker-membrane interaction in the absence of domain M. However, even with the removal of a large region of the linker (Δ227-232), quenching of W225 was not only still observed, but was enhanced. This may be because the linker deletion brings W225 and W234 within close proximity, creating a cluster of hydrophobic residues (two from each monomer) that may artificially promote membrane binding. However, it's still evident that

many of the conserved linker residues are not required for the linker-membrane interaction.

These data imply that the membrane interactions N-terminal to domain M are likely mediated by multiple residues spread out over the αE_C-linker sequence. To disrupt these interactions, it appears to be necessary to delete most or all of it. CCT-236, lacking domain M, co-eluted with lipid micelles in FPLC gel-filtration experiments. Co-elution persisted when a major region of the linker was deleted (Δ227-232). However, when αE_C was also removed (CCT-212), co-elution was not observed, representing a loss of CCT-lipid interaction. Both the αE_C and linker may forge a complex network of protein and lipid interactions, and disruption of this network has devastating effects on the ability to transduce activating signals.

4.4. The compact αE and linker conformation may be stabilized by direct interactions between the two segments

Previously it was shown that a disulfide crosslink (at an engineered C217 site) between adjacent αE_C helices, designed to hinder bending/splaying of the helices, reduced activation by lipids (69). To test whether the high FRET signal observed with W216 is a consequence of a bent αE conformation, I engineered in an αE_C cysteine residue (A217C) in the context of W216 to monitor FRET in oxidized and reduced forms of the dimer. Neither Cu-phenanthroline nor oxidized DTT were able to generate more than ~20% crosslinked (oxidized) dimer (data not shown). This could possibly be due to the bulky nature of the Y216W mutation and its proximity to C217. I therefore took a more indirect approach to prevent αE bending. I mutated the linker to prevent stabilization of an αE_C-linker fold. Mutating a region of the linker to a non-specific, glycine-rich sequence (^{227}GGGSGG^{232}) resulted in reduced FRET of W124 and W216. This supports the model in which a native linker sequence forges specific interactions with the αE_C that stabilize bent αE helices and catalytic domain approach.

A concerning observation comes when comparing the effect of the ^{227}GGGSGG^{232} linker mutation on W124/W216 FRET when monitoring dansyl fluorescence increase (**Fig. 3.13**) vs. monitoring Trp fluorescence decrease (**Fig. 3.15**). The decrease in the FRET signal from both W124 and W216 (especially W124) due to

this linker mutation appears less pronounced when monitoring Trp fluorescence. The effect may not be as pronounced because background FRET (likely from random vesicle collisions) is higher in these experiments (using 10% dansyl-PE vesicles) compared to the FRET experiments in which dansyl fluorescence was monitored (using ~1% dansyl-PE vesicles). The ^{227}GGGSGG^{232} mutation may expose W124 and W216 to solvent due to lack of protection by the αEc, making these sites more susceptible to the random collisions that cause this background FRET, compared to when the sites are buried within the αE_C-linker fold in the context of a wild-type linker.

Structural data of the αE_C-linker sequence performed by other researchers suggests that the region has a propensity to forge interactions within itself and with distal protein sites in the absence of the AI helices. In an unpublished less-stringently refined model of the CCT-236 crystal structure (52), an extra portion of αE_C is resolved and maintains a α-helical structure (J. Lee, unpublished observations). Residues in the sequence form contacts with regions of the CCT crystal symmetry mate. For example, on one chain R219 (αE_C) interacts with F124 (loop L2) backbone carbonyl of the symmetry mate. On the other chain, R218 (αE_C) forms simultaneous interactions with D204 (αE_N) and the backbone carbonyl of G199 (loop L6) of the symmetry mate. These data suggests an αE_C sequence with multiple residues that are prone to form distal molecular interactions, as in the bent αE helices model. In fact, in molecular dynamics simulations performed using the crystal structure data from CCT-236 (B. Holland, *et al*., unpublished), unconstrained αE_C and linker residues transiently forge intra-monomer (cis) and inter-monomer (trans) interactions. In one case, L221 (αE_C) associates with Y225 (linker) in cis during the final ~30 ns of the 200 ns simulation. Meanwhile, E229 (linker) of the same chain is interacting in trans with R218 (αE_C) for the majority of the simulation (~160 ns). If the αE_C has a high propensity to form interactions as suggested by these data, it's possible that the linker fulfills the role of stabilizing an active conformation of αE_C that, in turn, promotes the αE_C to form important activating interactions (i.e. with loop L2 or active site residues/substrate). Analysis of simulation structures with bent αE helices reveals a hydrophobic groove between the two αE_C helices situated near the membrane-bound side of the CCT dimer (**Fig. 4.3**). This groove may accommodate the linker sequence, allowing it to form interactions with both the αE_C and membrane.

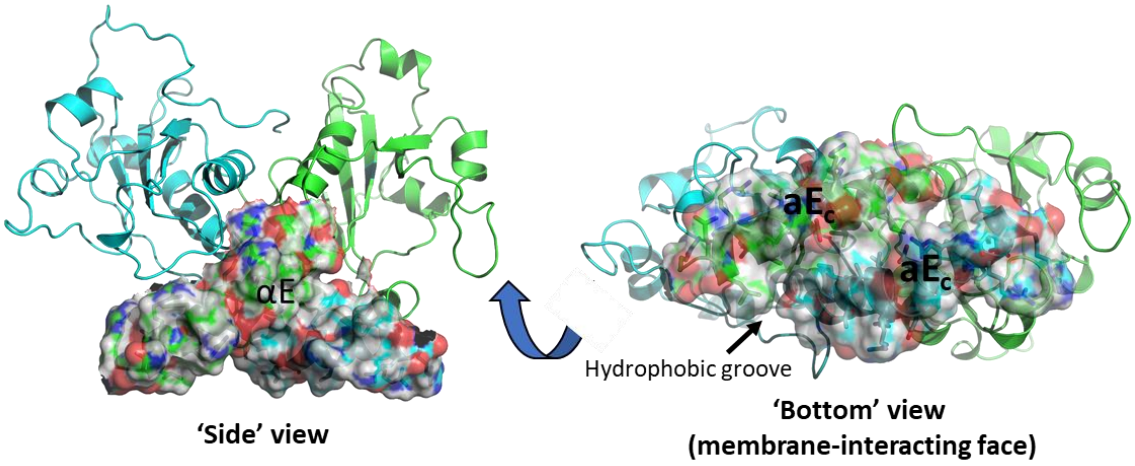

Figure 4.3. *Bent αE helices could provide a hydrophobic groove in which the linker could position itself during CCT activation.* Catalytic dimer with bent αE helices derived from simulation files from Ramezanpour and Lee, *et al* (69). Surface charge of the αE region is shown from two different views and reveals a hydrophobic groove on the membrane-binding face ('bottom' view) of CCT.

Strong indirect evidence for αE_C-linker interactions comes from co-evolution sequence analysis of the two sequences (**Fig. 4.4**). If amino acid substitutions in the αE_C are found in a specific clade of the phylogenetic tree, we can look for complementary substitutions in the linker sequence that suggest an interaction between the two substituted residues. We compiled sequences from a wide range of eukaryotic species covering various phyla and executed a sequence alignment to reveal possible substitution sites. One striking substitution occurred in Ascomycota fungi sequences. Position 221 in the αE_C which is a leucine in most species, is mutated to a phenylalanine, and in concert position 225 in the linker is changed from tyrosine to alanine. If co-evolution of the αE_C and linker sequences occurred, then the L221F/Y225A switch would imply that these two residues interact and having two bulky, aromatic side chains at these positions would create a steric clash and inefficient CCT catalysis. This conclusion is also suggested in the results from this study, which uses the rat CCT sequence. A Y225W mutation has far less impact on lipid-dependent activity compared to a L221W mutation, as in the latter there is an aromatic residue at both positions (W221/Y225).

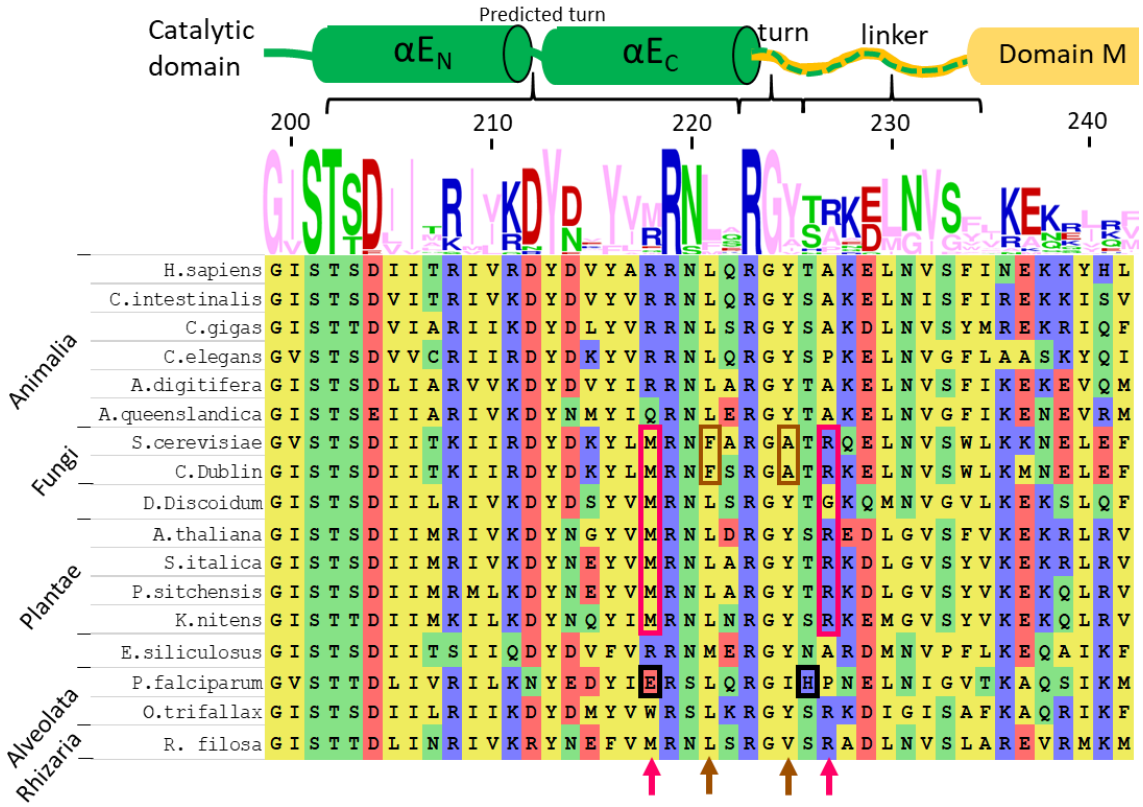

Figure 4.4. *The αE and linker sequences are highly conserved across eukaryotes but also possess specific cooperative mutations that may indicate sites of interaction.* Phosphocholine cytidylyltransferase sequences were loaded into ClustalX2 and subjected to a multiple sequence alignment. The alignment was coloured using: https://www.bioinformatics.org/sms/multi_align.html. The WebLogo tool: https://weblogo.berkeley.edu/logo.cgi was used to create the sequence logo. Accession: H. sapiens (human; P49585 - UniProt), C.intestinalis (sea squirt; A0A1W2WNC7 - UniProt), C.gigas (oyster; K1R1B8 - UniProt), C.elegans (nematode; Q3HKC4 - UniProt), A.digitifera (coral; XP_015766472.1 - NCBI), A.queenslandica (sponge; XP_003383158.1 - NCBI), S.cerevisiae (yeast; P13259 - UniProt), C.Dublin (fungal parasite; B9WFD0 - UniProt), D.Discoidum (slime mold; Q54GD2 - UniProt), A.thaliana (flowering plant; Q9ZV56 - UniProt), S.italica (seeded grass; K3YU76 - UniProt), P.sitchensis (coniferous tree; C0PTF1 - UniProt), K.nitens (green algae; A0A1Y1INE6 - UniProt), E.siliculosus (brown algae; D8LPY9- UniProt), P.falciparum (apicomplexan; P49587 - UniProt), O.trifallax (ciliate; J9HWN9 - UniProt), R. filosa (foraminiferans; X6NBS6 - UniProt). Sequences with the L221F/Y225A switch are highlighted in brown (with brown arrows indicating these positions). The basic residue switch between residues 218 and 227 is highlighted in pink (with pink arrows indicating these positions). The E218/H226 pair found in *P. falciparum* is highlighted in black.

I attempted to rescue activity of the L221W rat CCT mutant by introducing an alanine at position 225 to prevent the potential steric clash (W221/A225). However, activity was not restored (data not shown). In an attempt to more accurately replicate the Ascomycota fungi sequence, I switched the tryptophan at position 221 for phenylalanine, mimicking the L221F/Y225A switch. This also did not restore lipid-dependent activity of rat CCT (data not shown). It is likely that this switch only restores activity in the context of the fungi sequences. Therefore, its seems that stable αE_C-linker interactions require a finely-tuned (and species-specific) sequence to optimize all the specific residue-residue interactions.

Other clues in the sequence alignment hint at specific αE_C-linker interactions (**Fig. 4.4**). For example, in the identified plant/fungi sequences, residue 218 in the αE_C is a methionine switched from an arginine in animal sequences. In these same organisms, residue 227 in the linker is an arginine switched from an alanine or proline in other sequences. This observation suggests that a positively-charged arginine residue is not tolerated at both these positions as it would create electrostatic repulsion, and active CCT requires them to be closely associated. In another interesting case, residue 218 in the protozoan *P. falciparum* is switched to a negatively-charged glutamate. In this sequence, residue 226 is a basic histidine, whereas in every other sequence in the alignment, this position is an uncharged residue. Overall, these amino acid switches in the αE_C-linker sequence suggest a model for active, membrane-bound CCT where there is a turn around G224 that enables interactions between C-terminal αE_C residues and N-terminal linker residues. The interactions could propagate to the N-terminal of the αE_C and C-terminal of the linker, like a zipper. Trp mutations that might disrupt interactions further away from the αE_C-linker boundary turn appeared to have greater effects on activation (i.e. V232W > L230W > L221W in terms of degree of activity perturbation). Perhaps these interactions are the most vital to maintain the overall structure of the αE_C-linker complex in membrane-bound CCT.

4.5. How could a membrane-triggered compact αE_C – linker aid catalysis?

Bending of the αE helices positions conserved residues of one face of the αE_C within close proximity to the epicentre of CCT catalysis, loop L2 and the active site. The opposite face of the helix could orient towards the linker near the membrane interface,

forging both protein and lipid interactions (**Fig. 3.15**). Both sets of interactions may be important for stabilizing an αE_C helical structure, compensating for contacts lost during AI helices dissociation. For example, Y216 interacts with the AI helices in soluble CCT, and simulation data along with the data shown here suggests that it forms new protein contacts when CCT binds membranes. Stable loop L2-αE_C interactions could be important for preventing the carbonyl oxygen of F124 from contributing to the electrostatic pull of the catalytic residue, K122, away from the active site (60). More generally, these interactions may promote a loop L2 configuration that enhances interactions between K122 and substrate. R223 at the C-terminal of αE_C has been shown in simulations to form direct contacts with CTP in the active site (69). This contact is only possible through a bent αE helices model and could be a physiologically important contact for stabilizing substrate binding or promoting interactions between CTP and K122 or CTP and phosphocholine. The position of R223 at the start of a turn at the αE-linker boundary, suggests that it would not likely forge interactions with the linker. But its highly conserved nature points to a vital role in CCT catalysis, and stabilizing substrate in the active site may be this role.

Ramezanpour and Lee, *et al*. (69) proposed that when substrate binds membrane-bound CCT, the αE helices may stabilize in a bent conformation, closing off the active site route of entry. This protection from solvent could prevent hydrolysis of the active site-contorted CTP, allowing only nucleophilic attack of the CTP α-phosphate by phosphocholine. This may contribute to the overall enhancement of catalysis by membrane-binding, acting in concert with more direct mechanisms. Regardless of the mechanism of action, the fact that cytidylyltransferases that are not regulated by membranes lack the αE_C and linker sequences strongly suggests they serve an important role specifically in membrane-dependent activation. CCT's interdomain linker is clearly a finely-tuned sequence that takes on specific favoured conformations and plays active roles in maintaining regulation of CCT activity, and thus, the membrane composition of eukaryotic cells.

Recent structural studies have been elucidating interdomain linkers as mediators of allosteric signalling in a variety of allosterically-regulated proteins, including transcription factors/nuclear receptors (94), neurotransmitter receptors (95), chaperones (6,96) and a variety of enzymes (97-99). Reported models of allostery include direct interactions between flexible linkers and catalytic domains to promote catalysis (97)

along with allosteric linkers that induce repositioning of entire catalytic domains to promote substrate access (99). CCT's linker, which tethers its catalytic and membrane-binding regulatory domains, provides a unique example of how an allosteric linker can regulate the activation of enzymes that reversibly bind membranes. This study serves as a stepping stone to uncovering the full activation mechanism of CCT, which undoubtedly will be facilitated by the solving of high resolution structures of CCT in its lipid-bound, active form.

References

1. Henzler-Wildman, K., and Kern, D.(2007) Dynamic personalities of proteins. *Nature* **450**, 964-972
2. Apic, G., Huber, W., and Teichmann, S. A.(2003) Multi-domain protein families and domain pairs: comparison with known structures and a random model of domain recombination. *J Struct Funct Genomics* **4**, 67-78
3. Ma, B., Tsai, C. J., Haliloglu, T., and Nussinov, R.(2011) Dynamic allostery: linkers are not merely flexible. *Structure* **19**, 907-917
4. Kim, C., Xuong, N. H., and Taylor, S. S.(2005) Crystal structure of a complex between the catalytic and regulatory (RIalpha) subunits of PKA. *Science* **307**, 690-696
5. Akimoto, M., Selvaratnam, R., McNicholl, E. T., Verma, G., Taylor, S. S., and Melacini, G.(2013) Signaling through dynamic linkers as revealed by PKA. *Proc Natl Acad Sci U S A* **110**, 14231-14236
6. English, C. A., Sherman, W., Meng, W., and Gierasch, L. M.(2017) The Hsp70 interdomain linker is a dynamic switch that enables allosteric communication between two structured domains. *J Biol Chem* **292**, 14765-14774
7. Hartl, F. U., and Hayer-Hartl, M.(2002) Molecular chaperones in the cytosol: from nascent chain to folded protein. *Science* **295**, 1852-1858
8. Liu, Q., and Hendrickson, W. A.(2007) Insights into Hsp70 chaperone activity from a crystal structure of the yeast Hsp110 Sse1. *Cell* **131**, 106-120
9. Johnson, J. E., and Cornell, R. B.(1999) Amphitropic proteins: regulation by reversible membrane interactions (review). *Mol Membr Biol* **16**, 217-235
10. McLaughlin, S., and Aderem, A.(1995) The myristoyl-electrostatic switch: a modulator of reversible protein-membrane interactions. *Trends Biochem Sci* **20**, 272-276
11. Hyvonen, M., Macias, M. J., Nilges, M., Oschkinat, H., Saraste, M., and Wilmanns, M.(1995) Structure of the binding site for inositol phosphates in a PH domain. *Embo J* **14**, 4676-4685
12. Cantley, L. C.(2002) The phosphoinositide 3-kinase pathway. *Science* **296**, 1655-1657
13. Lumb, C. N., and Sansom, M. S.(2012) Finding a needle in a haystack: the role of electrostatics in target lipid recognition by PH domains. *PLoS Comput Biol* **8**, e1002617
14. Drin, G., and Antonny, B.(2010) Amphipathic helices and membrane curvature. *FEBS Lett* **584**, 1840-1847
15. Wieprecht, T., Apostolov, O., Beyermann, M., and Seelig, J.(1999) Thermodynamics of the alpha-helix-coil transition of amphipathic peptides in a membrane environment: implications for the peptide-membrane binding equilibrium. *J Mol Biol* **294**, 785-794

16. Goldenberg, N. M., and Steinberg, B. E.(2010) Surface charge: a key determinant of protein localization and function. *Cancer Res* **70**, 1277-1280

17. Cullis, P. R., and de Kruijff, B.(1979) Lipid polymorphism and the functional roles of lipids in biological membranes. *Biochim Biophys Acta* **559**, 399-420

18. Gruner, S. M., Cullis, P. R., Hope, M. J., and Tilcock, C. P.(1985) Lipid polymorphism: the molecular basis of nonbilayer phases. *Annu Rev Biophys Biophys Chem* **14**, 211-238

19. Kent, C.(1997) CTP:phosphocholine cytidylyltransferase. *Biochim Biophys Acta* **1348**, 79-90

20. Cornell, R. B.(2016) Membrane lipid compositional sensing by the inducible amphipathic helix of CCT. *Biochim Biophys Acta* **1861**, 847-861

21. Craig, L., Johnson, J. E., and Cornell, R. B.(1994) Identification of the membrane-binding domain of rat liver CTP: phosphocholine cytidylyltransferase using chymotrypsin proteolysis. *J Biol Chem* **269**, 3311-3317

22. Dunne, S. J., Cornell, R. B., Johnson, J. E., Glover, N. R., and Tracey, A. S.(1996) Structure of the membrane binding domain of CTP: phosphocholine cytidylyltransferase. *Biochemistry* **35**, 11975-11984

23. Johnson, J. E., and Cornell, R. B.(1994) Membrane-binding amphipathic alpha-helical peptide derived from CTP:phosphocholine cytidylyltransferase. *Biochemistry* **33**, 4327-4335

24. Kalmar, G. B., Kay, R. J., Lachance, A., Aebersold, R., and Cornell, R. B.(1990) Cloning and expression of rat liver CTP: phosphocholine cytidylyltransferase: an amphipathic protein that controls phosphatidylcholine synthesis. *Proc Natl Acad Sci* **87**, 6029-6033

25. McMaster, C. R.(2018) From yeast to humans–roles of the Kennedy pathway for phosphatidylcholine synthesis. *FEBS Lett* **592**, 1256-1272

26. Cornell, R. B., and Taneva, S. G.(2006) Amphipathic helices as mediators of the membrane interaction of amphitropic proteins, and as modulators of bilayer physical properties. *Curr Protein Pept Sci* **7**, 539-552

27. Arnold, R. S., and Cornell, R. B.(1996) Lipid regulation of CTP: phosphocholine cytidylyltransferase: electrostatic, hydrophobic, and synergistic interactions of anionic phospholipids and diacylglycerol. *Biochemistry* **35**, 9917-9924

28. Fagone, P., and Jackowski, S.(2013) Phosphatidylcholine and the CDP-choline cycle. *Biochim Biophys Acta* **1831**, 523-532

29. Houweling, M., Cui, Z., Anfuso, C., Bussiere, M., Chen, M., and Vance, D.(1996) CTP: phosphocholine cytidylyltransferase is both a nuclear and cytoplasmic protein in primary hepatocytes. *Eur J Cell Biol* **69**, 55-63

30. Wang, Y., Sweitzer, T., Weinhold, P. A., and Kent, C.(1993) Nuclear localization of soluble CTP: phosphocholine cytidylyltransferase. *J Biol Chem* **268**, 5899-5904

31. Haider, A., Wei, Y.-C., Lim, K., Barbosa, A. D., Liu, C.-H., Weber, U., Mlodzik, M., Oras, K., Collier, S., and Hussain, M. M.(2018) PCYT1A Regulates Phosphatidylcholine Homeostasis from the Inner Nuclear Membrane in

Response to Membrane Stored Curvature Elastic Stress. *Develop Cell* **45**, 481-495. e488

32. Lykidis, A., Baburina, I., and Jackowski, S.(1999) Distribution of CTP: phosphocholine cytidylyltransferase (CCT) isoforms identification of a new CCTβ splice variant. *J Biol Chem* **274**, 26992-27001

33. Lykidis, A., Murti, K. G., and Jackowski, S.(1998) Cloning and characterization of a second human CTP: phosphocholine cytidylyltransferase. *J Biol Chem* **273**, 14022-14029

34. Zhang, D., Tang, W., Yao, P. M., Yang, C., Xie, B., Jackowski, S., and Tabas, I.(2000) Macrophages deficient in CTP:Phosphocholine cytidylyltransferase-alpha are viable under normal culture conditions but are highly susceptible to free cholesterol-induced death. Molecular genetic evidence that the induction of phosphatidylcholine biosynthesis in free cholesterol-loaded macrophages is an adaptive response. *J Biol Chem* **275**, 35368-35376

35. Bremer, J., and Greenberg, D. M.(1961) Methyl transfering enzyme system of microsomes in the biosynthesis of lecithin (phosphatidylcholine). *Biochim Biophys Acta* **46**, 205-216

36. Hörl, G., Wagner, A., Cole, L. K., Malli, R., Reicher, H., Kotzbeck, P., Köfeler, H., Höfler, G., Frank, S., and Bogner-Strauss, J. G.(2011) Sequential synthesis and methylation of phosphatidylethanolamine promote lipid droplet biosynthesis and stability in tissue culture and in vivo. *J Biol Chem* **286**, 17338-17350

37. Ridgway, N. D.(1989) Phosphatidylethanolamine N-methyltransferase. *Phosphatidylcholine Metabolism*, 103-120

38. Walkey, C. J., Donohue, L. R., Bronson, R., Agellon, L. B., and Vance, D. E.(1997) Disruption of the murine gene encoding phosphatidylethanolamine N-methyltransferase. *Proc Natl Acad Sci U S A* **94**, 12880-12885

39. Walkey, C. J., Yu, L., Agellon, L. B., and Vance, D. E.(1998) Biochemical and evolutionary significance of phospholipid methylation. *J Biol Chem* **273**, 27043-27046

40. Cornell, R. B., and Ridgway, N. D.(2015) CTP: phosphocholine cytidylyltransferase: function, regulation, and structure of an amphitropic enzyme required for membrane biogenesis. *Prog Lipid Res* **59**, 147-171

41. Wang, L., Magdaleno, S., Tabas, I., and Jackowski, S.(2005) Early embryonic lethality in mice with targeted deletion of the CTP: phosphocholine cytidylyltransferase α gene (Pcyt1a). *Mol Cell Biol* **25**, 3357-3363

42. Cui, Z., Houweling, M., Chen, M. H., Record, M., Chap, H., Vance, D. E., and Tercé, F.(1996) A genetic defect in phosphatidylcholine biosynthesis triggers apoptosis in Chinese hamster ovary cells. *J Biol Chem* **271**, 14668-14671

43. McMaster, C. R.(2001) Lipid metabolism and vesicle trafficking: more than just greasing the transport machinery. *Biochem Cell Biol* **79**, 681-692

44. Tian, Y., Pate, C., Andreolotti, A., Wang, L., Tuomanen, E., Boyd, K., Claro, E., and Jackowski, S.(2008) Cytokine secretion requires phosphatidylcholine synthesis. *J Cell Biol* **181**, 945-957

45. Exton, J.(1994) Phosphatidylcholine breakdown and signal transduction. *Biochim Biophys Acta* **1212**, 26-42

46. Bangham, A., Morley, C., and Phillips, M.(1979) The physical properties of an effective lung surfactant. *Biochim Biophys Acta* **573**, 552-556

47. Tian, Y., Zhou, R., Rehg, J. E., and Jackowski, S.(2007) Role of phosphocholine cytidylyltransferase α in lung development. *Mol Cell Biol* **27**, 975-982

48. Jacobs, R. L., Devlin, C., Tabas, I., and Vance, D. E.(2004) Targeted deletion of hepatic CTP: phosphocholine cytidylyltransferase a in mice decreases plasma high density and very low density lipoproteins. *J Biol Chem* **279**, 47402–47410

49. Carter, J. M., Demizieux, L., Campenot, R. B., Vance, D. E., and Vance, J. E.(2008) Phosphatidylcholine Biosynthesis via CTP: Phosphocholine Cytidylyltransferase β2 Facilitates Neurite Outgrowth and Branching. *J Biol Chem* **283**, 202-212

50. Strakova, J., Demizieux, L., Campenot, R. B., Vance, D. E., and Vance, J. E.(2011) Involvement of CTP: phosphocholine cytidylyltransferase-β2 in axonal phosphatidylcholine synthesis and branching of neurons. *Biochim Biophys Acta* **1811**, 617-625

51. Dennis, M. K., Taneva, S. G., and Cornell, R. B.(2011) The intrinsically disordered nuclear localization signal and phosphorylation segments distinguish the membrane affinity of two cytidylyltransferase isoforms. *J Biol Chem* **286**, 12349-12360

52. Lee, J., Johnson, J., Ding, Z., Paetzel, M., and Cornell, R. B.(2009) Crystal structure of a mammalian CTP: phosphocholine cytidylyltransferase catalytic domain reveals novel active site residues within a highly conserved nucleotidyltransferase fold. *J Biol Chem* **284**, 33535-33548

53. Johnson, J. E., Rao, N. M., Hui, S.-W., and Cornell, R. B.(1998) Conformation and lipid binding properties of four peptides derived from the membrane-binding domain of CTP: phosphocholine cytidylyltransferase. *Biochemistry* **37**, 9509-9519

54. Taneva, S., Johnson, J. E., and Cornell, R. B.(2003) Lipid-induced conformational switch in the membrane binding domain of CTP: phosphocholine cytidylyltransferase: a circular dichroism study. *Biochemistry* **42**, 11768-11776

55. Friesen, J. A., Campbell, H. A., and Kent, C.(1999) Enzymatic and cellular characterization of a catalytic fragment of CTP: phosphocholine cytidylyltransferase α. *J Biol Chem* **274**, 13384-13389

56. MacDonald, J., and Kent, C.(1994) Identification of phosphorylation sites in rat liver CTP: phosphocholine cytidylyltransferase. *J Biol Chem* **269**, 10529-10537

57. Chong, S. S., Taneva, S. G., Lee, J. M., and Cornell, R. B.(2014) The curvature sensitivity of a membrane-binding amphipathic helix can be modulated by the charge on a flanking region. *Biochemistry* **53**, 450-461

58. Yang, W., and Jackowski, S.(1995) Lipid activation of CTP: phosphocholine cytidylyltransferase is regulated by the phosphorylated carboxyl-terminal domain. *J Biol Chem* **270**, 16503-16506

59. Arnold, R. S., DePaoli-Roach, A. A., and Cornell, R. B.(1997) Binding of CTP: phosphocholine cytidylyltransferase to lipid vesicles: diacylglycerol and enzyme dephosphorylation increase the affinity for negatively charged membranes. *Biochemistry* **36**, 6149-6156

60. Lee, J., Taneva, S. G., Holland, B. W., Tieleman, D. P., and Cornell, R. B.(2014) Structural basis for autoinhibition of CTP: phosphocholine cytidylyltransferase (CCT), the regulatory enzyme in phosphatidylcholine synthesis, by its membrane-binding amphipathic helix. *J Biol Chem* **289**, 1742-1755

61. Rao, S. T., and Rossmann, M. G.(1973) Comparison of super-secondary structures in proteins. *J Mol Biol* **76**, 241-256

62. Weber, C. H., Park, Y. S., Sanker, S., Kent, C., and Ludwig, M. L.(1999) A prototypical cytidylyltransferase: CTP: glycerol-3-phosphate cytidylyltransferase from Bacillus subtilis. *Structure* **7**, 1113-1124

63. Helmink, B. A., Braker, J. D., Kent, C., and Friesen, J. A.(2003) Identification of lysine 122 and arginine 196 as important functional residues of rat CTP:phosphocholine cytidylyltransferase alpha. *Biochemistry* **42**, 5043-5051

64. Veitch, D. P., and Cornell, R. B.(1996) Substitution of serine for glycine-91 in the HXGH motif of CTP:phosphocholine cytidylyltransferase implicates this motif in CTP binding. *Biochemistry* **35**, 10743-10750

65. Veitch, D. P., Gilham, D., and Cornell, R. B.(1998) The role of histidine residues in the HXGH site of CTP:phosphocholine cytidylyltransferase in CTP binding and catalysis. *Eur J Biochem* **255**, 227-234

66. Huang, H. K., Taneva, S. G., Lee, J., Silva, L. P., Schriemer, D. C., and Cornell, R. B.(2013) The membrane-binding domain of an amphitropic enzyme suppresses catalysis by contact with an amphipathic helix flanking its active site. *J Mol Biol* **425**, 1546-1564

67. Wang, Y., and Kent, C.(1995) Identification of an inhibitory domain of CTP: phosphocholine cytidylyltransferase. *J Biol Chem* **270**, 18948-18952

68. Ding, Z., Taneva, S. G., Huang, H. K., Campbell, S. A., Semenec, L., Chen, N., and Cornell, R. B.(2012) A 22-mer segment in the structurally pliable regulatory domain of metazoan CTP: phosphocholine cytidylyltransferase facilitates both silencing and activating functions. *J Biol Chem* **287**, 38980-38991

69. Ramezanpour, M., Lee, J., Taneva, S. G., Tieleman, D. P., and Cornell, R. B.(2018) An auto-inhibitory helix in CTP:phosphocholine cytidylyltransferase hijacks the catalytic residue and constrains a pliable, domain-bridging helix pair. *J Biol Chem* **293**, 7070-7084

70. Lee, J., Johnson, J. E., Ding, Z., Paetzel, M., and Cornell, R. B.(2009) Crystal Structure of a mammalian CTP: Phosphocholine cytidylyltransferase catalytic domain reveals novel active site residues within a highly conserved nucleotidyl-transferase fold. *J Biol Chem* **284**, 33535–33548.

71. Bogan, M. J., Agnes, G. R., Pio, F., and Cornell, R. B.(2005) Interdomain and membrane interactions of CTP:phosphocholine cytidylyltransferase revealed via limited proteolysis and mass spectrometry. *J Biol Chem* **280**, 19613-19624

72. Xie, M., Smith, J. L., Ding, Z., Zhang, D., and Cornell, R. B.(2004) Membrane binding modulates the quaternary structure of CTP: phosphocholine cytidylyltransferase. *J Biol Chem* **279**, 28817-28825

73. Lakowicz, J. R. (2006) *Principles of fluorescence spectroscopy*, 3rd ed., Springer, New York

74. Chen, Y., and Barkley, M. D.(1998) Toward understanding tryptophan fluorescence in proteins. *Biochemistry* **37**, 9976-9982

75. McIntosh, T. J., and Holloway, P. W.(1987) Determination of the depth of bromine atoms in bilayers formed from bromolipid probes. *Biochemistry* **26**, 1783-1788

76. Pfefferkorn, C. M., Walker, R. L., 3rd, He, Y., Gruschus, J. M., and Lee, J. C.(2015) Tryptophan probes reveal residue-specific phospholipid interactions of apolipoprotein C-III. *Biochim Biophys Acta* **1848**, 2821-2828

77. Bolen, E. J., and Holloway, P. W.(1990) Quenching of tryptophan fluorescence by brominated phospholipid. *Biochemistry* **29**, 9638-9643

78. Taneva, S., Dennis, M. K., Ding, Z., Smith, J. L., and Cornell, R. B.(2008) Contribution of each membrane binding domain of the CTP:phosphocholine cytidylyltransferase-alpha dimer to its activation, membrane binding, and membrane cross-bridging. *J Biol Chem* **283**, 28137-28148

79. QIAprep, Q., and Kit, M.(Cat. No. 27016. *QIAprep Miniprep Handbook: QIAprep Spin Miniprep Kit Protocol*, 22

80. Johnson, J. E., Xie, M., Singh, L. M., Edge, R., and Cornell, R. B.(2003) Both acidic and basic amino acids in an amphitropic enzyme, CTP: phosphocholine cytidylyltransferase, dictate its selectivity for anionic membranes. *J Biol Chem* **278**, 514-522

81. Bradford, M. M.(1976) A rapid and sensitive method for the quantitation of microgram quantities of protein utilizing the principle of protein-dye binding. *Anal Biochem* **72**, 248-254

82. Bartlett, G. R.(1959) Phosphorus assay in column chromatography. *J Biol Chem* **234**, 466-468

83. Lavinder, J. J., Hari, S. B., Sullivan, B. J., and Magliery, T. J.(2009) High-throughput thermal scanning: a general, rapid dye-binding thermal shift screen for protein engineering. *J Am Chem Soc* **131**, 3794-3795

84. Poehling, H. M., and Neuhoff, V.(1981) Visualization of proteins with a silver “stain”: a critical analysis. *Electrophoresis* **2**, 141-147

85. Aoki, S., and Epand, R. M.(2012) Caveolin-1 hydrophobic segment peptides insertion into membrane mimetic systems: role of proline residue. *Biochim Biophys Acta* **1818**, 12-18

86. Christiaens, B., Symoens, S., Verheyden, S., Engelborghs, Y., Joliot, A., Prochiantz, A., Vandekerckhove, J., Rosseneu, M., and Vanloo, B.(2002) Tryptophan fluorescence study of the interaction of penetratin peptides with model membranes. *Eur J Biochem* **269**, 2918-2926

87. van Rooijen, B. D., van Leijenhorst-Groener, K. A., Claessens, M. M., and Subramaniam, V.(2009) Tryptophan fluorescence reveals structural features of alpha-synuclein oligomers. *J Mol Biol* **394**, 826-833

88. Harada, R., Sugita, Y., and Feig, M.(2012) Protein crowding affects hydration structure and dynamics. *J Am Chem Soc* **134**, 4842-4849

89. MacCallum, J. L., Bennett, W. F., and Tieleman, D. P.(2008) Distribution of amino acids in a lipid bilayer from computer simulations. *Biophys J* **94**, 3393-3404

90. Wimley, W. C., and White, S. H.(1996) Experimentally determined hydrophobicity scale for proteins at membrane interfaces. *Nat Struct Biol* **3**, 842-848

91. Taneva, S. G., Lee, J. M., and Cornell, R. B.(2012) The amphipathic helix of an enzyme that regulates phosphatidylcholine synthesis remodels membranes into highly curved nanotubules. *Biochim Biophys Acta* **1818**, 1173-1186

92. Gautier, R., Douguet, D., Antonny, B., and Drin, G.(2008) HELIQUEST: a web server to screen sequences with specific α-helical properties. *Bioinformatics* **24**, 2101-2102

93. Jones, D. T.(1999) Protein secondary structure prediction based on position-specific scoring matrices1. *J Mol Biol* **292**, 195-202

94. Meijsing, S. H., Pufall, M. A., So, A. Y., Bates, D. L., Chen, L., and Yamamoto, K. R.(2009) DNA binding site sequence directs glucocorticoid receptor structure and activity. *Science* **324**, 407-410

95. Gielen, M., Siegler Retchless, B., Mony, L., Johnson, J. W., and Paoletti, P.(2009) Mechanism of differential control of NMDA receptor activity by NR2 subunits. *Nature* **459**, 703-707

96. Vogel, M., Mayer, M. P., and Bukau, B.(2006) Allosteric regulation of Hsp70 chaperones involves a conserved interdomain linker. *J Biol Chem* **281**, 38705-38711

97. Airola, M. V., Shanbhogue, P., Shamseddine, A. A., Guja, K. E., Senkal, C. E., Maini, R., Bartke, N., Wu, B. X., Obeid, L. M., Garcia-Diaz, M., and Hannun, Y. A.(2017) Structure of human nSMase2 reveals an interdomain allosteric activation mechanism for ceramide generation. *Proc Natl Acad Sci U S A* **114**, E5549-E5558

98. Liu, J., and Nussinov, R.(2010) Molecular dynamics reveal the essential role of linker motions in the function of cullin-RING E3 ligases. *J Mol Biol* **396**, 1508-1523

99. Pandit, J., Forman, M. D., Fennell, K. F., Dillman, K. S., and Menniti, F. S.(2009) Mechanism for the allosteric regulation of phosphodiesterase 2A deduced from the X-ray structure of a near full-length construct. *Proc Natl Acad Sci U S A* **106**, 18225-18230

Appendices

Appendix A Removal of NLS prevents vesicle aggregation and sample turbidity in CCT312-His

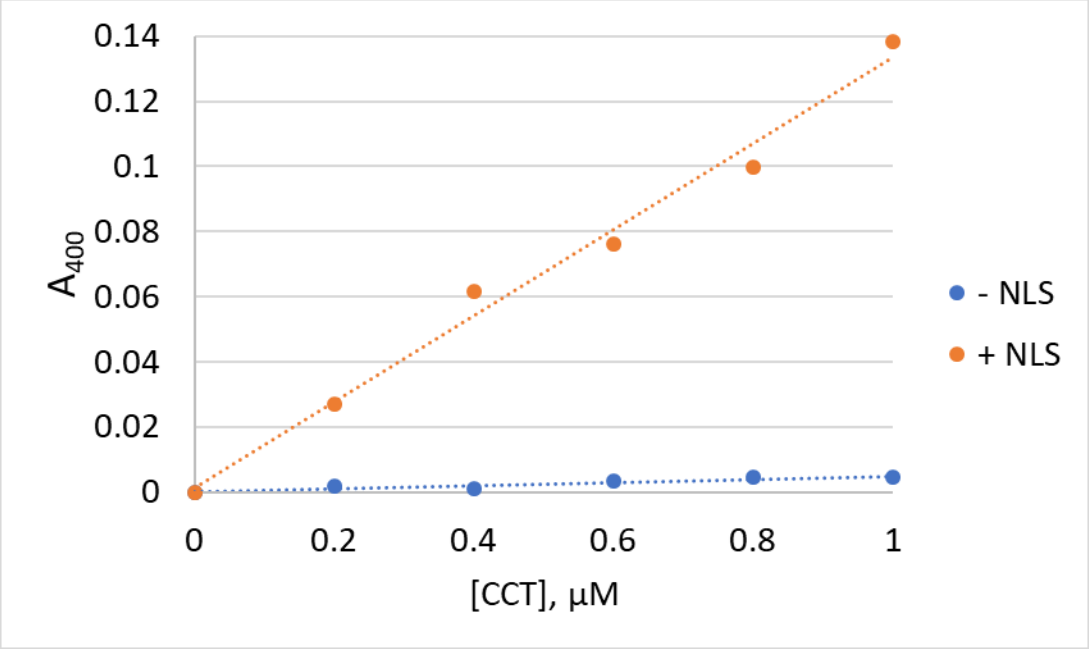

Absorbance at 400 nm was measured with increasing [CCT] to monitor the effects of the NLS on turbidity of samples containing CCT312-His constructs. Vesicle cross-bridging caused by multiple vesicle-binding sites on CCT constructs causes increased sample turbidity. The constructs used were CCT312-His L221W (orange) and CCT312-His L221W ΔNLS (blue). The results showed that the ΔNLS (Δ12-16) mutation prevents vesicle cross-bridging and sample turbidity in CCT312-His and so this mutation was made in all constructs to prevent optical interference in fluorescence experiments. Absorbance at 400 nm from protein blanks was subtracted in the plotted data.

Appendix B Polymerase chain reaction parameters for site-directed mutagenesis

Reaction components (in 50µL reaction)

DNA template, pET24a or pET14b (50 ng)

Sense primer (125 ng)

Anti-sense primer (125 ng)

dNTP (200 µM)

MgSO4 (2 mM)

Pfu DNA polymerase (2.5 Units)

20 mM Tris HCl (pH 8.8)

10 mM KCl

10 mM $(NH_4)_2SO_4$

5 µg BSA

0.1% Triton X-100

Thermocycler parameters:

1.	95°C	30 sec.	
2.	95°C	30 sec.	16 cycles
3.	55°C	1 min.	
4.	68°C	7 min.	
5.	68°C	8 min.	
6.	4°C	∞	

Appendix C List of protease inhibitors

Protease Inhibitor	Stock Concentration	Working Concentration
Leupeptin (2.5 µg/ml)	5 mg/mL in H_2O	2.5 µg/mL
Chymostatin (2 µg/ml)	2.5 mg/mL in DMSO	2 µg/mL
Antipain (1 µg/ml)	5 mg/mL in H_2O	1 µg/mL
Pepstatin (2 µg/ml)	5 mg/mL in DMSO	2 µg/mL
p-amino-benzadine (10 µg/ml)	10 mg/mL in H_2O	10 µg/mL
Benzamidine (10 µg/ml)	10 mg/mL in H_2O	10 µg/mL
PMSF (2 mM)	0.5 M in DMSO (87 mg/mL)	2 mM

Appendix D List of purified CCT mutants and cellular fraction from which they were purified

Construct	Purification
CCT312His Δ12-16	Whole cell
CCT312His Δ12-16 (W151F)	Pellet
CCT312His Δ12-16 (W278F)	Pellet
CCT312His Δ12-16 F55W (W151F, W278F)	Whole cell
CCT312His Δ12-16 F121W (W151F, W278F)	Whole cell
CCT312His Δ12-16 F124W (W151F, W278F)	Whole cell
CCT312His Δ12-16 F124W ^{227}GGGSGG^{232} (W151F, W278F)	Whole cell
CCT312His Δ12-16 Y216W (W278F)	Pellet
CCT312His Δ12-16 Y216W (W151F, W278F)	Pellet
CCT312His Δ12-16 Y216W ^{227}GGGSGG^{232} (W151F, W278F)	Whole cell
CCT312His Δ12-16 L221W (W278F)	Pellet
CCT312His Δ12-16 L221W (W151F, W278F)	Pellet
CCT312His Δ12-16 Y225W (W278F)	Pellet
CCT312His Δ12-16 Y225W (W151F, W278F)	Pellet
CCT312His Δ12-16 L230W (W278F)	Pellet
CCT312His Δ12-16 L230W (W151F, W278F)	Pellet
CCT312His Δ12-16 V232W (W278F)	Pellet
CCT312His Δ12-16 V232W (W151F, W278F)	Pellet
CCT312His Δ12-16 F234W (W278F)	Pellet
CCT312His Δ12-16 F234W (W151F, W278F)	Pellet
CCT312His Δ12-16 L230A V232A F234A (W151F)	Whole cell
CCT312His Δ12-16 L230A V232A F234A (W278F)	Whole cell
CCT312His Δ12-16 L230A V232A F234A Y225W (W151F, W278F)	Whole cell
CCT312His Δ12-16 R219Q R223Q K228Q (W151F)	Whole cell
CCT312His Δ12-16 R219Q R223Q K228Q (W278F)	Whole cell
CCT312His Δ12-16 R219Q R223Q K228Q Y225W (W151F, W278F)	Whole cell
CCT312His Δ12-16 Y216A Y225A F234A Y225W (W151F, W278F)	Whole cell
CCT312His Δ12-16 ^{227}GGGSGG^{232} (purified by C. Tishyadhigama)	Whole cell
CCT312His Δ12-16 ^{227}GGGSGG^{232} (W151F) (purified by C. Tishyadhigama)	Whole cell
CCT312His Δ12-16 Δ227-232 (purified by C. Tishyadhigama)	Pellet
CCT312His Δ12-16 Δ227-232 (W151F) (purified by C. Tishyadhigama)	Whole cell
CCT312His Δ12-16 L221W Y225A (W278F)	Whole cell
CCT312His Δ12-16 L221F Y225A (W278F)	Whole cell
CCT312His Δ12-16 Y216W A217C (W151F, W278F)	Whole cell
HisCCT236 Δ12-16	Supernatant
HisCCT236 Δ12-16 Y225W (W151F)	Supernatant
HisCCT236 Δ12-16 Δ227-232	Supernatant
HisCCT236 Δ12-16 Y225W Δ227-232 (W151F)	Supernatant

Appendix E SDS-PAGE analysis of select CCT mutants

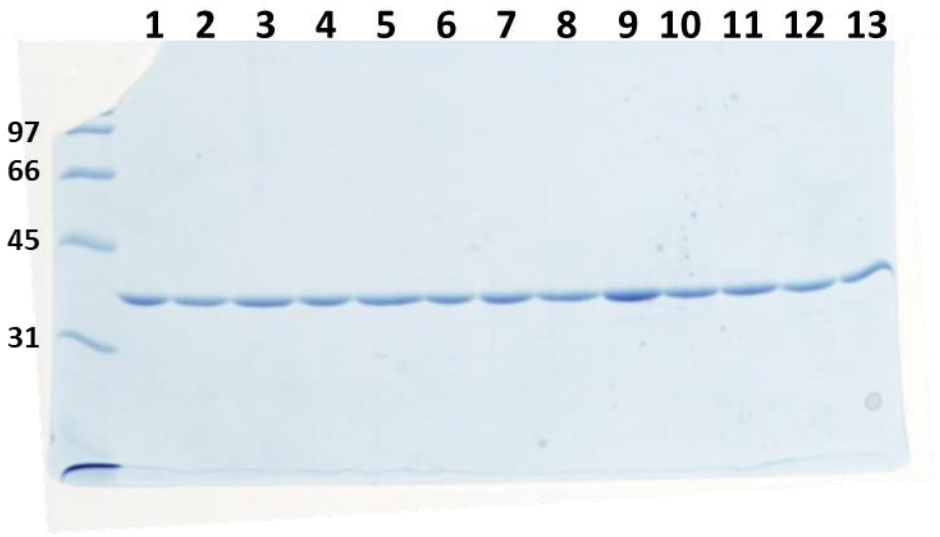

Lane	Construct	Code name
1	CCT312His Δ12-16 W278 (W151F)	W278
2	CCT312His Δ12-16 F55W (W151F, W278F)	W55
3	CCT312His Δ12-16 W151 (W278F)	W151
4	CCT312His Δ12-16 F121W (W151F, W278F)	W121
5	CCT312His Δ12-16 F124W (W151F, W278F)	W124
6	CCT312His Δ12-16 Y216W (W151F, W278F)	W216
7	CCT312His Δ12-16 L221W (W151F, W278F)	W221
8	CCT312His Δ12-16 Y225W (W151F, W278F)	W225
9	CCT312His Δ12-16 L230W (W151F, W278F)	W230
10	CCT312His Δ12-16 V232W (W151F, W278F)	W232
11	CCT312His Δ12-16 F234W (W151F, W278F)	W234
12	CCT312His Δ12-16 F124W ^{227}GGGSGG^{232} (W151F, W278F)	W124 GS linker
13	CCT312His Δ12-16 Y216W ^{227}GGGSGG^{232} (W151F, W278F)	W216 GS linker

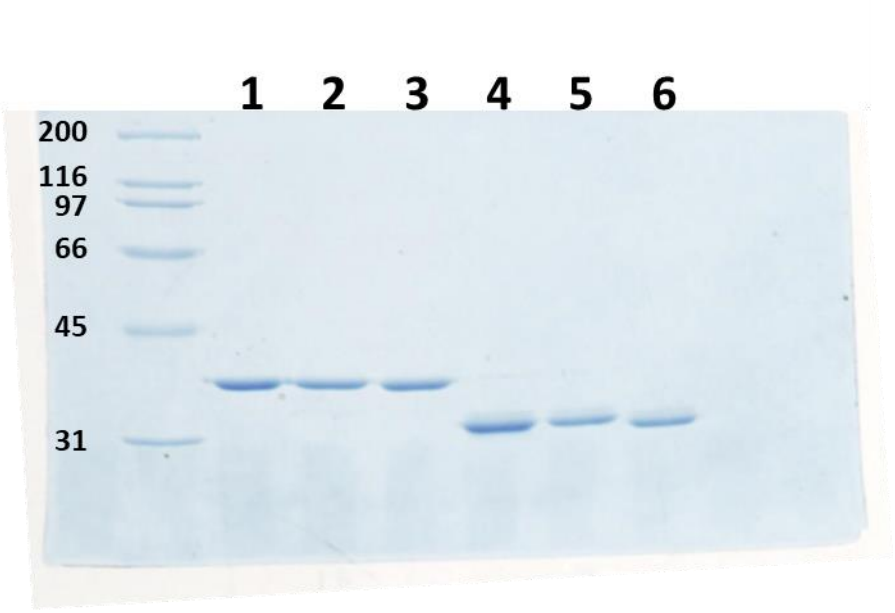

Lane	Construct	Code name
1	CCT312His Δ12-16 L230A V232A F234A Y225W (W151F, W278F)	Triple-A (W225)
2	CCT312His Δ12-16 R218Q, R223Q, K228Q Y225W (W151F, W278F)	Triple-Q (W225)
3	CCT312His Δ12-16 Y216A Y225A F234A Y225W (W151F, W278F)	Triple-Aro (W225)
4	HisCCT236 Δ12-16 W151	236 W151
5	HisCCT236 Δ12-16 Y225W (W151F)	236 W225
6	HisCCT236 Δ12-16 Y225W Δ227-232 (W151F)	236 W225 Δlinker

Appendix F P-values of BrPC quenching experiments

		P-values										
		W278	**W55**	**W151**	**W121**	**W124**	**W216**	**W221**	**W225**	**W230**	**W232**	**W234**
W278	diBrPC 6,7											
	diBrPC 9,10											
	diBrPC 11,12											
W55	diBrPC 6,7	0.0007										
	diBrPC 9,10	0.0144										
	diBrPC 11,12	0.0045										
W151	diBrPC 6,7	0.0002	0.4239									
	diBrPC 9,10	0.0041	0.5458									
	diBrPC 11,12	0.0008	0.8300									
W121	diBrPC 6,7	0.0054	0.2694	0.1260								
	diBrPC 9,10	0.0139	0.9544	0.5415								
	diBrPC 11,12	0.0070	0.3040	0.4893								
W124	diBrPC 6,7	0.0001	0.0057	0.0260	0.3425							
	diBrPC 9,10	0.0139	0.0423	0.1591	0.0390							
	diBrPC 11,12	0.0072	0.0040	0.0548	0.0032							
W216	diBrPC 6,7	0.0002	0.0145	0.0090	0.1118	0.2615						
	diBrPC 9,10	0.0057	0.4894	0.3453	0.4999	0.5029						
	diBrPC 11,12	0.0023	0.5771	0.6204	0.7008	0.0024						
W221	diBrPC 6,7	0.0001	0.0040	0.0056	0.0880	0.1399	0.9522					
	diBrPC 9,10	0.0066	0.0579	0.0487	0.0580	0.2197	0.1381					
	diBrPC 11,12	0.0009	0.0742	0.0806	0.1193	0.9938	0.1012					
W225	diBrPC 6,7	0.0378	0.0097	0.0037	0.0140	0.0241	0.0515	0.0516				
	diBrPC 9,10	0.0204	0.0617	0.0391	0.0616	0.1115	0.0757	0.3136				
	diBrPC 11,12	0.0017	0.0515	0.0493	0.0793	0.6788	0.0617	0.7559				
W230	diBrPC 6,7	0.4243	0.0619	0.0460	0.0750	0.1013	0.1313	0.1389	0.5473			
	diBrPC 9,10	0.0762	0.0021	0.0046	0.0009	0.0001	0.0003	0.0067	0.2084			
	diBrPC 11,12	0.0162	0.0292	0.0141	0.0393	0.0932	0.0253	0.0900	0.1323			
W232	diBrPC 6,7	0.0093	0.1625	0.0585	0.3702	0.8930	0.3910	0.3188	0.0282	0.0991		
	diBrPC 9,10	0.0117	0.2011	0.0975	0.1905	0.4311	0.2477	0.5436	0.1777	0.0254		
	diBrPC 11,12	0.0064	0.0401	0.1307	0.1137	0.0652	0.0354	0.4346	0.2507	0.0575		
W234	diBrPC 6,7	0.0292	0.0478	0.0052	0.0249	0.0332	0.0277	0.0295	0.8785	0.4854	0.0404	
	diBrPC 9,10	0.0298	0.0856	0.0141	0.0784	0.0646	0.0160	0.0874	0.7696	0.1673	0.0705	
	diBrPC 11,12	0.0149	0.0391	0.0328	0.0087	0.0149	0.0009	0.2816	0.4492	0.2345	0.0652	

For each BrPC position, statistical significance of the difference between unquenched/quenched values was determined for all pairs of Trp positions. P-values were generated using a two-sample unequal variance Student's t-Test with a two-tailed distribution.

Appendix G Emission spectra of Trps in the absence and presence of SUVs

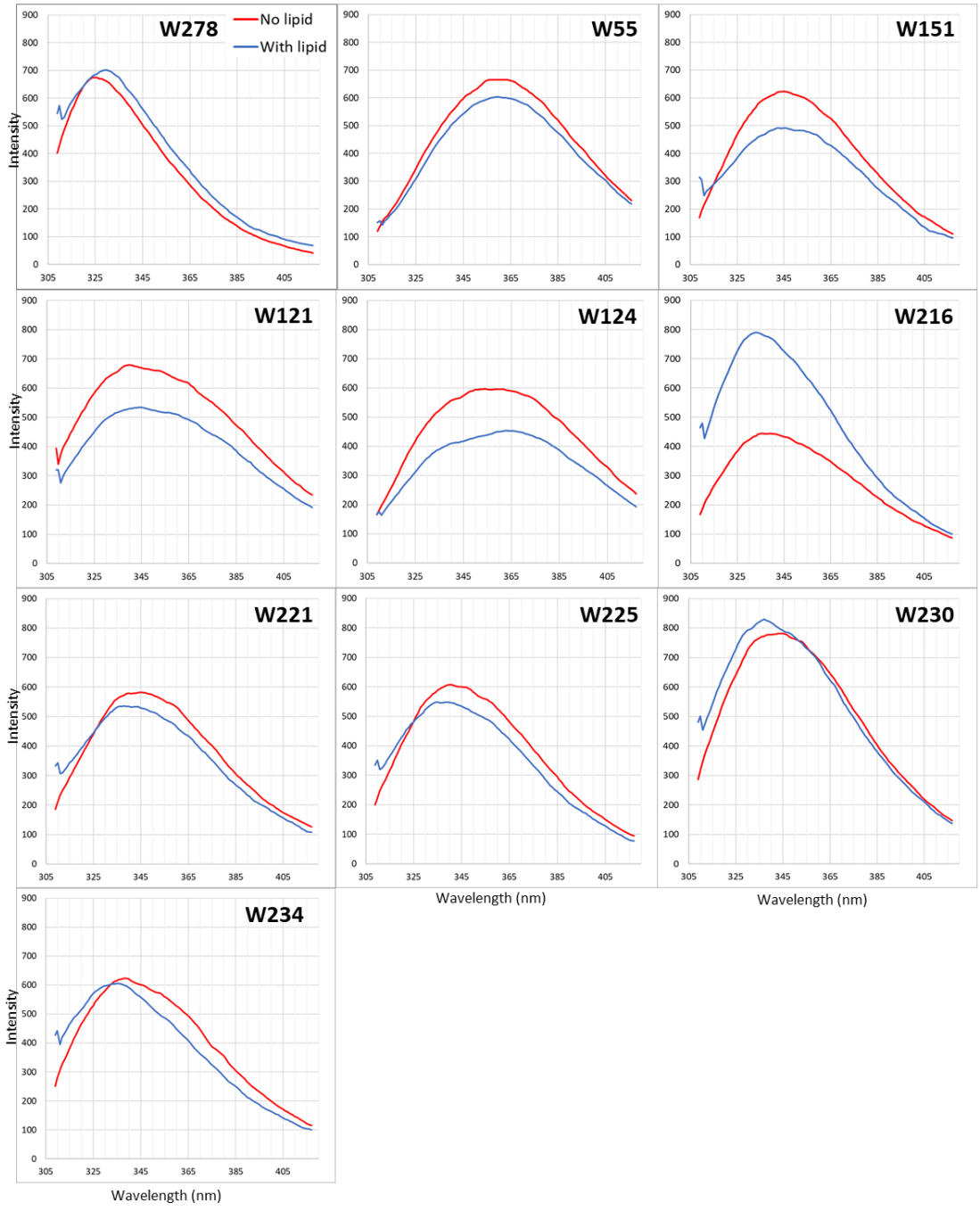

Sample spectra of single-Trp CCT312His Δ12-16 mutants (3 μM) in the absence and presence of 450 μM SUVs (50% eggPG, 50% POPC).

Appendix H FRET efficiency vs. Trp-dansyl distance plot

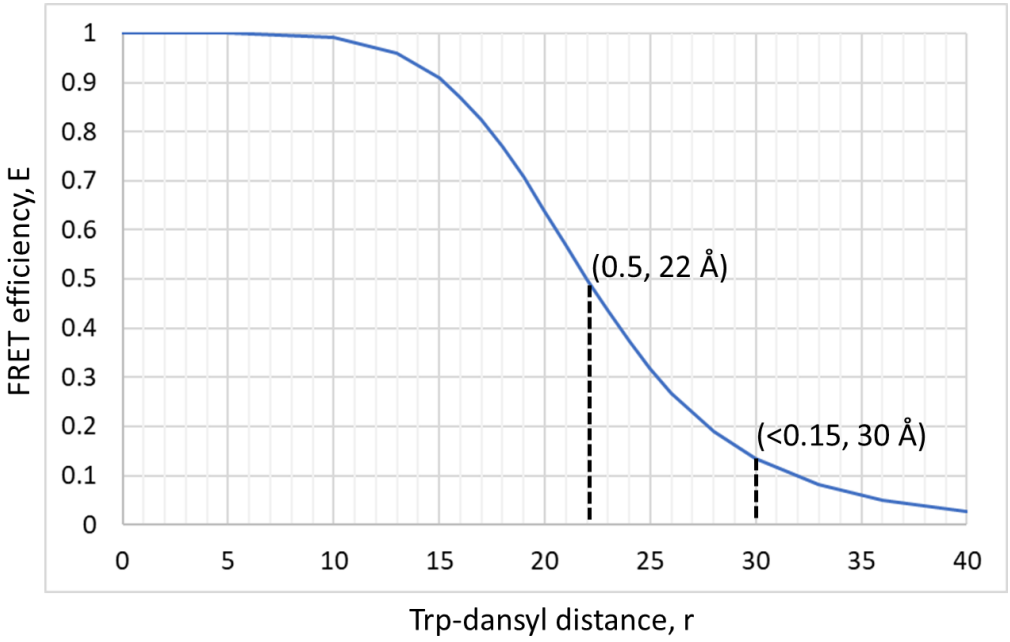

FRET efficiency (E) vs. donor-acceptor distance (r) based on the FRET relationship: $E = 1/(1-(r/R_0)^6)$, and an R_0 of 22 Å for the Trp-dansyl FRET pair. Above a Trp-dansyl distance of 30 Å, FRET efficiency is below 0.15.